COMPLEX OBJECT RECONSTRUCTION FROM FAR-FIELD INTENSITY AND ITS APPLICATION

A thesis submitted

in partial fulfilment for the degree of

Doctor of Philosophy

by

SURYA KUMAR GAUTAM

Department of Physics
INDIAN INSTITUTE OF SPACE SCIENCE AND TECHNOLOGY
Thiruvananthapuram - 695547
November, 2022

COMPLEX OBJECT RECONSTRUCTION FROM FAR-FIELD INTENSITY AND ITS APPLICATION

A thesis submitted

in partial fulfilment for the degree of

Doctor of Philosophy

by

SURYA KUMAR GAUTAM

Department of Physics
INDIAN INSTITUTE OF SPACE SCIENCE AND TECHNOLOGY
Thiruvananthapuram - 695547
November, 2022

Dedicated to my parents.....

CERTIFICATE

This is to certify that the thesis entitled **Complex object reconstruction from far-field intensity and its application** submitted by **Surya Kumar Gautam** to the Indian Institute of Space Science and Technology, Thiruvananthapuram, in partial fulfilment for the award of the degree of **Doctor of Philosophy** is a *bonafide* record of research work carried out by him under my supervision. The contents of this thesis, in full or in parts, have not been submitted to any other Institution or University for the award of any degree or diploma.

Dr. Dinesh N. Naik
Supervisor
Associate Professor
Department of Physics

Dr. Sudheesh Chethil
Professor & Head
Department of Physics

Thiruvananthapuram
November
2022

DECLARATION

I declare that this thesis entitled **Complex object reconstruction from far-field intensity and its application** submitted in partial fulfilment of the degree of **Doctor of Philosophy** is a record of original work carried out by me under the supervision of **Assoc. Prof. Dinesh N. Naik**, and has not formed the basis for the award of any other degree or diploma, in this or any other Institution or University. In keeping with the ethical practice in reporting scientific information, due acknowledgments have been made wherever the findings of others have been cited.

SURYA KUMAR GAUTAM

(SC16D048)

Thiruvananthapuram–695547

[24th November 2022]

Acknowledgments

I would like to give acknowledgment to IIST and Prof. C. S. Narayanamurthy for developing optical laboratory, which has one of the best facilities across India inside a wonderful green campus. I express my deepest gratitude towards my supervisors Prof. Rakesh Kumar Singh and Prof. Dinesh N Naik, for their helpful suggestions and guidance. I am sincerely thankful to Prof. Rakesh Kumar Singh for giving me this wonderful opportunity and introducing me to the fundamental problem associated with computational imaging. In addition, I am sincerely thankful to Prof. Dinesh N Naik for all the suggestions and help he offered me while performing the simulations as well as the experiments. Besides, heartfelt appreciation to Prof. Dinesh N Naik, who not only help me academically but also in my toughest time. Moreover, I also appreciate their immeasurable time that they have spent during the productive discussions with me. I am also grateful to the technical staff Mrs. Surasreelekshmi, Mrs. Leksmi Devan and Ms. Arya S. for providing the optical components, software and moral help and support whenever I need. To move from the north part of India to the south is not easy. Initially to adjust in an unknown location which is far from home with a different language, food, and culture is the toughest thing I have ever experienced. Nonetheless, with friends, this place seems no different than my home. I am lucky to have such amazing friends, Pramod, Preetam, Praveen, Darshika, Athira, Lekshmi, Shalabh, and Narendra. They have made this difficult journey peaceful, adventurous, and joyful for me. I am indebted to my mother Ms. Omwati and my late father Mr. Prathvi Singh, for supporting me in any way possible and never letting me get involved in their suffering and hardship, which they have endured alone. I am grateful for my siblings, they inspire me and constantly push me beyond my limits and help me throughout my life. Special credit goes to my younger brother Mr. Ashwani for structuring, improving, and helping me throughout the writing process and for providing me criticizing comments for my personal growth. Last but not the least, I would like to express my regard and gratitude towards my wife for all the courage, love and support.

Surya Kumar Gautam

Abstract

Non-destructive testing techniques are beneficial in many applications where one needs to study delicate objects or the objects that are located far away from the physical reach. Utilizing the optical methods, one can access the information of such objects without touching them physically or non-destructively. Existing non-destructive optical methods such as 1) holography and 2) phase retrieval iterative algorithms have some limitations.

To overcome those limitations, this thesis presents several novel optical non-destructive methods for reconstructing the complex object from an intensity recorded at the far-field using a conventional camera. Most of the methods presented in this thesis require capturing of a single intensity; therefore, opening up immense opportunities in real-time complex object imaging applications which are suitable for static as well as dynamic objects. Existing technique such as holography requires a separate beam which is derived from the illumination beam. This separate beam is considered as the reference field for encoding the phase of the illumination beam modified by the object in intensity redistribution resulting from their interference. The presence of this separate reference field being independent from the object field makes the system prone to external vibrations leading to phase error while reconstructing the phase. On the contrary, the methods proposed in the thesis employ edge point of the object itself as a source of reference field; therefore, the proposed methods do not require a separate reference beam. In the first method, we utilized the fact that object autocorrelation that can be obtained from the recorded far-field intensity at the Fourier plane by performing a two-dimensional Fourier transformation operation numerically contains the object information provided the object has a direction of asymmetry. Therefore, we crop some part of the object autocorrelation, which contains the object information, and utilize it as an initial guess to solve the problems involved in the phase retrieval iterative algorithm, resulting in unique, deterministic, twin-image free reconstruction. We follow up this investigation using a second method where the beam used for the illumination is structured utilizing an additional beam. By incorporating this additional beam, we can create the asymmetry in the beam itself. Due to this modification in the

illumination beam, irrespective of whether the objects have the direction of asymmetry or not, the proposed method provides desired results along with fast convergence. In holography, the reference field is generally independent and kept separately from the object. Considering the fact that one cannot isolate the optical system completely from the external vibration, the reference field can vibrate slightly with respect to the object field due to the external vibration, this can cause repeatability problem in the reconstruction from the holography. Moreover, for some objects which are located far from physical reach, putting the reference source nearby is difficult. Whereas in the proposed method where additional beam is used to illuminate the object edge point, even if object field oscillates due to the vibration, reference field which is scattered from the object edge point also oscillates in a similar manner. In order to reduce vibrational effects further, additional beam used to illuminate the edge point of the object is derived by utilizing simple, common path and robust optical setup. As a result, the relative motion between the reference and object's field is reduced significantly and thus, our approach works better in practical situations where the effect of external vibration cannot be avoided and is also suitable for analyzing the objects located far from reach. Utilizing the edge point of the object as a reference field makes the proposed method suitable even in vibrational environment, as compared to those based on the holography. Further, another method is proposed for reconstructing the complex object information from the hologram recorded optically. This method is beneficial in volumetric holographic data storage and reconstruction application. Furthermore, a technique is developed where one needs to capture the object photograph along with the far-field intensity for the reconstruction in a single shot. In addition, a non-iterative approach is also proposed; however, this approach needs two shots of the recording. There are several applications where one can utilize the proposed methods to study the object properties non-destructively. One of the applications in measuring the real-time deformation of an object under the mechanical loading is also presented in the final part of the thesis. Throughout the thesis, in each chapter, a detailed mathematical derivation is first established for proof of concept. Secondly, simulations are performed to support the theory. In the initial part of the thesis for reconstructing the complex object, modified iterative

techniques are designed and discussed, while non-iterative techniques are developed and presented in the final part of the thesis. Thirdly, novel, simple experimental setups are suggested and examined for recording the far-field intensity of a complex object, and image processing codes are also created for retrieving the complex object numerically in the MATLAB programming language.

ABBREVIATIONS

CCD	Charge Coupled Device
SLM	Spatial Light Modulator
He-Ne	Helium Neon
L	Lens
M	Mirror
SF	Spatial Filter
BS	Beam Splitter
PBS	Polarizing Beam Splitter
HWP	Half Wave Plate
QWP	Quarter Wave Plate
Pol	Polarizer
MO	Microscope Objective Lens
F.T.	Fourier Transformation
I.F.T	Inverse Fourier Transformation
PRA	Phase Retrieval Iterative Algorithm
EPR	Edge Point Referencing

NOTATIONS

$\emptyset$	Phase
λ	Wavelength
β	Feedback Coefficient
ε or E	Error
A_c or $\breve{g}$	Autocorrelation
f_x , f_y	Spatial Frequencies
k_x , k_y	Spatial coordinates

Table of Contents

Chapter 1 1
Introduction 1
1.1 Optical techniques 1
1.2 Mathematical model 1
1.2.1 Light source 2
1.2.2 Optical sensor 3
1.2.3 Propagation of a light field 3
1.2.4 Image processing 5
1.2.5 Existing techniques 5
1.2.6 Optical setup 8
1.3 Motivation 9
1.4 Outline of the thesis 9
1.5 Holography vs Edge Point Referencing 11
1.6 Common path setups 13
1.7 Conventions 15
Chapter 2 17
Single-shot and twin-image free unique phase retrieval using an aspect of autocorrelation that considers the object asymmetry 17
2.1 Introduction 17
2.2 Principle 19
2.3 Simulation, results and discussion 23
2.4 Random verses improved initial guess 28
2.5 Effect of noise 30
2.6 Experimental results 34
2.7 How to improve experimental results 37
2.8 Conclusion 41
Chapter 3 42
Phase retrieval algorithms using edge point referencing 42
3.1 Foundation 43
3.2 Theory 44
3.3 Simulations 47
3.3.1 Simulation result without the edge point referencing 47

3.3.2 Simulation result with the edge point referencing 48
3.4 Effect of noise 51
3.5 Experimental setup 53
3.5.1 Experimental results 54
3.6 Simulation result for deformation measurement 58
3.7 Summary 59
Chapter 4 61
Phase retrieval algorithm in volumetic holographic data storage and reconstruction 61
4.1 Basic Idea 62
4.2 Formulation 63
4.3 The procedure of recording and reconstruction 66
4.4 Simulation result 68
4.5 Simulation results when noise is present 72
4.6 Conclusion 74
Chapter 5 75
Photograph assisted Phase retrieval algorithm 75
5.1 The flow diagram of the proposed scheme 77
5.2 Optical setup 78
5.3 Numerical result 79
5.4 Comparison with random Guess 81
5.5 Effect of noise 83
5.6 Conclusion 84
Chapter 6 85
Reconstruction of complex-object using edge point referencing 85
6.1 Introduction 85
6.2 Principle 90
6.3 Simulation Results 94
6.4 Experimental Procedure 96
6.5 Results 97
6.6 Discussion 101
6.7 Conclusion 101
Chapter 7 103
Discrete and quantitative reconstruction of the out of plane non-linear deformation using local autocorrelations 103
7.1 Concept 103

7.2 Background 103
7.3 Derivation 107
7.4 Simulation results without and with the mask 116
7.5 Experiment and results 126
7.6 Conclusion 129
Conclusions and Future Scope 130
- Conclusions 130
- Future scope 132
Appendix A 133
A.1 Introduction 133
A.2 Principle 133
A.3 Simulation, results and discussion 135
Appendix B 137
B.1 Introduction 137
B.2 Random verses improved initial guess 137
Appendix C 141
C.1 Effect of the different shapes of the objects on the autocorrelations 141
Appendix D 146
HIO and HIO+GS algorithms 146
References 149
List of Publication 157

List of Figures

Figure 1.1: Scattering of a light field from the object 3

Figure 1.2: Propagation and recording of a complex field scatted from the object. 4

Figure 1.3: (a) Optical setup for recording off-axis hologram at the far-field, (b) distribution in the reconstruction plane. 6

Figure 1.4 (a): Optical setup for in-line holography, (b) distribution in the reconstruction plane. 7

Figure 1.5: Setup for (a) Holography, (b) Edge point referencing. 12

Figure 1.6: Common path setups for generating edge point referencing (a) using a ND filter, (b) using a spatial light modulator, and (c) using optical components, paths taken by the light reflected and transmitted from the PBS in figure (c) are shown in (d) and (e), respectivly. 15

Figure 2.1: (a) complex object bounded with radius ro where $P1(ro, \theta\text{-}180)$ and $P2(ro, \theta)$ show the two small circular portions of the desired object, located ro distance away from the origin and oriented at $\theta\text{-}180$ and θ degree respectively with respect to the x axis , (b) object autocorrelation, dotted and solid circles show the locations of 2^{nd} and 3^{rd} terms mentioned in the equation (2.5). 20

Figure 2.2: Images of (a) Letter 'A' (mirror symmetry about the y axis and asymmetry about the x axis) and (b) Letter 'P', representing the object amplitude and phase used in the PRA respectively, (c) intensity recorded at the Fourier plane, (d) object autocorrelation, dotted circle shows the $S(ro, \theta)$ 24

Figure 2.3: (a) Solid curve shows the error in the output after 1000 iterations with respect to the direction θ; the direction from which the filtered section is cropped using object support $S(ro, \theta)$; dotted line shows the object asymmetry factor measured along these orientations. (b) Object support $S(0,0)$ at origin, (c) object support $S(ro, \theta)$ with its center shifted at ro and oriented at θ, white color shows the location of the points which are inside the region $S(ro, \theta)$, i.e. $r \in S(ro, \theta)$ and black color shows the location of the points that lie outside the $S(ro, \theta)$, i.e. $r \notin S(ro, \theta)$. (d) and (e) correspond to the retrieved amplitude and phase

information, for $\theta = 0^0$, while (f) and (g) indicate the retrieved amplitude and phase information, for $\theta = 136.50^0$. Here amplitude and phase values are normalized between [0,1] and [-π, π], respectively. 26
Figure 2.4: Effect on reconstruction of PRA-HIO algorithm when initialized with different random guesses: (a) correct amplitude and (b) correct phase reconstruction, (c) twin amplitude and (d) twin phase reconstruction, (e) inverted and conjugate amplitude and (f) inverted and conjugate phase reconstruction, (g) Effect on errors when executing the algorithm multiple time. 30
Figure 2.5: Simulation results when noises are added in the measured data, reconstruction of amplitude and phase (a) and (b) respectively when noise level is 0.05%, (c) and (d) when it is 0.5 %, (e) and (f) noise level is 5% and (g) and (h) 50% noise is added with respect to the average intensity value. 32
Figure 2.6: Patterns of (a) peppers and (b) boats, representing the complex object amplitude and phase used in the PRA respectively, (c) intensity recorded at the Fourier plane, (d) object autocorrelation, where the dotted circle shows the location of $S(ro, \theta)$. Since object autocorrelation is a complex function only its modulus is shown here. (e) and (f) are the retrieved amplitude and phase information, for $\theta = 74.03^0$. 33
Figure 2.7: (a) Experimental setup for recording object diffraction pattern at the Fourier plane (b) intensity at the Fourier plane, (c) modulus of the object autocorrelation, solid and dotted circles show the filtering locations for two initial guesses for PRA, located at $\theta = 0^0$ and $\theta = 90^0$ respectively, (d) and (e) are the moduli of reconstructed object corresponding to $\theta = 0^0$ and $\theta = 90^0$ respectively. 35
Figure 2.8: Experimental reconstruction results for different objects (a) a portion of USAF chart containing 3 lines followed by a diffuser screen, (b) a square shaped black paper followed by a diffuser screen, (c) a shape of letter 'T' followed by a diffuser screen, (d) and a portion of metal rular containing letter '5'. 37
Figure 2.9: (a) Experimental setup for recording object diffraction pattern at the Fourier plane (b) intensity at the Fourier plane, (c) modulus of the object autocorrelation, dotted circle shows the filtering locations, located at θ , (d) and (e) are the error plots plotted after 1000 iterations by changing the size of support and direction of cropping

respectively. (f) and (g) moduli of reconstructed object after 1000 and 10000 iteratons respectively at $\theta = -79^{0}$ and $ro = 273$ pixels. 41
Figure 3.1: Setup for recording object information using EPR scheme. 45
Figure 3.2: object autocorrelation: 1st and 2nd terms show the DC terms, 3rd and 4th terms correspond to the object and its twin as mentioned in equation (3.5). ...46
Figure 3.3: Object reconstruction using PRA without the EPR 47
Figure 3.4: Object reconstruction using PRA-EPR, in (a) and (b) arrow-head shows the location of a small area near the edge. 49
Figure 3.5: Convergence rates of the PRA with respect to the number of iterations for two cases at $c = 45$ and at $c = 50$. 51
Figure 3.6: Simulation results when noises are added in the measured data, reconstruction of amplitude and phase (a) and (b) respectively when noise level is 0.05%, (c) and (d) when it is 0.5 %, (e) and (f) noise is 5% and (g) and (h) 50% noise is added with respect to the average intensity value. 53
Figure 3.7: Experimental setup, HWP: half wave plate, PBS: Polarizing beam splitter, BS: Beam splitter, M1 and M2: mirrors, L1-L3: Lenses, Pol: polarizer and CCD: charge coupled device or a camera. Intensity of the beams can be controlled via rotating HWP and for generating an interference pattern a Pol is placed and oriented at 45 degree. 54
Figure 3.8: Experimental result without the edge point referencing 55
Figure 3.9: Experimental result with edge point referencing 55
Figure 3.10: Experimental result with intense edge point referencing 56
Figure 3.11: Deformation measurement using PRA-EPR. The arrow head shows the location of a small area near the object's edge. 58
Figure 4.1: (a) Object-inverted conjugate pair, (b) Autocorrelation and 1st and 2nd terms show the DC part and 3rd and 4th terms represent the object convolution with itself or the object copies, and inverted-conjugate convolution with itself or the inverted-conjugate copies, solid and dotted circle show the object and inverted conjugate support, respectively, (c) Formation of initial guess by filtering portions from the autocorrelation using solid and dotted circles and placing them at a distance d from each other. 65

Figure 4.2: (a) Complex object data recording optically at the Fourier plane, (b) complex object data recording optically using lensless Fourier geometry, (c) optical to digital data recording and (d) complex object reconstruction digitally using PRA. 68
Figure 4.3: Optical recording and optical reconstruction from the Fourier hologram 69
Figure 4.4: Digital recording and digital reconstruction from the Fourier hologram. 72
Figure 4.5: Simulation results when noises are added in the measured data, reconstruction of amplitude and phase (a) and (b) respectively when noise level is 0.05%, (c) and (d) when it is 0.5 %, (e) and (f) noise is 5% and (g) and (h) 50% noise is added with respect to the average intensity value. 73
Figure 5.1 : Flow diagram of a photograph assisted PRA. 77
Figure 5.2: Optical setup, in the inset near the laser: amplitude and phase of the complex object is shown, and in the inset near the CCD: amplitude and far-field patterns recorded simultaneously onto the camera screen in a single-shot are shown. 78
Figure 5.3: Numerical result. 80
Figure 5.4: (a) Errors plotted for the reconstruction using random and improved guesses, (b) reconstructions of phase part of the object using random guesses in 10 different trails, each time a new random guess is used as an initial guess. 82
Figure 5.5: Simulation results when noises are added in the measured data, reconstruction of phases (a), (b), (c) and (d), when noise levels are 0.05%, 0.5%, 5% and 50% , respectively are added with respect to the average intensity value. 83
Figure 6.1: (a) Conceptual diagram for slightly off-axis lensless geometry for transparent object, (b) and (c) for reflecting object, (d) conceptual diagram with edge point referencing. o(r), R(r)and i(r) denote the object, reference and illumination field, BS and CCD denote the beam splitter and charge couple device camera. 88
Figure 6.2: Two dimensional complex valued object field. 91

Figure 6.3: (a) object autocorrelation : 1st term in equation (6.7) shows the DC term, 2nd term shows the edge point intensity and 3rd and 4th terms correspond to the object and its twin weighted by complex amplitude (b) Extracted object o(r) and its twin o*(-r) (2nd and 3rd terms in equation (6.10), respectively). 93
Figure 6.4: A simulation study, (a) and (b) modulus and phase part of 2D object, (c) reconstructed distribution and (d) effect on the reconstruction with the size of edge point referencing, colorbar in (a) and (c) show the amplitude and in (b) it shows the phase distribution. 95
Figure 6.5: (a) Shows the compact robust common path illumination beam setup (IBS): solid line shows the collimated beam and dotted lines show the converging beam. (b) The lensless imaging setup to image the complex object in reflection geometry. HWP: half wave plate, MO and SF: microscope objective lens and spatial filter, L, L1 and L2 are the biconvex lenses, PBS: polarizing beam splitter, M1 and M2 show the mirrors. 96
Figure 6.6: Recorded intensities with HWP oriented at: (a) 0^0 (b) 4^0, (c) Subtracted intensity pattern, (d-f) moduli of autocorrelation corresponding to (a-c), respectively. The colorbar beside each diagram indicates the amplitude values distribution for the respective image. 98
Figure 6.7: Real-time deformation measurement: (a) deformable object, (b) and (c) show the intensity patterns recorded in undeformed and deformed conditions and compared phase part of autocorrelation is shown in (d), colorbar for (b) and (c) show the intensity values distribution, and in (d) it shows the phase value distribution. 99
Figure 6.8: (a) Two metal rulers, separated by 8.5 *cm*, are used as a 3D object and solid and dotted lines show the collimated and converging beam, (b) and (c) recorded intensties with HWP oriented at 0^0 and 4^0, (d) subtracted intensity pattern, (e-g) moduli of autocorrelations corresponding to (b-d) respectively, and (h) modulus of propagated field, (i) and (j) enlarged portions of the area enclosed with the dotted lines shown in (g) and (h), respectively. 100
Figure 7.1: (a) Setup for measuring deformation, (b) ray diagram of the setup, (c) shows how a mask having 2×2 cells divides the object into 2×2 sub-regions and results in creating 2×2 sub-images, this figure also shows that scattered field

from a sub-region of the object that is behind a cell of the mask (M11) propagates and falls on a small part the camera i.e., sub-image (I11), (d) enlarged portion of a sub-region of the object $g_{pq}(x, y)$ which is behind M_{pq} and respective sub-image I_{pq}, where subscript p and q represent the corresponding location, located at p^{th} row and q^{th} column. 108
Figure 7.2: Procedure for measuring nonlinear deformation.....110
Figure 7.3: (a) and (b) sub-images i.e., I_{pq} and I'_{pq}, (c) linear deformation introduced in the sub-region of the object behind a particular cell, (d) unwrap and normalized version of the (c) shows the linear deformation or tilt, (e) and (f) show the respective line plots plotted with respect to the solid and dotted lines shown in (c) and (d) respectively, (g) and (h) amplitudes of the local autocorrelations obtained computationally from the sub-images (a) and (b), (i) and (j) show the corresponding phases of the local autocorrelations, (k) and (l) amplitude M_{s_pq} and phase $\emptyset_{s\_pq}$ information of the function S_{pq}, (m) and (n) wrapped, and unwrapped and normalized line plots; with respect to the line indicated in (l). 115
Figure 7.4: (a) and (b) amplitude and phase of the object used for the simulation. The value of amplitude is chosen unity throughout the entire region, and the value of the phase is varying spatially between $-\pi$ to π randomly. 117
Figure 7.5: Deformation introduced in the phase part of the object. 117
Figure 7.6: (a) and (b) line plots are plotted with respect to the solid and dotted lines shown in figures 7.5 (a) and (b) respectively. 118
Figure 7.7: Simulation without the mask.....121
Figure 7.8: Simulation with the mask.....121
Figure 7.9: Simulation result without the mask.....123
Figure 7.10: Simulation result with the mask.....123
Figure 7.11: Effect with respect to the size of the sub-image on signal to noise ratio, resolution, and processing time (a), (b) and (c) respectively. 125
Figure 7.12: Deformable object.....126
Figure 7.13: Experimental results with the mask 128
Figure A.1: Patterns of (a) Letter 'M' and (b) uniform distribution, show the object amplitude and phase used in the PRA respectively, collections of points

near the peripheries of the desired object are denoted by red color/dotted circled c1 , c2 , c3 and c4 (c) intensity recorded at the Fourier plane, (d) object autocorrelation, dotted and solid circles show the cropping locations using object support from x and y directions respectively. Reconstructions using a portion cropped from the autocorrelation displaced by a dotted circle in (d) are shown in (e) and (f) as amplitude and phase, respectively, (g) and (h) show the retrieved amplitude and phase information, for the portion filtered from the autocorrelation using a solid circle as shown in (d). Here images of all the amplitudes and phases are normalized between [0,1] and [-π, π]. 135
Figure B.1: Patterns of (a) Letter 'M' and (b) uniform distribution, show the object amplitude and phase used in the PRA respectively, (c) intensity recorded at the Fourier plane, (d) object autocorrelation, a solid circle shows a filtering location using a object support. Reconstructions using the filtered portion from the autocorrelation displaced by the solid circle in (d) are shown in (e) and (f) as amplitude and phase, respectively, (g) and (h), (i) and (j), (k) and (l) show the retrieved amplitudes and phases information, when the random guesses are used as in initial guesses while executing the algorithm multiple times, (m) reconstruction errors in both the cases: using random and improved initial guesses displayed by square and circle symbol, respectively with respect to the execution of the algorithm multiple times, (n) effect of the size of the object support on the errors of the reconstructions. Here all the amplitudes and phases are normalized between [0,1] and [-π, π**]**, respectively.....139
Figure C.1.1: (a) Special object contains an object and a reference point, (b) object autocorrelation for the 'special object' shown in (a). 141
Figure C.1.2: (a) 'Special object' contains an object and two reference points, (b) respective autocorrelation. 142
Figure C.1.3: (a) 'Special object' contains object and three reference points, (b) corresponding object's autocorrelation. 142
Figure C.1.4: (a) 'Special object' contains object and three reference points, (b) corresponding object autocorrelation of the 'special object'. 143
Figure C.1.5: (a) 'Special object' contains two copies of the object, (b) respective autocorrelation 144

Figure C.1.6: (a) ‘Special object’ contains object and inverted-conjugate pair, (b) respective object autocorrelation. 144
Figure D.1: Flow diagram of hybrid input-output (HIO) phase retrieval algorithm. 147
Figure D.2: Flow diagram of hybrid input-output (HIO) followed by the Gerchberg–Saxton (GS) phase retrieval algorithm.....148

Chapter 1

Introduction

1.1 Optical techniques

In various fields of science and technology, situations arise where one desires to measure some information about the object. To fulfill this aim, one gathers a collection of measurements. From this collection, one makes an effort to evaluate the object information. Moreover, measurements can be made either using destructive testing where one needs to contact the object surface or using non-destructive testing (contactless). In the contact techniques for delicate objects, the possibility of damaging the objects is high. For an object located far from reach, it is always beneficial to adopt non-contact and non-destructive techniques for the measurements. In such non-destructive techniques, optical methods are well suited where one can illuminate the aforementioned objects with a light source and the scattered light from such objects can be captured using an optical sensor.

Non-destructive testing (NDT) using optical sensors has immense potential in various applications such as image processing, wavefront sensing, biomedical imaging, deformation measurement of an object under loading conditions, x-ray crystallography, gas sensing, to study the hazards materials, optical element testing, holographic data storage and reconstruction etc. In order to understand, design, and develop an optical method for NDT purposes, a mathematical model should be established first.

1.2 Mathematical model

To build a mathematical model, one needs to consider few parameters associated with the technique as given below

- Light source
- Optical sensor

- Propagation of a light field
- Image processing
- Existing techniques
    - Off-axis holography
    - In-line holography
    - Phase retrieval iterative algorithm
- Optical setup

1.2.1 Light source

There are mainly two types of light sources [1] utilized for illumination purpose: 1) incoherent and 2) coherent sources. In the incoherent light source, phase part of a light field is not stable, while in the coherent light source, the phase part is steady within the coherent length. Based on the applications, one can select the light source. Throughout the thesis, a coherent laser light is selected for its large coherence length.

Since the optical field has amplitude and phase, illumination field IF of a light source can be represented mathematically as a two dimensional complex function, as given below

$$IF(x, y, t) = a(x, y)e^{i(k.r-\omega t)}. \quad (1.1)$$

where (x, y) represents the two dimensional coordinates system at the field plane, t and r indicate the time and propagation vector of the respective field, $k = \frac{2\pi}{\lambda}$ and ω signify wavenumber and frequency of the light wave. In equation (1.1), the amplitude and phase parts of the field are indicated with $a(x, y)$ and exponential factor i.e. $(k.r - \omega t)$, respectively. Since we are only interested in measuring the field at a particular instance, dependency of the function $IF(x, y, t)$ on time can be omitted, which leads to

$$IF(x, y) = a(x, y)e^{i(k.r)}. \quad (1.2)$$

In this thesis, all the optical fields are represented in a similar fashion as mentioned in the equation (1.2).

1.2.2 Optical sensor

When the object is illuminated with the coherent laser light either in transmission or reflection mode, it scatters the light as shown in figures 1.1 (a) and (b).

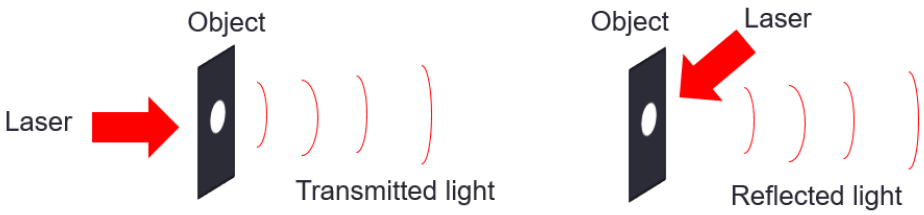

(a) Transmission mode (b) Reflection mode

Figure 1.1: Scattering of a light field from the object

To sense the scattered light, a sensor / detector is used. Detector based on the application can be further divided into two i.e., chemical and electrical based. A chemical based light detector i.e., photographic plate [2] or photo emulsion plate, detects the light by changing its material property. On the other hand, an electrical based detector such as complementary metal-oxide semiconductor (CMOS) or charged couple device (CCD) [3], converts the light into an electric signal that can be processed later in the computer. However, both kinds of detectors are sensitive to intensity of the light field. By recording only the intensity information, one can only find the amplitude information of the light field, whereas the phase part of the complex light field gets lost during the recording. In some applications, as mentioned before, the amplitude as well as phase parts contain useful information about the object properties and one has to retrieve both the parts of the field for the NDT purposes.

1.2.3 Propagation of a light field

When an object is illuminated with a light field $IF(x, y)$, it absorbs some part of the light and scatters the remaining part of the field, the scattered field $g(x, y)$ depends on the spatially varying object field and the illumination field that can be represented mathematically as follow

$$g(x, y) = \alpha . o(x, y) . IF(x, y). \tag{1.3}$$

Where α denotes the scattering coefficient and $o(x, y)$ represents the complex object. For simplicity throughout this thesis the value of the scattering coefficient is assumed to be one.

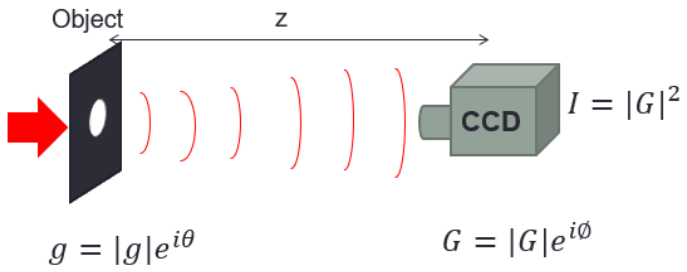

Figure 1.2: Propagation and recording of a complex field scatted from the object.

In figure 1.2, the laser light used to illuminate the object is denoted with an arrow. The scattered and propagated field from the object is displayed by the curved lines. For the sake of simplicity, dependency of the fields on the coordinates can be ignored for now, resulting in

$$g = \alpha . o . IF \tag{1.4}$$

Since illumination field is a complex function containing amplitude and phase, scattering field can also be written in terms of a complex function as follow,

$$g = |g|e^{i\theta}. \tag{1.5}$$

Where amplitude and phase of the scattered field are denoted with the $|g|$ and θ , respectively. When this field propagates in space, it changes with respect to the propagation distance z . The field propagation in free space can be generally described by the Huygens-Fresnel principle [4]. According to this, field G after the propagation can be written in terms of the field g i.e.,

$$G(\check{x}, \check{y}) = |G|e^{i\phi} = \frac{1}{j\lambda} \iint \frac{g(x, y) . \exp\,(jk . r)}{r} \cos\varphi \, dxdy. \tag{1.6}$$

Where λ is the wavelength of the light field, r is a vector pointing from (x, y) to $(\check{x}, \check{y})$ and φ is angle between r and outward normal. To capture this field either a CCD camera or photographic plate should be placed.

1.2.4 Image processing

Assuming, a CCD camera is placed at a distance z away from the object as shown in figure 1.2, since the camera is sensitive to the intensity of the light field, the two dimensional pattern captured using the CCD camera can be described as

$$I = |G|^2. \tag{1.7}$$

From equation (1.7), amplitude information can be calculated by performing a two dimensional square root operation on the intensity pattern numerically. Note CCD camera does not record the phase part of the propagated field directly. Therefore, retrieving the phase information of the field is not an easy task, it requires extensive image processing e.g., Fourier fringe analysis [5], numerical Fourier and inverse Fourier transformation operations [6], digital holography [7] and phase retrieval iterative algorithm [8] etc.

1.2.5 Existing techniques

Since the camera records only the intensity, to record the phase part of the field, in some techniques, an interference pattern is formed by introducing a reference field along with the object field, while in others a numerical iterative method is incorporated. In the first technique, an interference pattern is formed by overlapping above mentioned two fields with one another, which can easily be recorded with the camera. This technique is well known as Holography, and the interference pattern recorded is known as a hologram, that can be written as

$$I = |G + R|^2. \tag{1.8}$$

Expanding the brackets, equation (1.8) simplifies to

$$I = |G|^2 + |R|^2 + R^*G + R.G^*. \tag{1.9}$$

The interference pattern or the hologram contains four terms; on the right hand side 1st and 2nd terms of the above equation represent the intensity of the object and the reference fields, respectively. Cross terms are mentioned in the equation (1.9) by 3rd and 4th terms. The cross terms of the equation (1.9), possess the object information, however, they are merged with the remaining terms. In order to separate those terms from one another, holography is further divided into two techniques: 1) off-axis holography [9] and 2) in-line holography [10] .

1.2.5.1 Off-axis holography

In the off-axis holography, as the name suggests, reference and object fields propagate slightly off-axis from one another as shown in figure 1.3 (a), due to this off-axis, fringes appear in the interference pattern which have certain frequency. Note, to record the fringes in the interference pattern properly at the far-field, one needs to have a camera with a pixel width smaller than the spacing between the fringes. More precisely pixel width of a camera should satisfy the Nyquist frequency criteria.

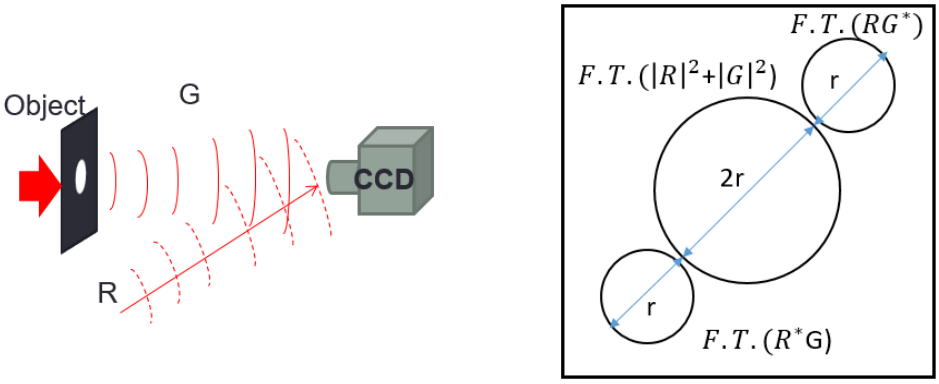

(a) (b)

Figure 1.3: (a) Optical setup for recording off-axis hologram at the far-field, (b) distribution in the reconstruction plane.

By the introduction of the slight angle between the object and reference fields, one can separate the four terms mentioned in the equation (1.9) in the reconstruction plane, which can be obtained by performing a two dimensional Fourier transform operation on the recorded intensity. The distribution in reconstruction plane is shown in figure 1.3 (b). From this figure, one can see that, for an object having size r, the combination of first and second terms of equation (1.9), covers twice the size of the object i.e., $2r$ in the reconstruction plane, 3rd and 4th terms spread and cover an area of size r and are located diagonally opposite to each other. According to figure 1.3 (b), in order to separate the terms from one another, there needs to be a minimum separation of 1.5 times the object's size between object and the reference point source in off-axis holography. Since reconstruction plane has a limited size, this means that object with certain size only can be reconstructed fully without any

overlapping in a single shot. Therefore, field of view is restricted in off-axis holography.

1.2.5.2 In-line holography

In the inline holography shown in figure 1.4 (a), the highest frequency content in the interference pattern formed at the camera plane is determined by the scattered lights coming from the farthest two points of the object i.e., size of the object r. While for the same object in off-axis hologram, it is coming from the interference of lights from reference point and the farthest point of the object (2 times the object size). Therefore, as compared to in-line holography, one claims that in off-axis holography, field of view is restricted by a factor of 4 and sampling of the off-axis hologram has to be perform twice as fast.

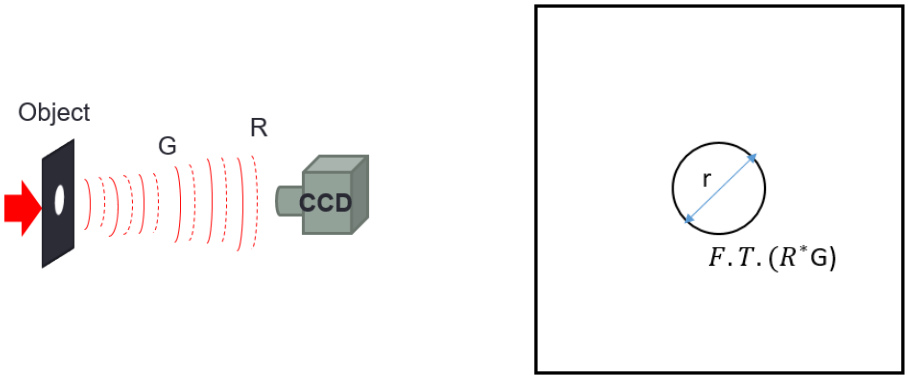

Figure 1.4 (a): Optical setup for in-line holography, (b) distribution in the reconstruction plane.

In the in-line holography, to retrieve the object information from the hologram recorded at the far-field, one has to record multiple intensities of the interference pattern by varying the phase of the reference field in steps. From the multiple intensities one can obtain the desired term or the 3rd term as mentioned in equation (1.9) and reconstruction of object is achieved by performing the Fourier transform operation. This process is known as the phase shifting technique. However, during the recording procedure, the concerned object should remain stable. Therefore, in-line holography is applicable only for the static object.

1.2.5.3 Phase retrieval iterative algorithm

Phase retrieval algorithm (PRA) is a numerical iterative method to retrieve a complex object from far-field intensity pattern recorded at the Fourier plane. This method requires no separate reference source; therefore, it employs a simple optical setup as compared to the holography. Moreover, since it does not require a separate reference source; the highest frequency content in the interference pattern is determined by the scattered lights coming from the outermost points of the object i.e., size of the object r. Therefore, in PRA angle is reduced twofold as compared to the off-axis holography. Besides, in the reconstruction plane, only autocorrelation term is present which covers twice the size of the object; therefore, one obtains two times higher field of view as compared to off-axis holography. However, owing to the fact that a random guess is employed in most of the PRA algorithms as an initial estimation of the object that differs in different trails of the algorithms, occasionally it results in non-deterministic output. Further, sometimes the reconstruction output shows the signature of the object and its twin (complex conjugate and inverted) simultaneously, resulting in a twin image problem. Furthermore, since this method is an iterative approach, the reconstruction takes some time to converge. Hence, it is hard to use this method in real-time situation.

1.2.6 Optical setup

Since in the existing techniques such as holography, owing to the fact of using separate reference source, optical setup becomes complicated and sensitive to external vibration, restricts its application in real-time NDT in the vibrational environment. On the other hand, PRA can be insensitive to external vibration; however, sometimes the output of the algorithm varies in different trails, and occasionally it suffers from the twin image problem.

In this thesis, simple methods are developed which produce unique output that are as good as obtained with the holography and use a simple optical setup similar to the PRA without incorporating a separate reference source. In the proposed methods, one should record the far-field intensity of an object, and from the recorded intensity, one can easily obtain an autocorrelation of the object by

performing a Fourier transform operation numerically. All the way through the thesis, the autocorrelation of the object is utilized to retrieve the complex object.

1.3 Motivation

Although the off-axis and in-line holography techniques reconstruct the complex object i.e., amplitude and phase information, however, each one has some disadvantages. In addition to this, in both techniques reference field should be maintained stable during the recording process. Therefore, both the techniques work well within a stable environment where one should isolate the external vibration. Therefore, holography is not suitable in a practical scenario where one cannot control the external vibration. To solve the limitation of the holography, one should modify the optical setup and develop numerical methods in such a way that reconstruction of the complex object can be achieved without using the separate reference field. In addition, quality of the reconstruction from such methods should also be better as compared to the existing methods; moreover, such methods should be robust and suitable in vibrational environmental.

1.4 Outline of the thesis

In some applications, as mentioned at the beginning of this chapter, one has to retrive amplitude as well as the phase part of a field scattered from the object. Besides, it is also pointed out that existing techniques such as off-axis and in-line holography fulfill the objective; however, at the cost of some drawbacks, which are described earlier. In this thesis, several methods are proposed to overcome those limitations. In most of the proposed methods in this thesis, to keep the setup robust, novel, simple, common path geometries for the optical setups for recording the intensity pattern are designed and developed. Most importantly, like the holography where a separate reference field is required, which makes the setup vulnerable to the vibration is not present in the proposed schemes, resulting in minimizing the effect of the external vibration.

In the second chapter, a very simple design has opted for the recording procedure, where a single CCD camera is placed at the Fourier plane to record the intensity of the scattered field of the object at the far-field. Since, as mentioned before, the camera records only the intensity, the phase part of the field gets lost during the

recording procedure. In order to retrieve the complex object i.e., amplitude and phase, a phase retrieval iterative algorithm is employed. However, since far-field intensity is same for object and its conjugate inverted or twin self, the execution of the PRA on different trails occassianlly reconstructs different outputs, sometimes it reconstructs object, some other time twin and at another instance object-twin both simultaneously. When the output contains the signature of the object as well as its twin it is known as the twin image problem. Besides, to start the PRA, a random initial guess is used, results in varying the algorithm output sometimes as the algorithm is executed multiple times. In order to provide twin image free unique solution, a novel method is discussed in chapter 2, which incorporates the asymmetry of the object. A detailed analysis along with simulation and experimental results are provided for the proof of principle.

The method proposed in chapter 2 works well only for the objects having the direction of asymmetry. In addition, the existing PRA technique with the random guess as an initial estimation sometimes shows a fast convergence rate, produces less reconstruction error and retrieves high quality output compared to the method proposed in chapter 2. Therefore, in the third chapter, another PRA method is proposed where area near the edge of the object is illuminated using an additional beam, the proposed technique is named as PRA with edge point referencing (PRA-EPR). By utilizing the EPR in the PRA, asymmetry is created in the illumination beam itself. Therefore, irrespective of the asymmetry of the object, the reconstruction produces unique and twin-image free object with a fast convergence rate.

In the fourth chapter, a novel PRA method is suggested, where without utilizing the asymmetry of the object and any modification in the illumination beam, one can retrieve the complex object information. The method provides very promising results; however, it is limited to the ‘special object’ containing object and its twin located at a certain distance away from each other. This kind of ‘special object’ is realized in the case of volumetric holographic data storage and reconstruction (VHDSR). VHDSR technique is used to store huge data on a small volume using the holographic principle. Most of the existing VHDSR methods reconstruct only the amplitude part of the object. While the proposed method based on PRA provides

a way to store and retrieve complex object, therefore the same volume can be utilized to store and retrieve twice the data.

In the early development of the phase retrieval iterative algorithm, researchers have employed a photograph of the object along with the intensity of the object recorded at the Fourier plane. However, this technique needs to capture two shots of the object; therefore, the existing approach is not applicable for real time dynamic objects. In recent years researchers have utilized holography in the PRA, where the low resolution image obtained from the holography is used as an initial guess in the PRA. However, by incorporating the holography in the PRA, drawbacks associated with the holography will also affect the reconstruction. Therefore, in the fifth chapter, a novel and simple PRA method is proposed where a photograph of the object is captured alongside the intensity of the object at the Fourier plane. Additionally, a novel optical setup is proposed for capturing two distributions in a single shot by dividing the camera screen into two parts.

From chapter 2 to 5, the iterative PRA methods are incorporated, that deliver promising results by running the algorithm for few iterations. In chapter 6, a non-iterative method is proposed by incorporating the EPR and developing a novel experimental setup. Apart from this, the capability of the proposed setup is also tested on various objects e.g., two dimensional and three dimensional objects, the theoretical derivation is also carried out for the proof of concept. Moreover, how this method can be utilized for real time deformation measurement is further discussed.

In the last chapter, a novel non-iterative method is developed by modifying the method proposed in chapter 6, for measuring the deformation of an object in real time.

1.5 Holography vs Edge Point Referencing

In this section, we are going to highlight major differences between the holography and edge point referencing schemes.

In the holography scheme, under the ideal condition when there is no vibrational effect, holography equation can be written as follow

$$I = |G|^2 + |R|^2 + R^*G + G^*R. \tag{1.10}$$

Where G and R represent the fields scattered from the object and reference source.

Under the vibration, according to the setup shown in figure 1.5 (a), since object and reference fields are independent from each other, object can oscillate independently from the reference or vice versa. This introduces a random phase $e^{i\emptyset(t)}$ in the object field which depends on the time t, by considering this factor interference equation in the holography can be written as follow

$$I = |G|^2 + |R|^2 + R^*e^{i\emptyset(t)}G + G^*Re^{-i\emptyset(t)}. \tag{1.11}$$

One can see that in the reconstruction or 3rd term of equation (1.11) i.e., $R^*e^{i\emptyset(t)}G$, extra phase factor appears which produces a constant phase distribution over the object phase in the reconstruction. On top of that, this random factor depends on the time, hence, reconstructions of the phase of the same object in different trails retrieve different phases, results in repeatability problem in the holography. Besides, if object is located far from physical reach to put a reference point near the object is not possible. Moreover, when object is located far from reach, matching the coherence length between the reference and object fields is also a major problem.

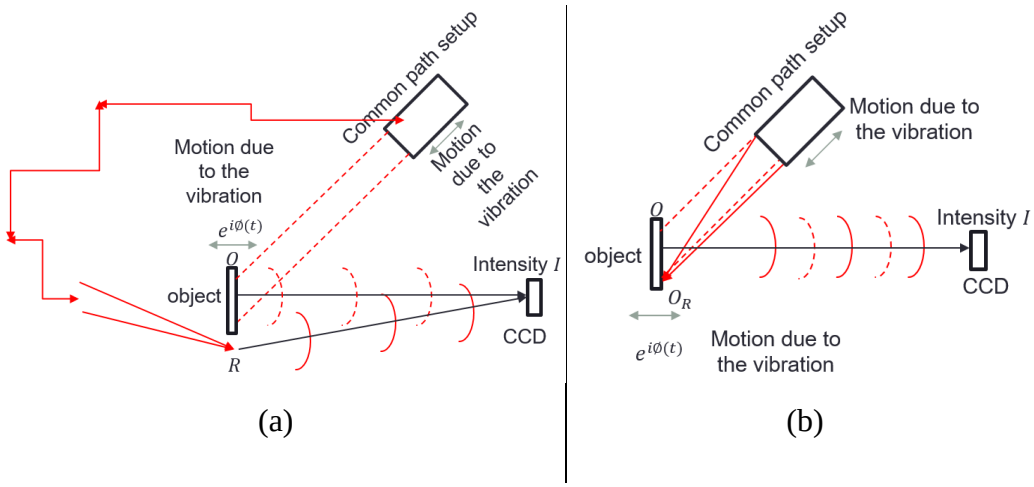

Figure 1.5: Setup for (a) Holography, (b) Edge point referencing.

In the edge point referencing scheme, considering ideal condition, interference equation can be written as

$$I = |G|^2 + |G_R|^2 + GG_R^* + G^*G_R. \quad (1.12)$$

Where G and G_R represent the fields scattered from object O and edge point of the object O_R.

In EPR, according to the figure shown in 1.5 (b), since edge point of the object is acting as a reference field, due to the vibration, when object moves reference field also moves accordingly. This introduces almost equal random phase $e^{i\emptyset(t)}$ in the reference field as well in the object field, which depends on the time t, by considering this factor, interference equation can be written as follow

$$I \approx |G|^2 + |G_R|^2 + Ge^{i\emptyset(t)}G_R^*e^{-i\emptyset(t)} + G^*e^{-i\emptyset(t)}G_Re^{i\emptyset(t)}. \quad (1.13)$$

Rewriting equation (1.13)

$$I \approx |G|^2 + |G_R|^2 + GG_R^* + G^*G_R. \quad (1.14)$$

One can see that in the reconstruction or 3rd term in equation (1.14) i.e., GG_R^*, extra phase factor does not appear, which confirms the immunity against the external vibration. Additionally, a common path setup is utilized for the generation of the beams; therefore, even if entire common path setup moves, it introduces almost identical phases in both the beams, i.e., converging beam for illuminating the edge point of the object and plane beam for illuminating a desired portion of the object. Objects which are located far-from physical reach can also be measured. Due to the common path setup and edge point referencing, object and reference fields are located at the same plane; therefore, coherence length is automatically matched.

1.6 Common path setups

There are several ways for creating common path setups to generate the beams for the edge point referencing. One way is to utilize a neutral density (ND) filter, which has a uniform coating throughout its region except near the periphery. By placing this ND filter in front of a collimated laser beam, one can reduce the beam intensity throughout the beam except at the location where the coating is absent; then, 4f geometry can be utilized for imaging the ND filter plane onto the object plane as shown in figure 1.6 (a). Second way is to place a spatial light modulator (SLM) in front of a collimated laser beam. SLM is generally sensitive to one polarization; therefore, it can only modulate a certain type of polarization, let say x polarization.

By illuminating it with 45 degree polarized light; which has both x and y polarization states, one can generate two beams. One is modulated or diffracted (x polarized) and the other one is unmodulated i.e., undiffracted (y polarized). Unmodulated beam reflects from the SLM as it is, while the modulated beam can be modified according to our need by creating a phase pattern and loading it onto the SLM screen. For the edge point referencing, these two beams can be made collimated and converged respectively as illustrated in figure 1.6 (b).

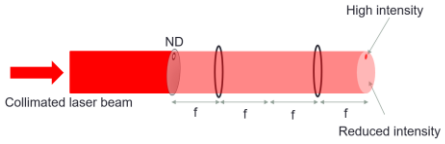

(a)

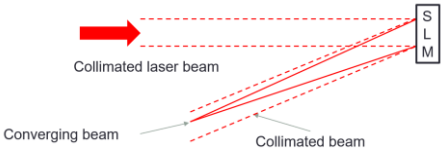

(b)

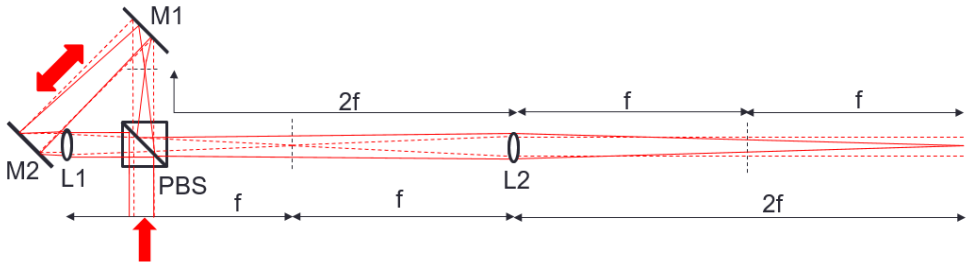

(c)

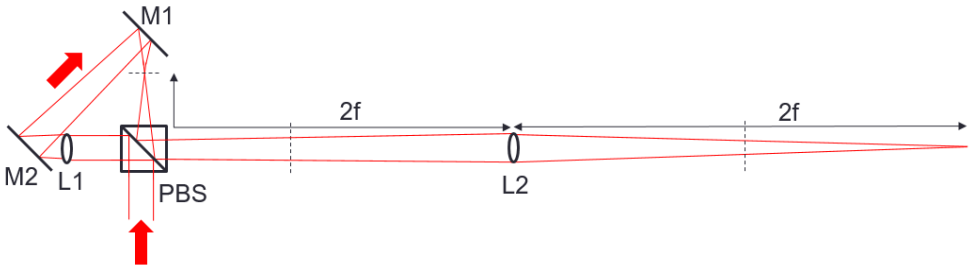

(d)

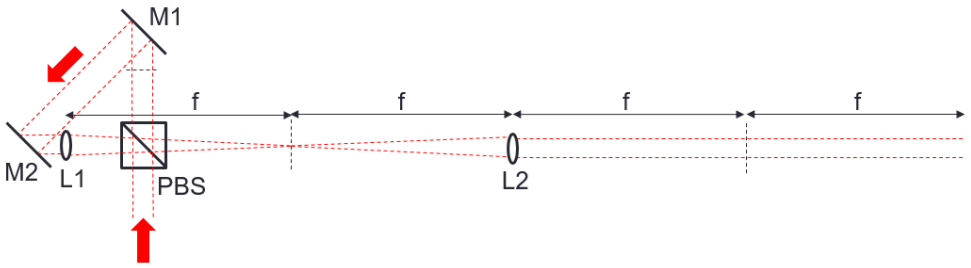

(e)

Figure 1.6: Common path setups for generating edge point referencing (a) using a ND filter, (b) using a spatial light modulator, and (c) using optical components, paths taken by the light reflected and transmitted from the PBS in figure (c) are shown in (d) and (e), respectivly.

The two methods shown in figures 1.6 (a) and (b) are limited only if one has the access of ND filter or the SLM. In figure 1.6 (c), a simple approach is presented for generating beams suitable for EPR using optical components. By employing a common path Sagnac and 4f geometry using two lenses L1 and L2 and designing the setup shown in figure 1.6 (c), one can generate such beams. The beam reflected from the PBS shown in figure 1.6 (c) follows the path as shown in figure 1.6 (d). Similarly, the path taken by the transmitted beam is shown in figure 1.6 (e). Since in all the three cases as mentioned before, both the beams encounter same number of optical elements, even if all the components oscillate due to the vibration the relative phase between the two beams remains almost stable.

1.7 Conventions

Throughout the thesis, amplitude functions e.g. intensity and photograph have only the amplitude values, while complex functions e.g., autocorrelation and complex object have amplitude as well as phase distribution. Therefore, amplitude functions are displayed with only one pattern, whereas complex functions are shown with two separate distributions representing amplitude and phase, respectively. Further, all the images are represented by a two dimensional matrix having multiple pixels. In most of the cases amplitude images are normalized between the value 0 to 1, representing minimum and maximum values of the pixels, and these values are represented by black and white colors and in between values by gray colors, respectively. On the other hand, phase images are normalized either between $-\pi$ to π or between $-\pi/2$ to $\pi/2$ (mention in the respective sections), indicating minimum and maximum value of the pixels, and these values are shown with black and white colors and in between values with the gray colors, respectively. This convention is used throughout the thesis for the displaying the amplitude and phase images. Apart from this, size of the images along with the number of iterations used for processing is also mentioned in the respective section. In addition, to execute

the proposed algorithms in the thesis and to calculate the processing times, a system is used having the following specifications: Processor Intel(R) Core(TM) i5-3470 CPU @ 3.20GHz 3.20 GHz, RAM 12.0 GB (11.8 GB usable), Window 8, 64 bit Operating System, x64 based processor.

Chapter 2

Single-shot and twin-image free unique phase retrieval using an aspect of autocorrelation that considers the object asymmetry

A phase retrieval algorithm can reconstruct the phase of an object from an intensity of a diffraction pattern recorded at the Fourier plane provided; one makes a right initial guess. For the algorithms which are based on an initial random guess, at times, the output either becomes non-deterministic, non-convergence or develops twin-image. For improving the performance of the algorithms by eliminating the twin-image and for bringing uniqueness to the output, prior information about the object or more number of intensity measurements is needed. In order to achieve it using only a single acquisition of the intensity pattern recoded at the Fourier plane for an object, here a method is proposed in which object support along with the object information provided object has a direction of asymmetry can be measured from the object autocorrelation and utilized as an initial guess in the phase retrieval algorithm. In the process, how even a partial asymmetry in the object distribution can lead to a good solution in the phase retrieval algorithm is also explored. This method is beneficial for unique phase detection without any twin artifact in various fields of optics. In this chapter, the proposed method is theoretically analyzed and validated by carrying out the simulations and experiment.

2.1 Introduction

In some applications such as astronomy, x-ray crystallography, wavefront sensing, electron microscopy and biomedical imaging; phase part of the object contains valuable information. In these cases, camera and photographic plates are employed for recording the diffraction pattern of the object. However, since these devices record only the intensity, phase part of the field gets lost during the recording. To reconstruct the phase of an object from the intensity of the diffraction pattern recorded at the Fourier plane or equivalently, from the object

autocorrelation, generally, digital holography [7] or phase retrieval algorithm (PRA) [8] is used. In holography, an interference pattern or hologram is created, by introducing a separate reference beam. Depending on the choice of the reference, these holography techniques can be divided into two categories: 1) single shot off-axis holography [9] and 2) multiple shots in-line holography [10]. PRA, on the other hand, is a simple iterative computational technique that does not require separate reference beam and complicated setup as that used in the holographic techniques. However, PRA is an iterative method and requires constraints in the object as well in the Fourier domain as a priori information.

Since the object $g(r)$ or its twin (complex conjugate and inverted) $g^*(-r)$ generates a similar intensity pattern at the Fourier plane, reconstruction from PRA is known to suffer from the twin-image problem [11] especially for the asymmetric object where $g(r) \neq g^*(-r)$. With twin-image problem, the reconstruction shows the features of both the desired object as well as its twin. Besides, this problem worsens when the object is bounded with the centrosymmetric aperture. For eliminating the twin-image problem from the reconstruction, some prominent solutions have been proposed in the literature. T.R. Crimmins et al. have suggested a method of finding the object support as prior information from the object autocorrelation [12]. The effect of object support on object reconstruction in case of tight or loose has also been discussed [13]. However, a priori information of the object support does not ensure that object can be uniquely reconstructed [14]. T. Latychevskaia et al. [15] have suggested another approach, where the diverging beam is employed for illuminating the object. Owing to the diverging nature of the beam, object and its twin image get separated in the reconstruction at different longitudinal planes. And by filtering one of the planes and using it into the iterative algorithms one can obtain the desired object without the twin-image. This method is difficult to use in x-ray crystallography where the distance between the planes is very small. Another method has been proposed [16], which employs a reduced-support constrains where object support mask is replaced with a non-centrosymmetric mask that is a subset of the original object support for few initial iterations. This results in the enhancement of one of the two possible solutions over the other. And subsequent iterations with full object support lead to the solution, free from the twin-image. While another method [17], proposes a sparsity assisted, where a sparsity-enhancing step is introduced in the iterative algorithm for

removing the twin-image. In addition to twin-image problem, the output of PRA algorithms is not unique but occasionally varies owing to a random guess as an initial estimation of the object. To overcome the non-uniqueness along with the twin-image problem, some methods use more number of recording i.e. transport of intensity method [18] or off-axis holography technique [19] to assist the PRA. In both of these methods, the initial random guess is replaced by the measured object phase. By incorporating the measured phase, one can reconstruct objects uniquely without twin-image and with faster convergence rate.

Is there a possibility to obtain object information without recording its multiple shots or off-axis hologram? The answer to this question is yes. In this chapter, a PRA method is proposed in which object support along with the object information in case the object has a direction of asymmetry can be measured from the object autocorrelation. This information fed to the PRA as an initial guess to ensure the twin-image free unique solution. Object autocorrelation can easily be obtained from the intensity recorded at the Fourier plane without requiring any additional measurement. Since object autocorrelation is the result of object convolved with its twin, in addition to object support, it also contains information about the object itself [20]. Besides, in contrasts to the existing studies, the conditions that is used in the method are naturally present in the coherent illumination of an object. In the simulations as well in the experiment, plane beam illumination is employed as opposed to the fabricated condition used in reference [15], and circular symmetric bound as opposed to synthetic support used in reference [8], Under such conditions, removing the twin-image problem has been considered to be much more difficult. In this chapter, the well-known Fienup Hybrid Input-Output (HIO) [21] [13] phase retrieval algorithm is utilized.

2.2 Principle

Consider an object being illuminated with a uniform plane coherent circular beam of radius r_o. The size of the illumination beam is selected to be smaller than the object dimension. The desired object $g(r)$ (confined within the illumination) can be treated as a composition of several points. To investigate the effect of these points of the object and the role of asymmetry in the object and how it encodes the object information on the object autocorrelation, two small circular portions $P_1(r_o, \theta - 180)$ and $P_2(r_o, \theta)$ on the object are considered. Their centres

are located at r_o distance away from the origin and oriented opposite to each other at $\theta - 180$ and θ with respect to the x axis as shown in figure 2.1 (a). Mathematically, the desired object can be written as follows,

$$g(r) = g'(r) + \sum_{r_i \in P_1(r_o, \theta - 180)} g(r_i)\delta(r - r_i) + \sum_{r_i \in P_2(r_o, \theta)} g(-r_i)\delta(r + r_i) \quad (2.1)$$

Where $r = (x, y)$ is the position vector at the object plane, $g'(r)$ represents the remaining part of the desired object excluding two portions $P_1(r_o, \theta - 180)$ and $P_2(r_o, \theta)$. Object points that lie in these small portions are denoted by Dirac delta functions as $\sum_{r \in P_1(r_o, \theta - 180)} g(r_i)\delta(r - r_i)$ and $\sum_{r \in P_2(r_o, \theta)} g(-r_i)\delta(r + r_i)$ with complex amplitudes $g(r_i)$ and $g(-r_i)$ respectively.

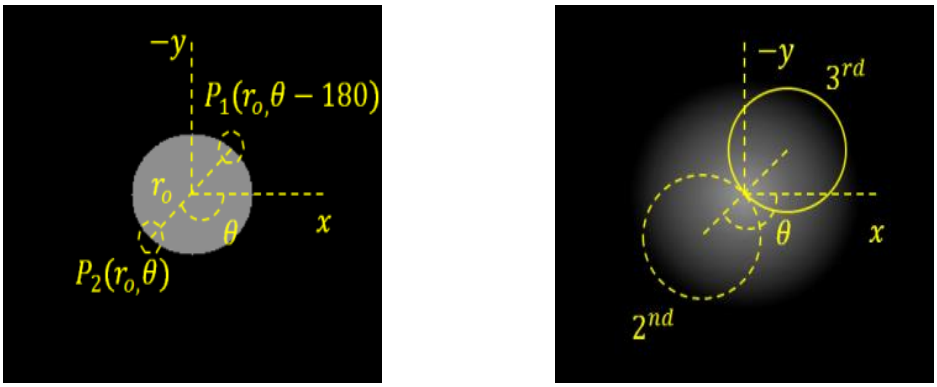

(a) (b)

Figure 2.1: (a) complex object bounded with radius r_o where $P_1(r_o, \theta - 180)$ and $P_2(r_o, \theta)$ show the two small circular portions of the desired object, located r_o distance away from the origin and oriented at $\theta - 180$ and θ degree respectively with respect to the x axis , (b) object autocorrelation, dotted and solid circles show the locations of 2nd and 3rd terms mentioned in the equation (2.5).

The diffraction field of the object $g(r)$ at the Fourier plane can be obtained by simply taking its Fourier transform as,

$$G(k) = F.T.[g(r)]. \quad (2.2)$$

Where $G(k)$, k and $F.T.$ represent the diffraction field at Fourier plane, two dimensional wave vector and Fourier transform operator respectively. Let us suppose a camera is present at the Fourier plane to record the intensity of the diffraction pattern, which can be written as,

$$I = |G(k)|^2 . \tag{2.3}$$

The numerically inverse Fourier transform of the diffraction pattern can be described as,

$$\tilde{g}(r) = I.F.T.(I) = g(r) \otimes g^*(-r) . \tag{2.4}$$

Where $\breve{g}(r)$ represents the autocorrelation of the desired object, $\otimes$ represents the convolution operation, and $I.F.T.$ denotes the inverse Fourier transform operator. Since the desired object is confined within the illumination of radius of r_o , object autocorrelation spans in a circular region of radius $2r_o$. Thus, from the size of autocorrelation, object support $S(0,0)$ information that spans in the circular aperture of radius r_o (half the size of object autocorrelation), can be measured for further analysis. Using equations (2.1) and (2.4) object autocorrelation can be expanded as follows,

$$\begin{aligned} \tilde{g}(r) = o(r) + & \left(\begin{array}{c} \sum_{r_i \in P_1(r_o, \theta-180)} \left[\left\{ g'(r) g^*(r_i) \right\} \otimes \delta(r + r_i) \right] + \\ \sum_{r_i \in P_2(r_o, \theta)} \left[\left\{ g'^*(-r) g(-r_i) \right\} \otimes \delta(r + r_i) \right] \end{array} \right) + \\ & \left(\begin{array}{c} \sum_{r_i \in P_2(r_o, \theta)} \left[\left\{ g'(r) g^*(-r_i) \right\} \otimes \delta(r - r_i) \right] + \\ \sum_{r_i \in P_1(r_o, \theta-180)} \left[\left\{ g'^*(-r) g(r_i) \right\} \otimes \delta(r - r_i) \right] \end{array} \right). \end{aligned} \tag{2.5}$$

Where $o(r)$ represents the remaining multiplication terms present in the autocorrelation and can be written as follows

$$o(r) = g'(r) \otimes g'^{*}(-r) + \left[\sum_{r_i \in P_1(r_o, \theta-180)} g(r_i)\delta(r - r_i) \otimes \left\{ \begin{array}{l} \sum_{r_i \in P_1(r_o, \theta-180)} g^{*}(r_i)\delta(r + r_i) + \\ \sum_{r_i \in P_2(r_o, \theta)} g^{*}(-r_i)\delta(r - r_i) \end{array} \right\} \right] + \left[\sum_{r_i \in P_2(r_o, \theta)} g(-r_i)\delta(r + r_i) \otimes \left\{ \begin{array}{l} \sum_{r_i \in P_1(r_o, \theta-180)} g^{*}(r_i)\delta(r + r_i) + \\ \sum_{r_i \in P_2(r_o, \theta)} g^{*}(-r_i)\delta(r - r_i) \end{array} \right\} \right]. \quad (2.6)$$

In the equation (2.6), first term shows the convolution of $g'(r)$ with its twin and second term shows the region $P_1(r_o, \theta - 180)$ convolved with its twin itself and with the twin of region $P_2(r_o, \theta)$. Similarly third term represents the region $P_2(r_o, \theta)$ convolved with twin of $P_1(r_o, \theta - 180)$ and $P_2(r_o, \theta)$ respectively. Term $o(r)$ and the 2nd and 3rd terms (inside the round brackets) in equation (2.5), create the object autocorrelation as shown in figure 2.1 (b). In the equation (2.6), first term forms the background distribution; in addition to the background, 2nd and 3rd terms in equation (2.5) form the distributions as shown in figure 2.1 (b) by the dotted and solid circles, respectively. Since the size of the portions $P_1(r_o, \theta - 180)$ and $P_2(r_o, \theta)$ is considered to be smaller than $g'(r)$, information of object is encoded in the object autocorrelation, mainly by the 2nd and 3rd terms mentioned in equation (2.5), compared to the 2nd and 3rd terms (inside the square brackets) mentioned in equation (2.6). Therefore, in the subsequent paragraph, 2nd and 3rd terms mentioned in equation (2.5) are emphasized more.

As can be seen clearly from equation (2.5), location and amplitude (strength) of 2nd and 3rd terms (inside the round brackets) are decided by the location and the amplitude of the corresponding object points which are lie in portions $P_1(r_o, \theta - 180)$ and $P_2(r_o, \theta)$. Locations of these two portions can be chosen anywhere within the desired object, however, for the two portions that are located at the opposite locations and near the periphery of the desired object, the 2nd and 3rd terms are well separated as shown in the figure 2.1 (b) by dotted and solid circles respectively. Therefore, a portion, corresponding to 2nd term from the object autocorrelation, is filtered out using the measured object support by locating $S(0,0)$ to $S(r_o, \theta)$ location. The filtered term from equation (2.5) can be written separately using $g(r_i) = |g(r_i)|\, e^{i\varphi(r_i)}$ and $g(-r_i) = |g(-r_i)|\, e^{i\varphi(-r_i)}$ as follow,

$$f_\theta(r) \propto S(r_o,\theta)\times\left(\begin{array}{c}\sum_{r_i\in P_1(r_o,\theta-180)}\left[\left\{g'(r)|g(r_i)|e^{-i\varphi(r_i)}\right\}\otimes\delta(r+r_i)\right]+\\ \sum_{r_i\in P_2(r_o,\theta)}\left[\left\{g'^*(-r)|g(-r_i)|e^{i\varphi(-r_i)}\right\}\otimes\delta(r+r_i)\right]\end{array}\right). \quad (2.7)$$

Where $S(r_o,\theta)$ indicate the object support with radius r_o and centred at r_o and oriented at θ degree and $f_\theta(r)$ represents the portion filtered out using $S(r_o,\theta)$. In the filter region, points that lie in region $P_1(r_o,\theta-180)$ create $g'(r)$ while points lying in region $P_2(r_o,\theta)$ generate $g'^*(-r)$. As long as the object is asymmetric, amplitudes of points lying in $P_1(r_o,\theta-180)$ and $P_2(r_o,\theta)$ portions are not going to be same i.e., $\sum_{r_i\in P_1(r_o,\theta-180)} g(r_i) \neq \sum_{r_i\in P_2(r_o,\theta)} g(-r_i)$, by following equation (2.7), it leads to different proportion of $g'(r)$ over its twin $g'^*(-r)$ in $f_\theta(r)$. If this filter out portion is used in any existing PRA algorithms, depending on the strength of the object points lying in regions $P_1(r_o,\theta-180)$ and $P_2(r_o,\theta)$, either PRA converges to upright $\sum_{r_i\in P_1(r_o,\theta-180)}|g(r_i)| > \sum_{r_i\in P_2(r_o,\theta)}|g(-r_i)|$ or the conjugated and inverted $\sum_{r_i\in P_1(r_o,\theta-180)}|g(r_i)| < \sum_{r_i\in P_2(r_o,\theta)}|g(-r_i)|$ but never to both. If 3rd term is selected, instead of 2nd term in the equation (2.5), and follow the same derivation, one can find that the last two aformetioned conditions are opposite i.e., conjugated and inverted will be reconstructed if $\sum_{r_i\in P_1(r_o,\theta-180)}|g(r_i)| > \sum_{r_i\in P_2(r_o,\theta)}|g(-r_i)|$ however, the upright will be reconstructed if $\sum_{r_i\in P_1(r_o,\theta-180)}|g(r_i)| < \sum_{r_i\in P_2(r_o,\theta)}|g(-r_i)|$ for some direction θ. For better understanding, the above derivation can also be derived considering two points instead of the two circular portions as discussed in Appendix A. In the subsequent sections, simulations are provided for the validation.

2.3 Simulation, results and discussion

For simulation, a complex object using distributions of letter 'A' and letter 'P' as an amplitude and phase information is created. These patterns are bounded with a support of circular aperture of radius 40 pixels as shown in figures 2.2 (a) and (b). To show the effect of symmetry and asymmetry of the object on the PRA reconstruction, amplitude of object is chosen such that it is symmetric with respect to the y axis i.e., left portion is the mirror image of right portion. Additionally, about the x axis, object is asymmetric, i.e., top portion is different from bottom part. For further analysis, object asymmetry is formalized as,

$$OAF = \left| \frac{\sum_{r_i \in P_1(r_o,\theta-180)} |g(r_i)|^2 - \sum_{r_i \in P_2(r_o,\theta)} |g(-r_i)|^2}{\sum_{r_i \in P_1(r_o,\theta-180)} |g(r_i)|^2 + \sum_{r_i \in P_2(r_o,\theta)} |g(-r_i)|^2} \right|^{1/2} . \quad (2.8)$$

Where OAF defines as object asymmetry factor for the two portions $P_1(r_o, \theta - 180)$ and $P_2(r_o, \theta)$ of the object $g(r)$ along the direction θ. If $OAF \approx 0$ at certain direction θ then given portions are almost symmetric otherwise if $OAF > 0$, portions are asymmetric along that direction.

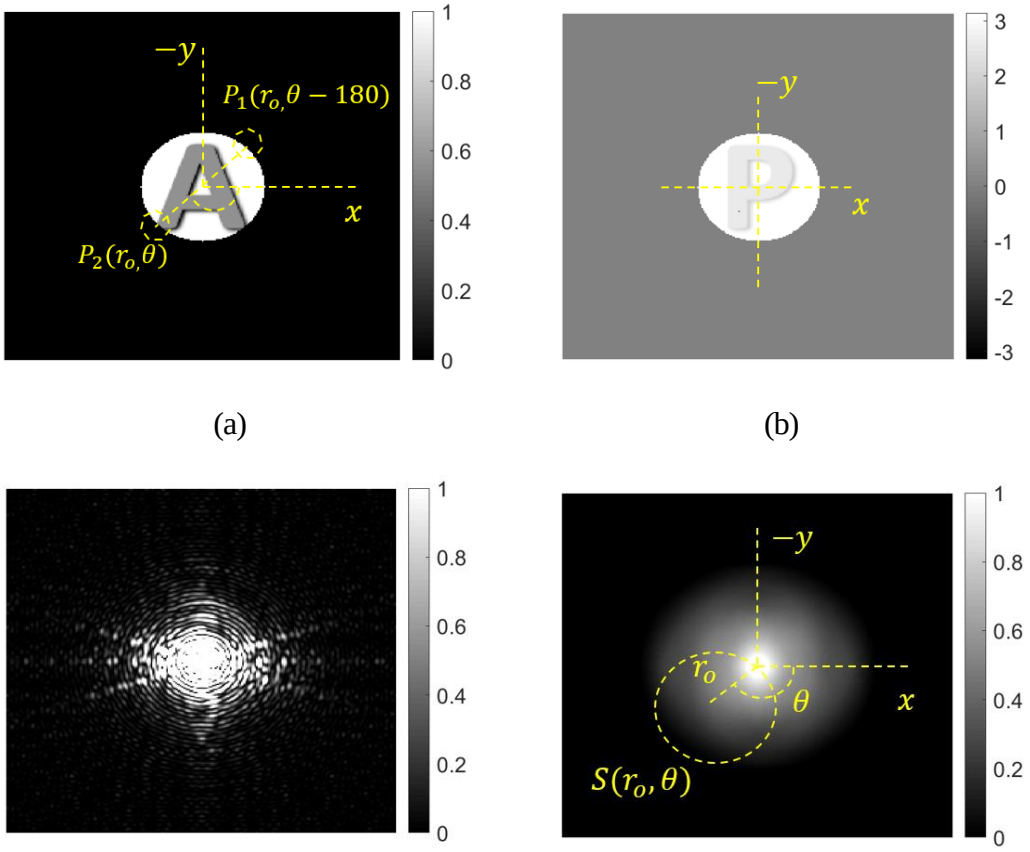

(a) (b)

(c) (d)

Figure 2.2: Images of (a) Letter 'A' (mirror symmetry about the y axis and asymmetry about the x axis) and (b) Letter 'P', representing the object amplitude and phase used in the PRA respectively, (c) intensity recorded at the Fourier plane, (d) object autocorrelation, dotted circle shows the $S(r_o, \theta)$.

The intensity recorded at the Fourier plane is shown in figure 2.2 (c). And the object autocorrelation obtained from the intensity pattern is shown in figure 2.2 (d). From this figure, it can be observed that the size of the autocorrelation is exactly twice the size of the object for more detail refer Appendix B. Thus, the circular object support $S(0,0)$ with radius $r_o = 40$ pixels is measured from the object autocorrelation. Lastly, position for filtering is selected by shifting and orienting $S(0,0)$ to $S(r_o, \theta)$ location and then sweeping it across the object autocorrelation keeping the centre of $S(r_o, \theta)$ fixed at r_o from the origin and by varying the direction θ. In order to find the location for superior reconstruction, all the filtered out portions are used one by one as an initial estimation for the Fienup HIO PRA algorithm, the flow diagram of the algorithm is given in Appendix D. In the algorithm, $S(r_o, \theta)$ and square root of intensity with feedback factor $\beta = 1$ as an object domain and Fourier domain constraints are utilized.

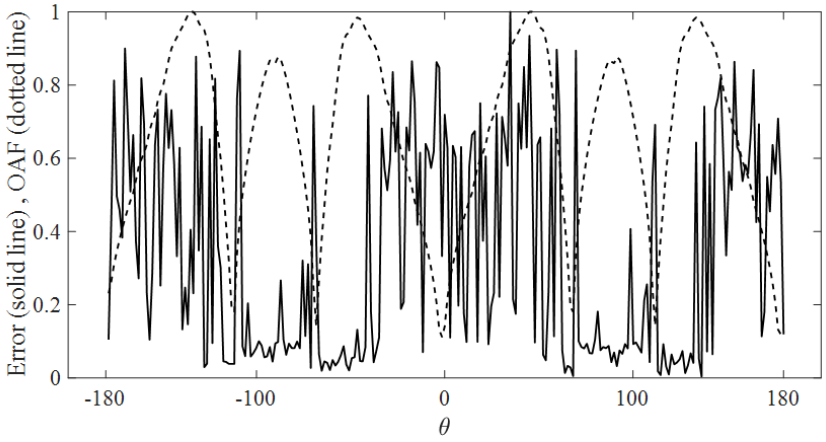

(a)

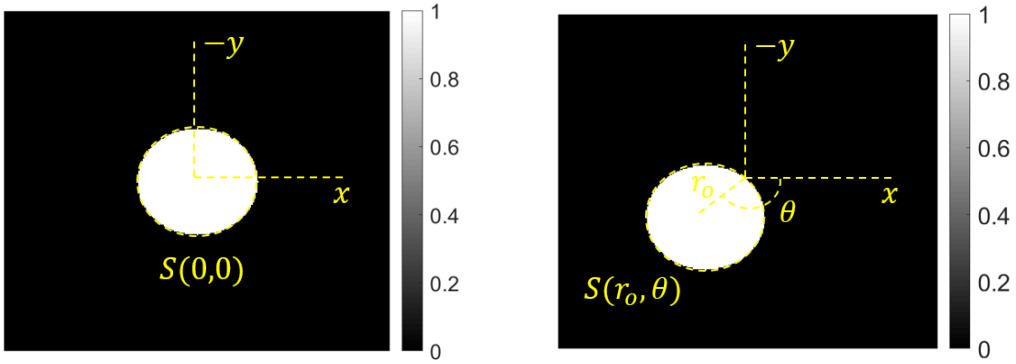

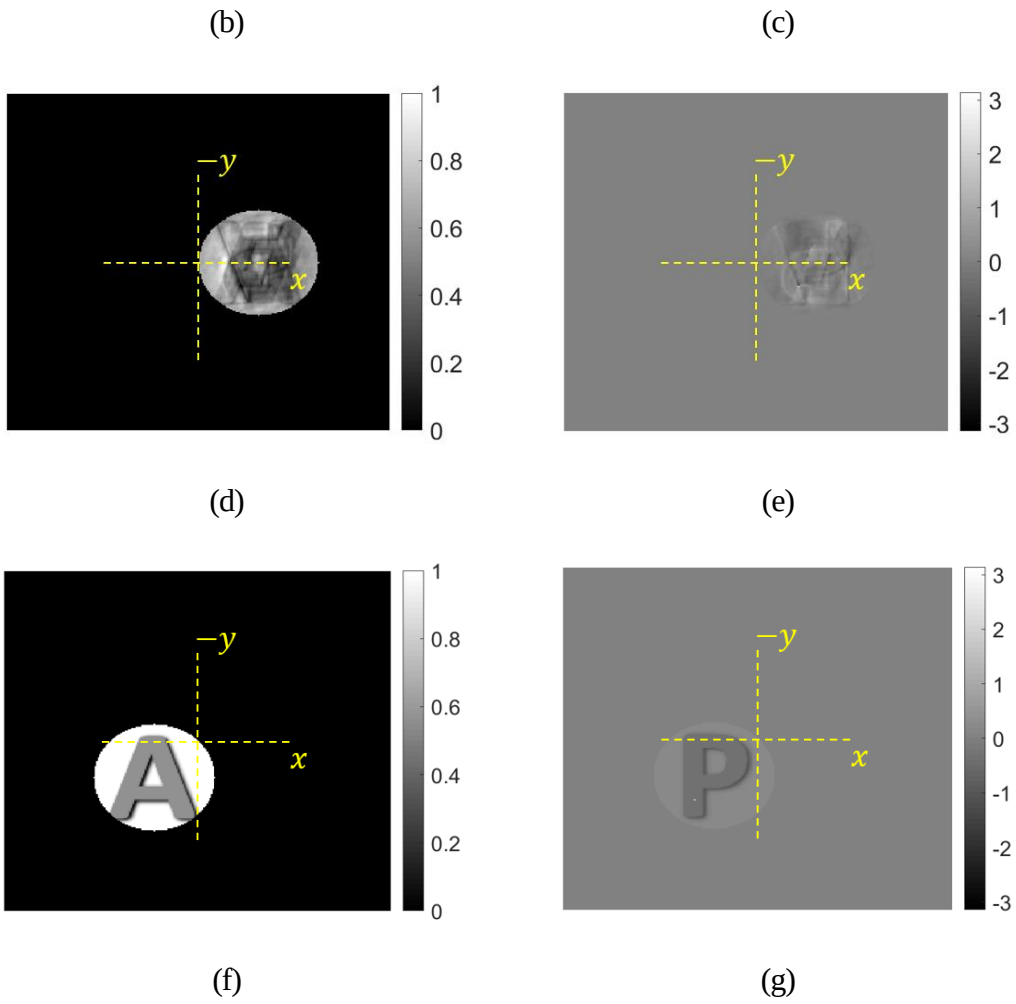

Figure 2.3: (a) Solid curve shows the error in the output after 1000 iterations with respect to the direction θ; the direction from which the filtered section is cropped using object support $S(r_o, \theta)$; dotted line shows the object asymmetry factor measured along these orientations. (b) Object support $S(0,0)$ at origin, (c) object support $S(r_o, \theta)$ with its center shifted at r_o and oriented at θ, white color shows the location of the points which are inside the region $S(r_o, \theta)$, i.e. $r \in S(r_o, \theta)$ and black color shows the location of the points that lie outside the $S(r_o, \theta)$, i.e. $r \notin S(r_o, \theta)$. (d) and (e) correspond to the retrieved amplitude and phase information, for $\theta = 0^0$, while (f) and (g) indicate the retrieved amplitude and phase

information, for $\theta = 136.50^0$. Here amplitude and phase values are normalized between [0,1] and $[-\pi, \pi]$, respectively.

A normalized root-mean-squared (nrms) error [13] [16] in the object domain after 1000 iterations is plotted with respect to the θ; the direction from which the filtered section is cropped as shown in figure 2.3 (a) by the solid line. The nrms error $\mathcal{E}$ is measured, using the following equation,

$$\varepsilon = \sqrt{\frac{\sum_{r \notin S(r_o,\theta)} |g''(r)|^2}{\sum_{r} |g''(r)|^2}}. \tag{2.9}$$

Where $g''(r)$ represents the reconstructed complex-valued object. To calculate this error, ratio of the intensity value of the pixels of the reconstructed field $g''(r)$ that are located outside the object support $S(r_o, \theta)$ to the intensity value of the pixels of the entire reconstructed field is measured. Locations of the pixels of the reconstructed field lie outside the object support are shown in figure 2.3 (c) with black color.

For the letter 'A', since the left and right portions are almost symmetric i.e. $P_1(r_o, -180) \approx P_2(r_o, 0)$, filtering from left or right portion or near the value of θ equals to -180^0, 0^0or 180^0 degree from the object autocorrelation produces the twin-image problem as mentioned in the figures 2.3 (d) and (e) for $\theta = 0^0$. It is well known that in the reconstruction plane, twin-image field spreads more compared to twin-image free solution [16] hence reconstructed twin-image field $g''(r)$ generates more error as depicted in figure 2.3 (a) near the value of to -180^0, 0^0or 180^0. Notice value of OAF is nearly zero at these particular locations. However, error is less (without twin-image problem) when filtering are done from the top and bottom locations, where θ is nearly 90^0 or 90^0. At these particular directions OAF is non-zero i.e. $P_1(r_o, -90) \neq P_2(r_o, 90)$. Since in practical situations, where the object is unknown, one does not have information about $P_1(r_o, \theta - 180), P_2(r_o, \theta)$ or do not have access to OAF. Hence, in order to find the best location one needs to scan through different θ, and check when the reconstruction error becomes minimum, at $\theta = 136.50^0$ in our case. The

corresponding reconstructed amplitude and phase results for $\theta = 136.50^0$ are displayed in the figures 2.3 (f) and (g).

Since at $\theta = 136.50^0$ reconstruction shows the twin-image free output, condition $\sum_{r_i \in P_1(r_o, \theta - 180)} |g(r_i)| > \sum_{r_i \in P_2(r_o, \theta)} |g(-r_i)|$ is satisfied for the particular object at this particular direction. Also, this condition can easily be found out visually from the figure 2.2 (a) for the $\theta = 136.50^0$ direction, i.e. sum of points' intensity located in the portion $P_1(r_o, \theta - 180)$ is more compared to sum of points' intensity located inside the portion $P_2(r_o, \theta)$. Also note that, if one select a portion located at the opposite location with $\theta = -43.50^0$ equivalent to the 3rd term instead of the 2nd term in the equation (2.5), this method produces the conjugated and inverted in the reconstruction since $\sum_{r_i \in P_1(r_o, \theta - 180)} |g(r_i)| > \sum_{r_i \in P_2(r_o, \theta)} |g(-r_i)|$ is met at this location. Moreover, if one consider two small circular portions $P_1(0,0)$ and $P_2(0,0)$ on the object, located at the center and follow the same derivation as mentioned in the principle section, the corresponding generated 2nd and 3rd terms in equation (2.5) will completely overlap each other at the center, thereby resulting in higher probability of developing the twin-image problem at this location. Thus, we should not crop or filter a portion from the centre of the object autocorrelation using $S(0,0)$. One should always select a portion from the side of the autocorrelation using $S(r_o, \theta)$ so that one solution dominates over the other and PRA algorithm converges to unique solution.

2.4 Random verses improved initial guess

Here, the effect of using random and improved initial guesses on the HIO PRA is shown. Simulation is carried out by forming a complex object using the same images as shown in figures 2.2 (a) and (b). For the letter 'A', as shown in figure 2.2 (a), the object has asymmetry with respect to x-axis viz filtering from near the bottom location i.e., $\theta = 136.50^0$, results in amplitude and phase reconstruction as displayed in figures 2.3 (f) and (g). These results are unique and deterministic irrespective of the number of times the algorithm runs. Therefore, the error associated with these results also remains constant even if one runs the algorithm multiple times. On the other hand,

reconstructions using a random initial guesses show the non-deterministic outputs. The algorithm has been executed multiple times, and each time the algorithm initiates with different random guess. Executing the algorithm multiple times, shows the different output each time the algorithm run, at some point, it shows the correct reconstruction as shown in figures 2.4 (a) and (b). Sometimes it shows twin image problem as shown in the figures 2.4 (c) and (d) and some other instances, it shows the inverted and conjugate distribution as shown in figures 2.4 (e) and (f) as amplitude and phase respectively. In conclusion, results obtained using the random guesses are not unique; each time the algorithm runs, it produces different output. Errors in the reconstruction for the object support of 40 pixels, for both the cases, are also plotted as shown in figure 2.4 (g), which clearly shows the algorithm uniqueness in the case of improved guess i.e., error remains constant while non-uniqueness in the case of the random guesses viz error keeps on fluctuating.

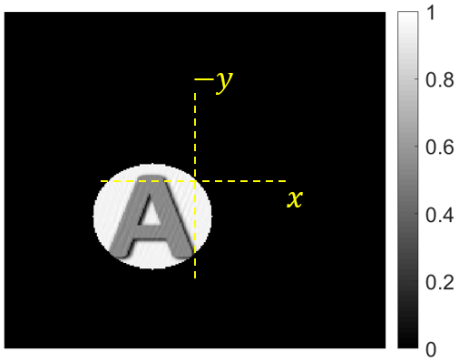

(a)

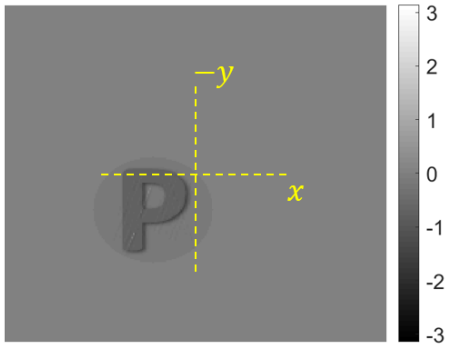

(b)

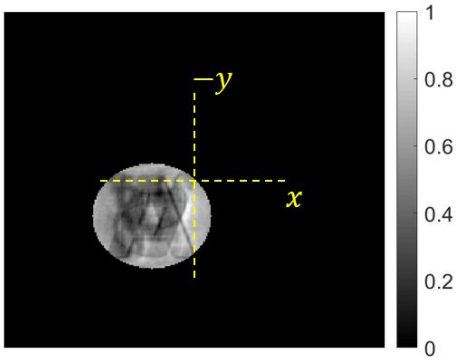

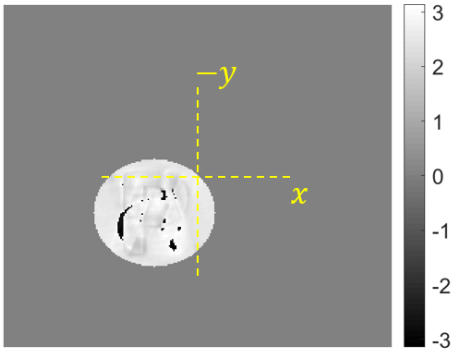

(c) (d)

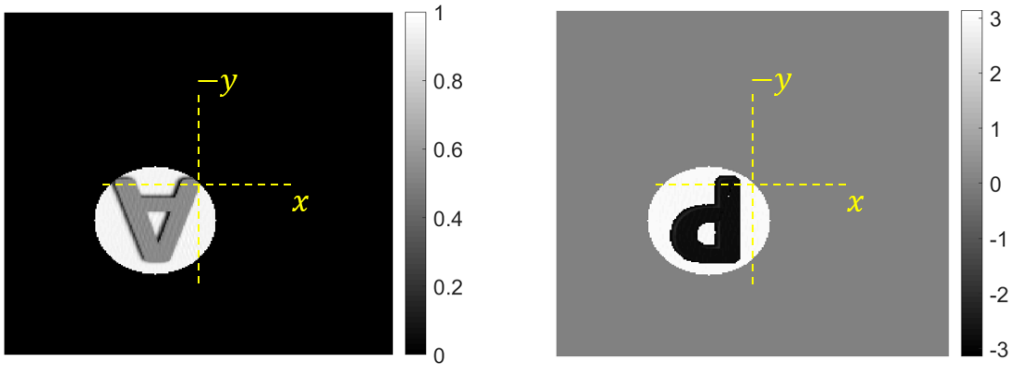

(e) (f)

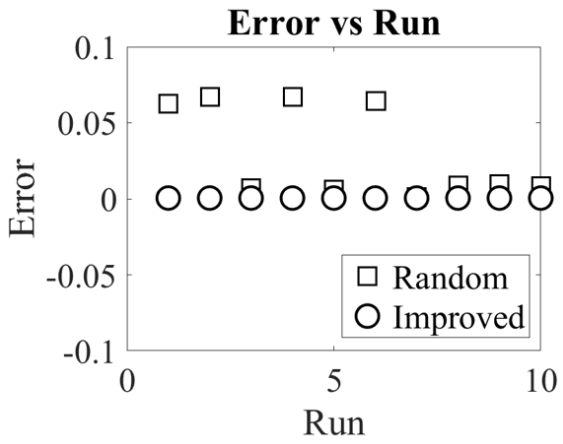

(g)

Figure 2.4: Effect on reconstruction of PRA-HIO algorithm when initialized with different random guesses: (a) correct amplitude and (b) correct phase reconstruction, (c) twin amplitude and (d) twin phase reconstruction, (e) inverted and conjugate amplitude and (f) inverted and conjugate phase reconstruction, (g) Effect on errors when executing the algorithm multiple time.

2.5 Effect of noise

The reconstructed results shown in figure 2.3 and 2.4 are simulated when there is no noise i.e., 0% noise is added. Since in the actual experiment, while detecting the intensity using a camera, unnecessary noises are introduced, in order to match our simulation with the actual experiment,

in this section, we added the noise in the measured data. Here simulations are carried out when noise levels 0.05%, 0.5 %, 5% and 50%, respectively are introduced with respect to the average intensity value present in the measured intensity pattern.

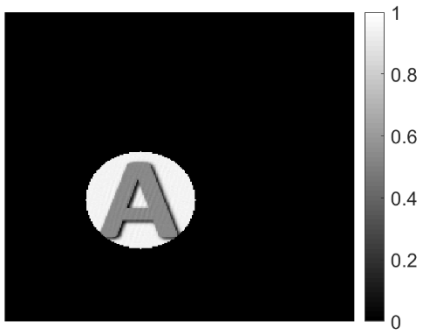

(a)

(b)

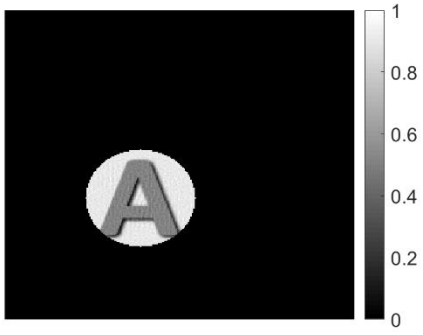

(c)

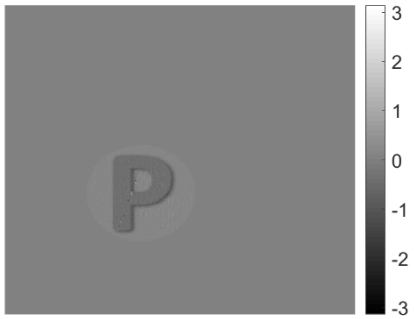

(d)

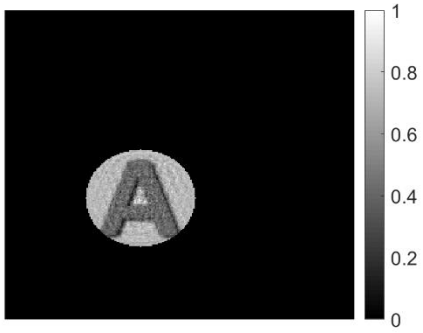

(e)

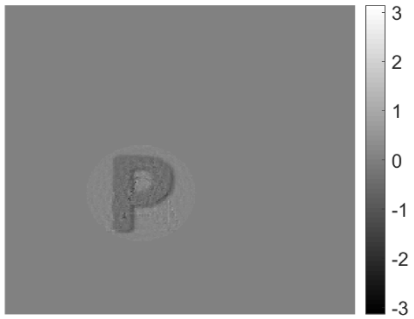

(f)

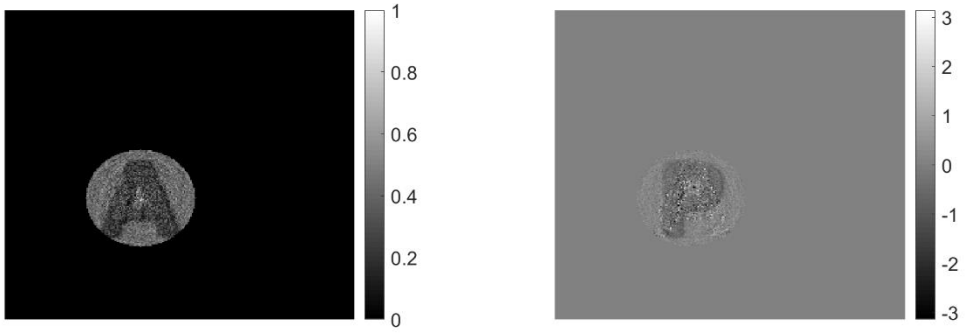

(g) (h)

Figure 2.5: Simulation results when noises are added in the measured data, reconstruction of amplitude and phase (a) and (b) respectively when noise level is 0.05%, (c) and (d) when it is 0.5 %, (e) and (f) noise level is 5% and (g) and (h) 50% noise is added with respect to the average intensity value.

The reconstruction result for the different noise levels using the proposed algorithm is shown in figure 2.5. In the simulations shown in figures 2.2 to 2.5, size of the images used for processing is 256×256 pixels^2. The quality of reconstruction affects severly when 50% noise level is introduced, however, it can be improved to some extent by increasing the size of the recording images along with number of iterations. Improvement on the reconstruction quality with respect to the image size as well with the number of iterations is also tested via simulations.

To further test our technique on a more complicated object, distributions of peppers and boats bounded with a circular support of radius 40 pixels are employed as amplitude and phase information as displayed in figures 2.6 (a) and (b).

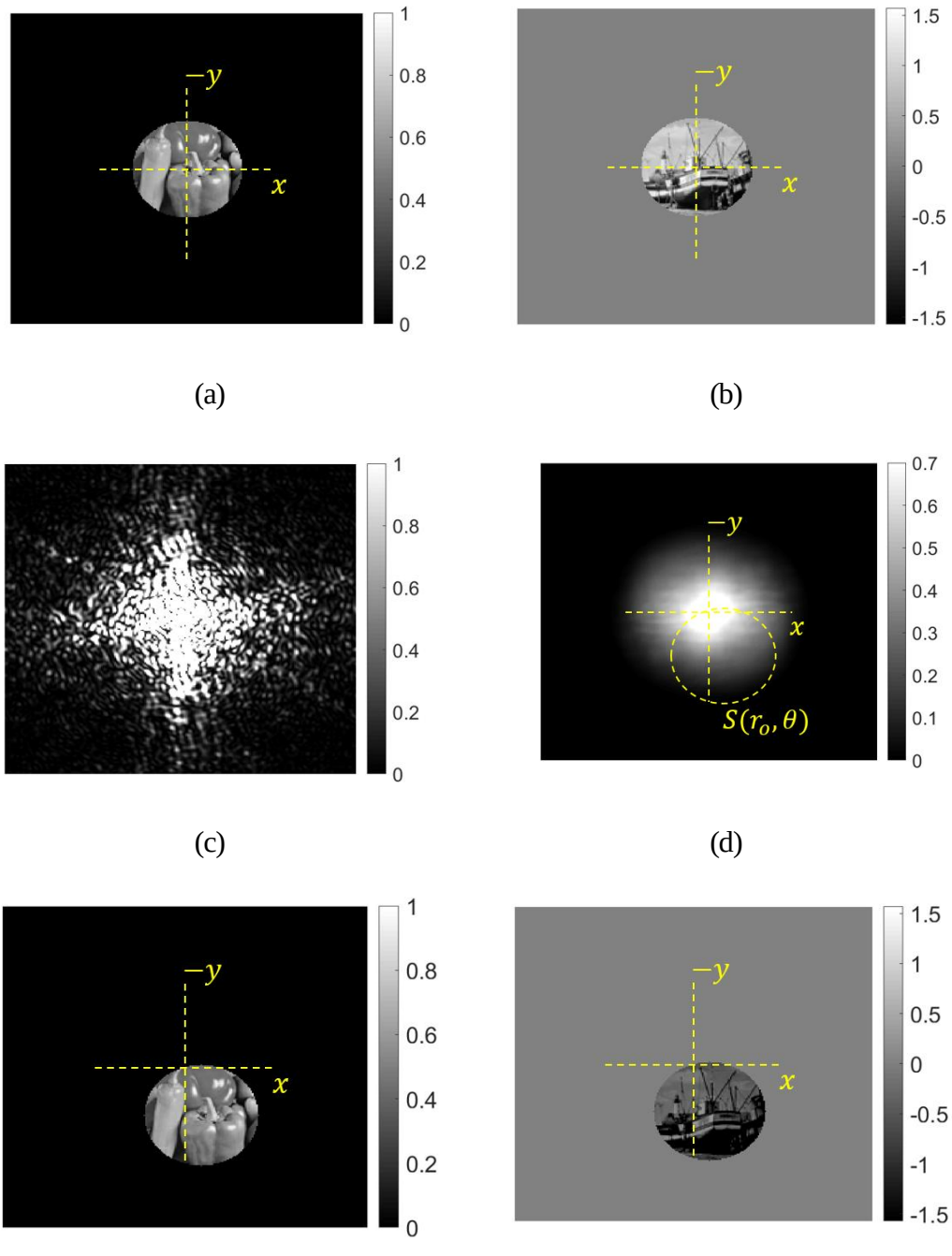

Figure 2.6: Patterns of (a) peppers and (b) boats, representing the complex object amplitude and phase used in the PRA respectively, (c) intensity recorded at the Fourier plane, (d) object autocorrelation, where the dotted circle shows the location

of $S(r_o, \theta)$. Since object autocorrelation is a complex function only its modulus is shown here. (e) and (f) are the retrieved amplitude and phase information, for $\theta = 74.03^0$.

The intensity recorded at the Fourier plane is shown in figure 2.6 (c). And the object autocorrelation obtained from the intensity pattern is shown in figure 2.6 (d). This object is asymmetric in all the directions; therefore, almost every direction produces an output which is free of twin-image. Nonetheless, for this particular object, the minimum reconstruction error and the best retrieved amplitude and phase are obtained for $\theta = 74.03^0$, and displayed in figures 2.6 (e) and (f). In all the figures from figure 2.2 to figure 2.6, the size of images used for processing is 256×256 pixels^2, and number of iterations used for HIO algorithm is 1000, the processing time required to complete the 1000 iterations is around 23 seconds in a system mentioned in the first chapter.

2.6 Experimental results

In the experiment, a coherent laser of wavelength 632.8 nm is used for illuminating a simple object as shown in figure 2.7 (a). The object is created by piercing an opaque black paper with the help of a needle. In the object, seven pinholes are created such that object has symmetry with respect to the y axis and asymmetry with respect to the x axis as displaced in figure 2.7 (a). Moreover, note that the object does not contain any pinhole located at the center. To increase the scattering, this object is followed immediately by a diffuser screen.

Then using a biconvex lens of focal length $f = 15\ cm$ and 8 bit camera (Prosilica GX2750 pixel width $4.54\ \mu m$), the intensity at the Fourier plane is recorded, as shown in figure 2.7 (b).

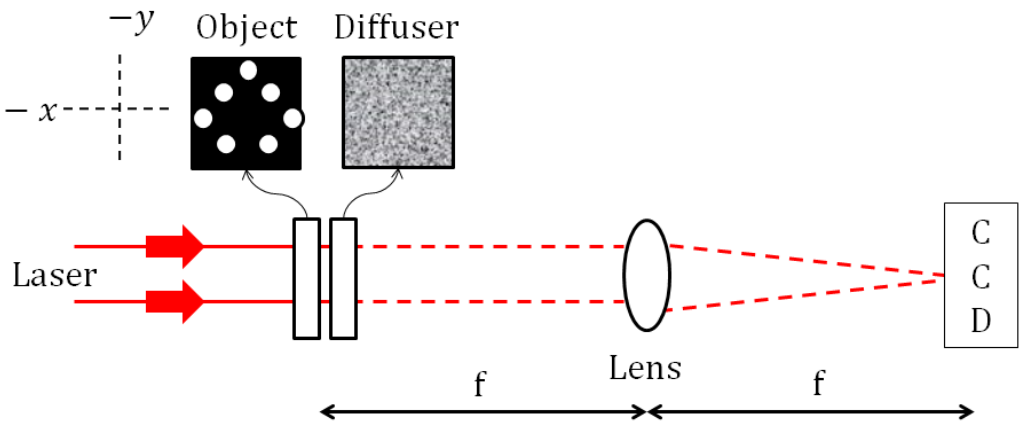

(a)

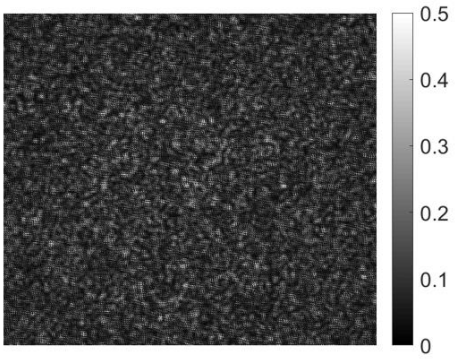

(b)

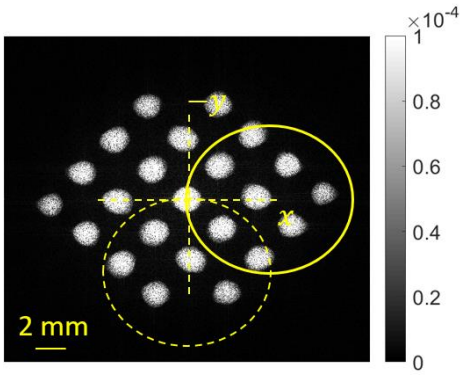

(c)

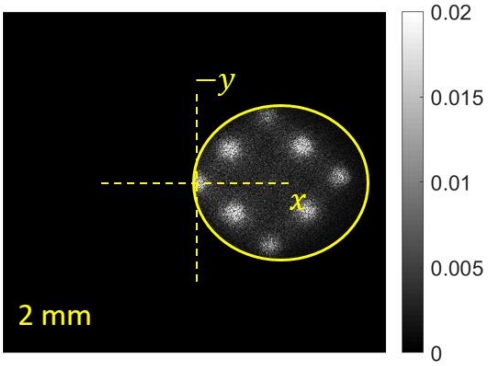

(d)

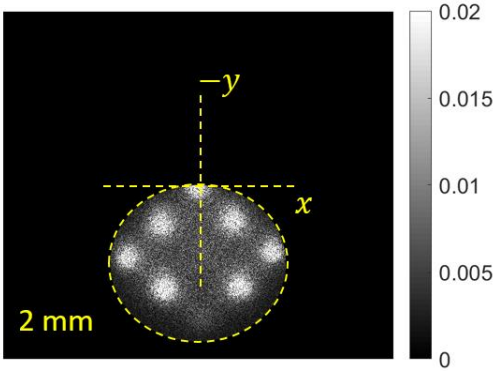

(e)

Figure 2.7: (a) Experimental setup for recording object diffraction pattern at the Fourier plane (b) intensity at the Fourier plane, (c) modulus of the object autocorrelation, solid and dotted circles show the filtering locations for two initial guesses for PRA, located at $\theta =$

0^0 and $\theta = 90^0$ respectively, (d) and (e) are the moduli of reconstructed object corresponding to $\theta = 0^0$ and $\theta = 90^0$ respectively.

Modulus of object autocorrelation is shown in figure 2.7 (c). As can be seen from the object autocorrelation, the portion encircled by dotted line has the features similar to the object, while portion enclosed by solid line has features of object as well the twin. Therefore, it is clear from this example that due to the object asymmetry, object information is encoded into the object autocorrelation along the asymmetric direction. Thus, for the initial guess which is filtered for $\theta = 0^0$, using the solid circle as mentioned in figure 2.7 (c), the twin-image is reconstructed as shown in figure 2.7 (d). While for the portion filtered from for $\theta = 90^0$, using the dotted circle, shows a twin-image free reconstruction in figure 2.7 (e). Notice the portions of object autocorrelation enclosed with the solid and dotted circles displayed in figure 2.7 (c) contain 9 and 8 pinholes. Both the portions have an extra pinhole located at the center; therefore, object is different from the subset of the autocorrelation. In both the reconstruction results pinhole located at the center vanishes, converging to a solution shown in figures 2.7 (d) and (e). Result in (d), clearly shows the reconstruction of the object with twin image, while (e) shows the object reconstruction. Since due to the diffuser, object phase becomes random, only modulus part is shown here. For processing the experimental data, size of an image is kept 2048×2048 pixels^2. Number of iterations used in this case is 1000 and processing time required to complete the iterations for the aforementioned image size is 1114 seconds.

We have also tried experiments using the same setup and experimental conditions as mentioned in section 2.6, for few more objects. The reconstruction results for transparent objects are shown in figures 2.8 (a) to (c) and for reflective object, reconstruction is shown in figure 2.8 (d).

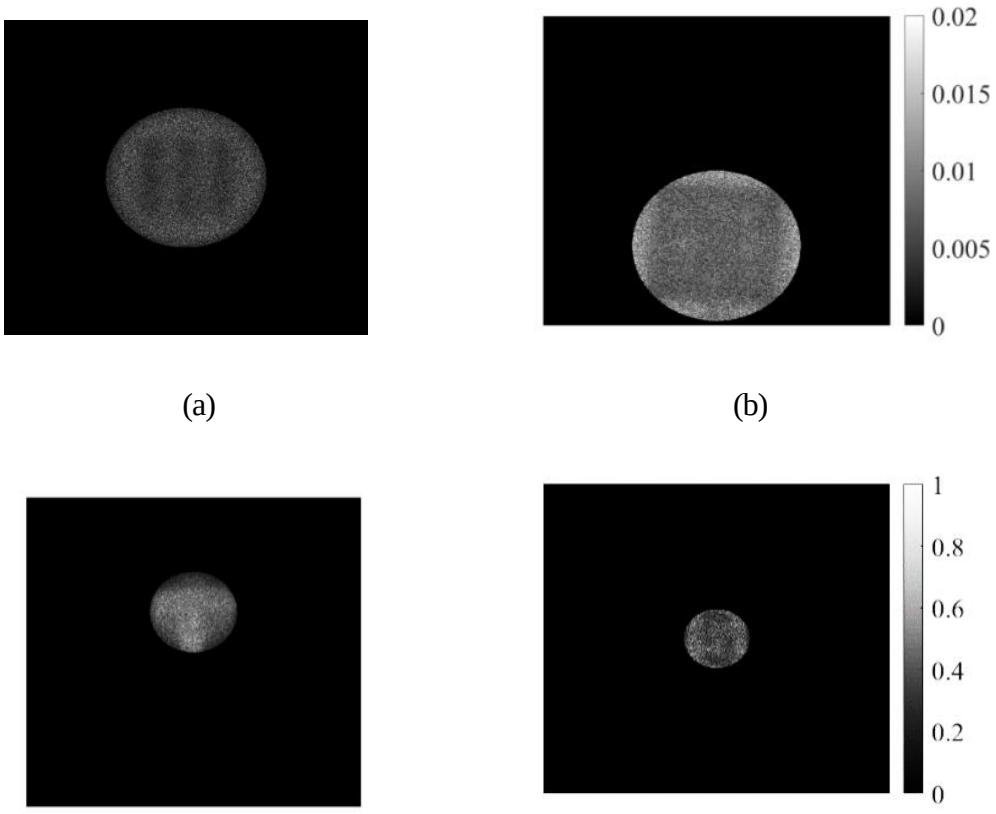

Figure 2.8: Experimental reconstruction results for different objects (a) a portion of USAF chart containing 3 lines followed by a diffuser screen, (b) a square shaped black paper followed by a diffuser screen, (c) a shape of letter 'T' followed by a diffuser screen, (d) and a portion of metal rular containing letter '5'.

2.7 How to improve experimental results

In this section, few key points are discussed to obtain good quality reconstruction from a phase retrieval iterative algorithm (PRA) as mentioned below:

1. Size (r_o) of the object support $S(r_{o,}\theta)$: a rough size of the object support can be measured from the object autocorrelation without recording any additional image. In order to calculate exact support size, error plot should be plotted with respect to the support size. Exact size can be determined by finding the point at which sudden change occurs in the error plot.

2. Number of iterations: by increasing the number of iterations convergence error can be reduced, however, with more number of iterations, algorithm needs longer time to run.

3. Direction of cropping (θ): as we mentioned earlier that we need to find the direction in which object is most asymmetric, only that direction produces less error in the reconstruction. To find that direction since object information is not always present as a priori, we need to plot an error graph with respect to the direction of cropping, and search for a point at which minimum error is obtained.

4. Scattering of a field: for a smooth object or if scattering is low, at the Fourier plane mostly all the scattering lights fall within central region of the camera which can cause saturation issue. Though saturation can be overcome by changing the exposure time of the camera. However, since most of the scattered lights present at the central region of a camera, this small region may not be sufficient to produce good quality reconstruction. Therefore, to increase the scattering a diffuser should be placed in front of the object.

5. Fourier transforming lens: if a thick lens (shorter focal length (f)) is used it can capture higher spatial frequencies; however, it can also introduce aberration. On the other hand, if a thin lens (longer focal length (f)) is used for Fourier transformation, aberration can be reduced at the cost of sacrificing higher spatial frequencies.

6. Camera specification: by utilizing bigger camera (N×M) higher spatial frequencies can be captured which results in higher resolution. Apart from this, camera should have smaller pixel pitch (p) in order to increase field of view.

7. Ambient light and vibration: ambient light and vibration should be as low as possible for better quality, otherwise noise will be present in the reconstruction results. The ambient light can be reduced to some extent by placing an aperture with desired radius before the object.

8. Autocorrelation size: in order to determine the support size, autocorrelation size should not be bigger than the reconstructed image. Besides, its size should not be very small; otherwise, feature of the reconstructed object may not look good. For better

reconstruction, autocorrelation should cover at least 2/3 of the entire image size. Size of the autocorrelation can be changed either by changing the recording distance between the camera and the object, or using different focal length lens.

9. Illumination beam: illumination beam should be as uniform as possible; otherwise, its shape also contributes some noise in the reconstruction. Or else, its effect can be removed from the reconstruction by recording one reference image without the presence of the object.
10. Padding: padding can also be incorporated for improving the quality; however, by utilizing it, algorithm will take longer time to run.

For the reconstruction, hybrid input output PRA is used. An umbrella shaped object shown in figure 2.9 (a) is used for the experiment. An aperture of size (r_o) is placed to reduce the ambient noise and a diffuser screen is placed to increase the scattering as shown in figure 2.9 (a). A lens of focal length $f = 15\ cm$ is used for the Fourier transformation. The intensity as shown in figure 2.9 (b) is recorded at the Fourier plane with the help of a camera. The camera used in the experiment is having size of 2048×2048 pixels^2 and pixel pitch $4.54\ \mu m$. The object autocorrelation obtained from the intensity pattern is shown in figure 2.9 (c). A rough size of the object support is measured from the autocorrelation, which is around $r_o = 270$ pixels. For calculating the exact size of the support, an error plot is plotted with respect to the size of the support as shown in figure 2.9 (d) and a radius is selected where error is reduced significantly i.e., $r_o = 273$ pixels. Once the size of the support is fixed, to find the direction of asymmetry, an error plot is plotted with respect the direction as shown in figure 2.9 (e). The point at which minimum error is achieved can be selected from the figure 2.9 (e), i.e., $\theta = -79^0$. Once these parameters are fixed, number of iterations can be changed according to our need to obtain good reconstruction. To see this effect, amplitudes of object are retrieved after 1000 and 10000 iterations and are displayed in the figures 2.9 (f) and (g) respectively.

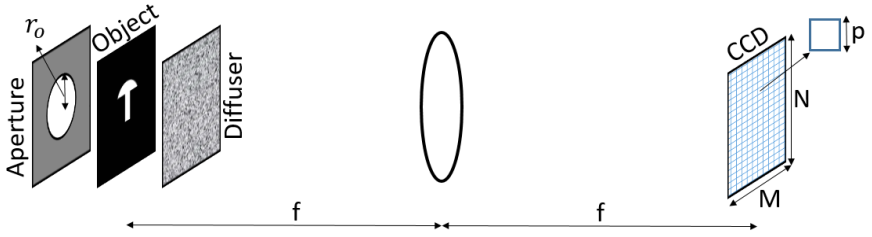
r_o
Object
Aperture
Diffuser
f
f
CCD
p
N
M

(a)

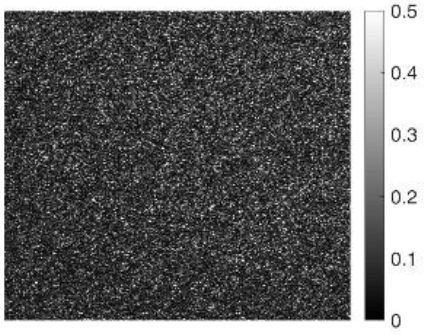
0.5
0.4
0.3
0.2
0.1
0

(b)

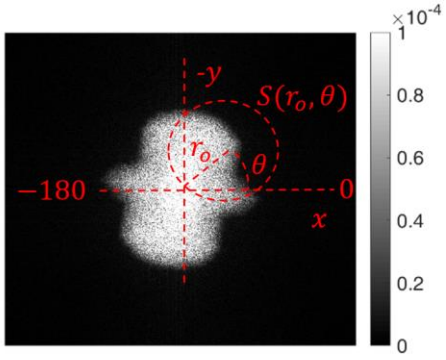
$\times 10^{-4}$
1
0.8
0.6
0.4
0.2
0
-y
$S(r_o, \theta)$
r_o
θ
−180
0
x

(c)

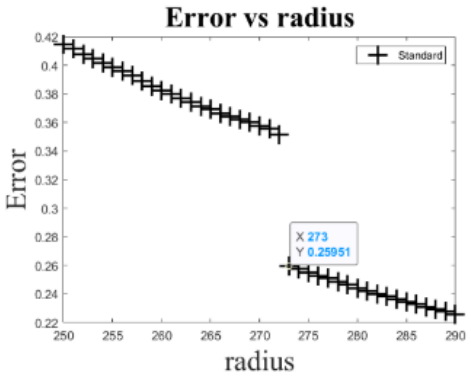
Error vs radius
Standard
Error
radius
X 273
Y 0.25951

(d)

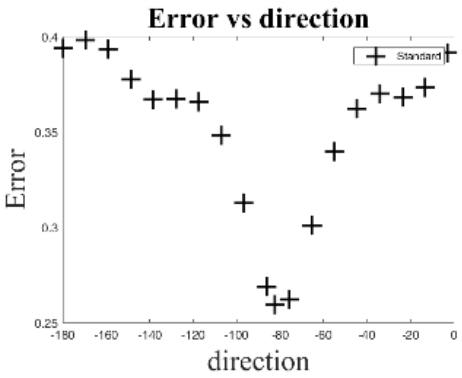
Error vs direction
Standard
Error
direction

(e)

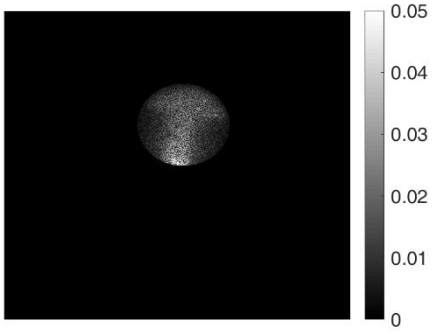
0.05
0.04
0.03
0.02
0.01
0

(f)

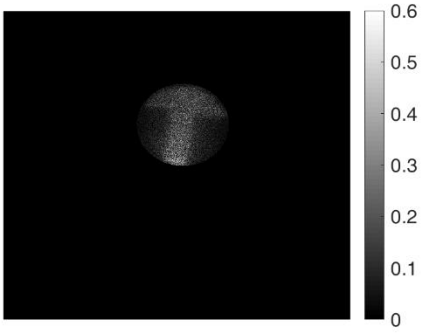
0.6
0.5
0.4
0.3
0.2
0.1
0

(g)

Figure 2.9: (a) Experimental setup for recording object diffraction pattern at the Fourier plane (b) intensity at the Fourier plane, (c) modulus of the object autocorrelation, dotted circle shows the filtering locations, located at θ , (d) and (e) are the error plots plotted after 1000 iterations by changing the size of support and direction of cropping respectively. (f) and (g) moduli of reconstructed object after 1000 and 10000 iteratons respectively at $\theta = -79^{0}$ and $r_o = 273$ pixels.

Therefore, by considering all the mentioned factors, one can achieve good quality reconstruction from the PRA as mentioned in figure 2.9 (g).

2.8 Conclusion

The twin-image problem is severe in case of asymmetric object and in this chapter, asymmetry of the object is used as a tool to eliminate the twin-image problem. By carrying out the simulations as well as the experiment, the validity of the proposed scheme have been proven. The proposed method only requires calculating the object support information. For most of the objects, the support information can be retrieved from the object autocorrelation itself without requiring additional measurements. Even though, results is only demonstrated with Fienup HIO phase retrieval algorithm; this method can be easily incorporated in any other existing PRAs. Additionally, method is not restricted to Fourier plane, it can also be performed in Fresnel region by utilizing corresponding Fresnel propagator. The novel scheme presented in this chapter provides a simple way for retrieving the amplitude and phase information of the object uniquely without any twin artifact in a single-shot and therefore, will be useful in several areas of optics such as biomedical imaging, astronomy, x-ray crystallography, wavefront sensing, electron microscopy.

Chapter 3

Phase retrieval algorithms using edge point referencing

The method discussed in chapter 2, utilizes the asymmetry present in the object to reconstruct the twin-image free solution in the phase retrieval algorithm [22]. Therefore, its application is limited to the objects which have a direction of asymmetry. On top of that, searching the best initial guess from the autocorrelation takes sufficient amount of time, which slow down the process, therefore makes the technique non suitable for real time applications. In this chapter, a novel method is discussed in which an asymmetry is created in the illumination beam itself using edge point referencing (EPR). In this technique a small area near the periphery of the object is illuminated with slightly higher intensity as compared to the rest of the object. Such illumination creates imbalance in the autocorrelation that can be used to improve the initial guess. By utilizing the initial guess, PRA provides twin-image free unique output for asymmetric as well as symmetric objects. In addition, by inducing the asymmetry in the beam, one can also control the strength of the object copy generated in the autocorrelation [20]. By filtering that enhanced copy of the object from the autocorrelation; one can also achieve fast convergence. While, most of the existing PRA techniques based on random initial guess, might produce different outputs in different trails, leads to non-deterministic output. On top of that occasionally output of such algorithm either shows non-convergence or needs longer time to converge or shows twin-image problem. Due to this PRA methods based on random guess are unsuitable for the cases where consecutive reconstructed outputs obtained in different trails need to be compared e.g., deformation measurement [23]. Therefore, for the best of our knowledge no one has used PRA method for deformation measurement till now. In contrast to this, the proposed method in this chapter based on EPR produces unique deterministic output; therefore, suitable for such situations.

3.1 Foundation

The phase retrieval algorithms are based on the computation methods which retrieve the amplitude and phase information of the object from the single intensity or amplitude pattern of the propagated field recorded at the Fourier plane. Since in this case, no separate reference optical field is required, this technique is more robust and also suitable for vibrational environment conditions as compared to holography techniques. However, since the intensity recorded at the Fourier plane is identical for the object as well as for the twin (complex conjugate and inverted) copy of the object, the reconstruction result of the existing PRAs sometimes shows twin-image problem in which the signature of object and twin present at the same time [11]. For the application such as measuring deformation [23], one needs to record two sets of data before and after deformation. From these two sets, one needs to reconstruct the object information consecutively before and after the deformation and needs to compare those two. However, owing to the fact of using different random initial guesses in different trails, outputs of PRA method could vary while running the algorithm sequentially [13]; therefore, one cannot determine the deformation by comparing the outputs obtained in two different trails. Due to these difficulties, existing PRAs method based on random guess are not suitable in such cases where we need to compare the output results with each other.

To solve the twin-image problem and maintain uniqueness in PRA, in this chapter, a method is proposed where a single coherent beam is first split into two; one beam is used to illuminate a region of interest (ROI) of the object while the other beam is used to illuminate a small area of the object near the periphery of the first beam on the object surface at the boundary of the ROI. This approach is termed PRA-EPR, where PRA and EPR stand for phase retrieval iterative algorithm and edge point referencing, respectively. PRA-EPR produces an output that is always unique and free from twin-image problem. Since the method produces a consistent deterministic unique result, one can also apply this technique for measuring deformation. By utilizing an area of the object near the periphery as a reference, this method no longer remains limited to asymmetrical objects but applies equally to symmetrical objects as well. Apart from this, by increasing the intensity of the illumination near the edge, one can control the strength of the object copy generated

in the autocorrelation obtained from the intensity [20], and by filtering this enhanced copy of the object, one can retrieve the object information directly without utilizing PRA, however two conditions should be met 1) one should focus the light tightly onto the object in order to generate a big speckle pattern at the far-field, the size of speckle should be large enough to cover the entire size of the CCD camera, 2) one should modulate the intensity of beam focused near the edge. While in this chapter, we proposed that intensity of 2nd beam should be maintained stable and adjusted with respect to 1st beam such that they should generate a high contrast interference pattern. However, even if we adjust the required intensity ratio between the two beams, we can only obtain a blurred image of the object from the autocorrelation, which is merged with background terms present in the autocorrelation. This blurred image of the object can be used an initial guess in PRA to obtain unique reconstruction free from aforementioned problems. Moreover, the method uses only a single intensity hence suitable for real-time dynamic objects, the experimental setup to implement this technique is also simpler compared to the holographic setup where a separate reference source is required [9] [10].

3.2 Theory

EPR can be obtained by creating asymmetry in the illumination beam or structuring the illumination beam. It can be implemented using an intensity gradient filter, or spatial light modulator, or designing optical setup using optical components as discussed in 1st chapter. Here, for simplicity, EPR is implemented by designing the optical setup.

Consider a scenario, where a complex object is illuminated with an edge point referencing, as illustrated in figure 3.1. The illumination contains two beams generated from a single coherent source: 1st beam is a uniform plane coherent beam of radius x_o, used for illuminating a portion or region of interest (ROI) of the object, and a converging coherent beam is used as a 2nd beam to illuminate a small area of the object located at the extreme periphery or the boundary of the ROI i.e., $r = x_o$.

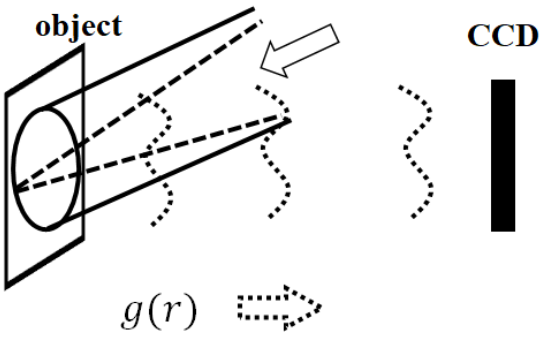

Figure 3.1: Setup for recording object information using EPR scheme.

The scattered field from this object has amplitude as well as phase parts and therefore, can be written as a complex-function represented by $g(r)$. Where r represents a two-dimensional coordinates system. Moreover, owing to the two beams illumination, the scattered field from this object can further be divided into two terms: 1) $o(r)$ which is resulted from the 1st beam and 2) $o(r)c\delta(r-r_o)$, generated from the small area near the edge due to the 2nd beam, where c and $\delta(r-r_o)$ represent the complex amplitude of the 2nd beam and Dirac delta function. Thus the total field can be written as a sum of these two terms as follows

$$g(r) = o(r) + o(r)c\delta(r-r_o) \tag{3.1}$$

The resulting propagated field at the Fourier plane is simply the Fourier transform of $g(r)$, described as follows

$$G(k) = F.T.(g(r)) \tag{3.2}$$

Where $F.T.$ and k represent the 2D Fourier transform operation and 2D spatial coordinates. If a CCD camera is placed at this plane, the recorded intensity is given as follow

$$I = |G(k)|^2 \tag{3.3}$$

The autocorrelation $\breve{g}(r)$ can be obtained by performing inverse Fourier transform operation on the recorded intensity, as

$$\breve{g}(r) = I.F.T.(I) = g(r) \otimes g^*(-r) \tag{3.4}$$

Where the sign $\otimes$ indicates the convolution operation. Rewriting the above equation by using equation (3.1) leads to:

$$\begin{aligned}\breve{g}(r) = o(r) \otimes o^*(-r) + |c|^2 |o(x_o)|^2 \otimes \delta(r) \\ + c^* o^*(x_o)[o(r) \otimes \delta(r + x_o)] \\ + co(x_o)[o^*(-r) \otimes \delta(r - x_o)].\end{aligned} \tag{3.5}$$

Where 1st and 2nd terms show the unmodulated part or DC part, while 3rd and 4th terms represent the object and its twin part. Our goal is to extract the 3rd term from the autocorrelation which contains the object information. Graphically, terms in autocorrelation is illustrated as shown in figure 3.2.

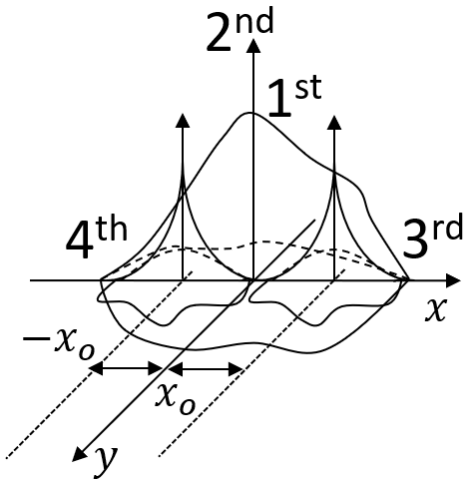

Figure 3.2: object autocorrelation: 1st and 2nd terms show the DC terms, 3rd and 4th terms correspond to the object and its twin as mentioned in equation (3.5).

According to equation (3.5), 3rd term which contains the object information $o(r)$, and depends on the complex amplitude c. According to equation (3.5), by controlling the intensity of 2nd beam, the strength of the 3rd term can be controlled. Cropping this enhanced copy of the object from the autocorrelation and using it as an initial guess in the phase retrieval algorithm retrieves a unique output solution without twin image effect with fast convergence rate. In this chapter, HIO + GS algorithm is opted for the simulation and the flow diagram of the algorithm is given in the Appendix D.

3.3 Simulations

Simulations for phase retrieval iterative algorithm are carried out with and without the edge point referencing.

3.3.1 Simulation result without the edge point referencing

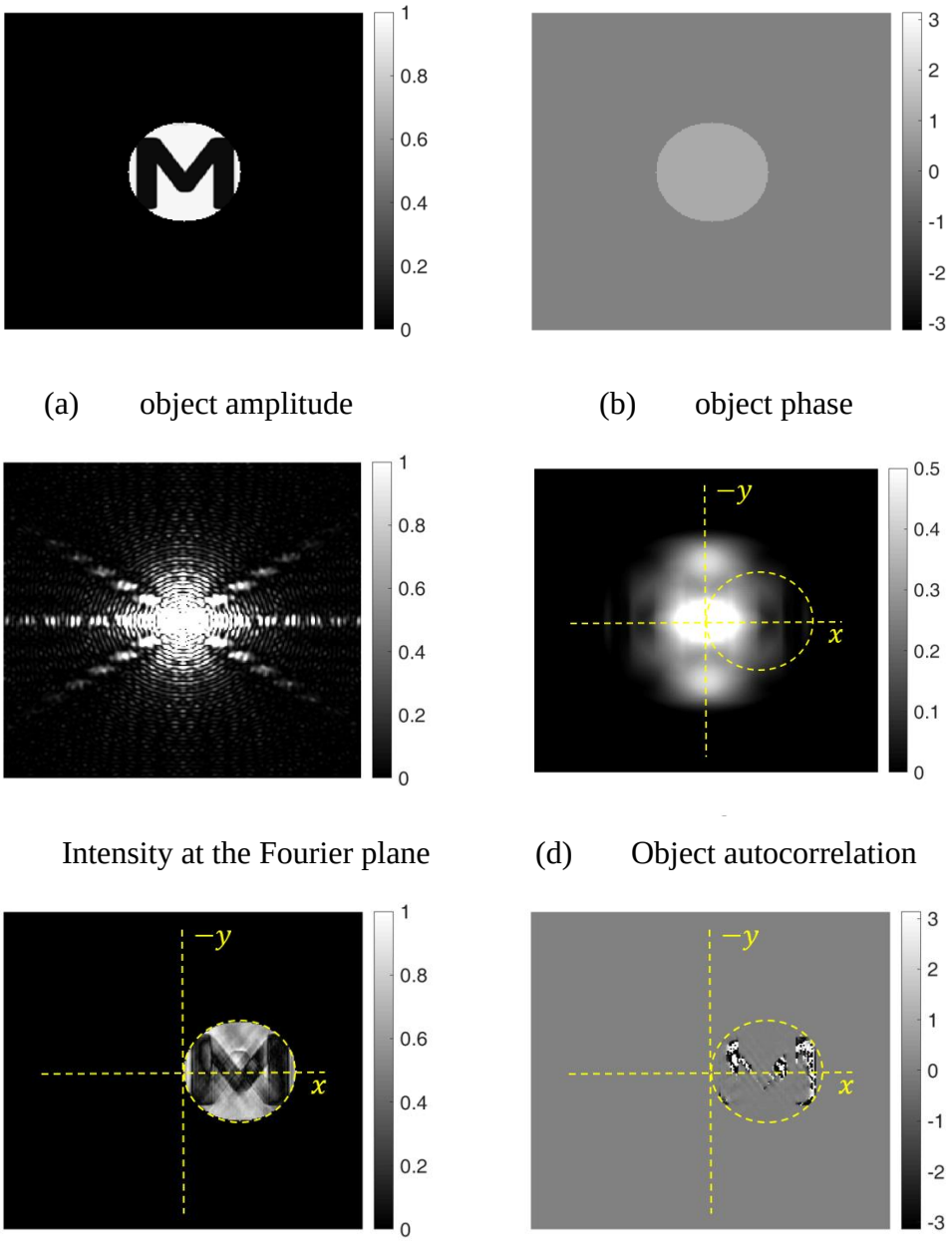

(a) object amplitude (b) object phase

(c) Intensity at the Fourier plane (d) Object autocorrelation

(e) Retrieved object amplitude (f) Retrieved object phase

Figure 3.3: Object reconstruction using PRA without the EPR

For the simulation, an image of letter ‘M’ and an image in which pixels having uniform value inside a circular aperture are used as amplitude and phase of the

complex object, respectively as shown in figures 3.3 (a) and (b). The object is chosen such that it has mirror symmetry along the vertical direction and asymmetry along the horizontal axis. As we have pointed out in the previous chapter that for such kind of object if a portion is cropped from the autocorrelation along the horizontal line passing through the center, it leads to twin image problem. On the other hand, if the portion is cropped from the autocorrelation along the vertical line passing through the center, it results in twin image free solution. For such object, far-field intensity at the Fourier plane is shown in figure 3.3 (c). Autocorrelation of the object is obtained from the far-field intensity and although the autocorrelation is a complex quantity, only its amplitude part is shown in figure 3.3 (d). Due to the object features, object autocorrelation also has symmetry with respect to the vertical axis and asymmetry about the horizontal axis. Thus by cropping a portion from the autocorrelation from the right side as indicated by dotted circle in figure 3.3 (d) and using it as an initial guess in the phase retrieval algorithm retrieves the object with twin image. The reconstructed amplitude and phase results are shown in figures 3.3 (e) and (f), respectively. It can be seen clearly from the figures 3.3 (e) and (f), that the results are obstructed by the twin image artifact.

3.3.2 Simulation result with the edge point referencing

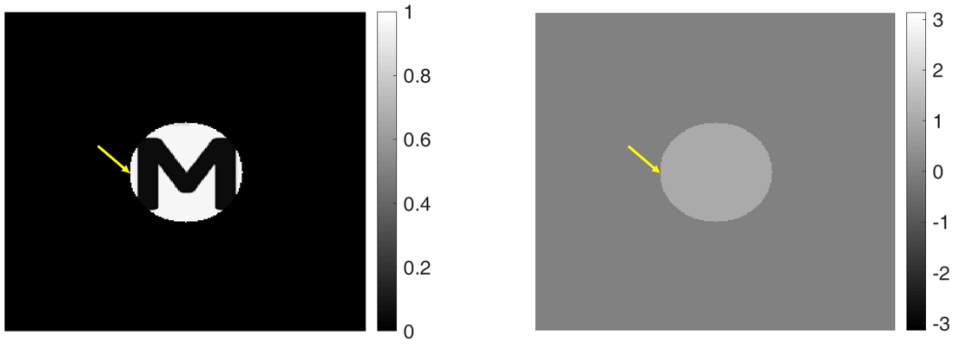

a) Object amplitude b) Object phase

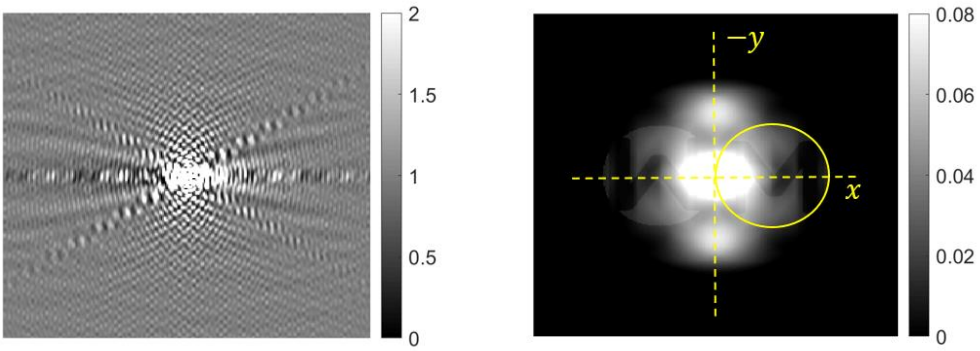

c) Intensity at the Fourier plane d) Object autocorrelation

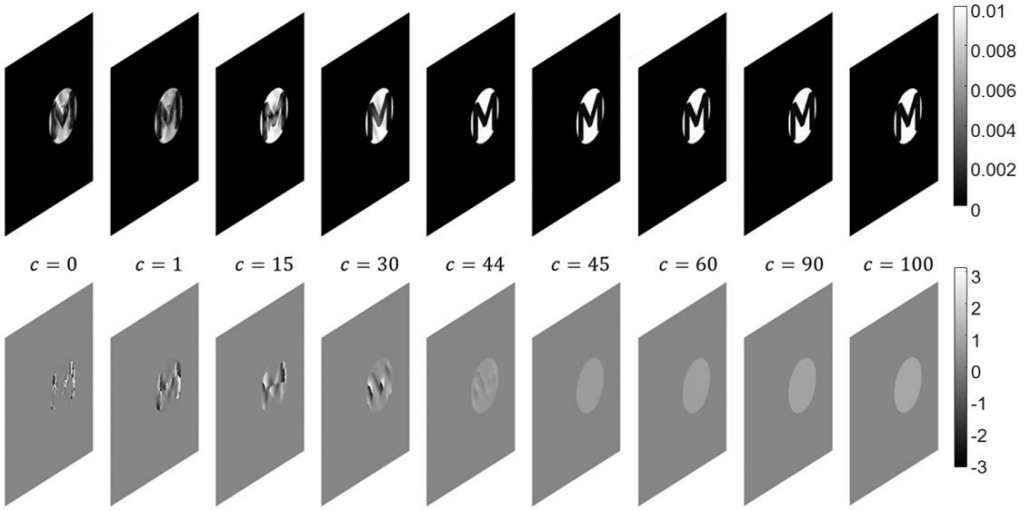

e) 1st and 2nd rows show retrieved amplitudes (normalized) and phases of the object at different values of c

Figure 3.4: Object reconstruction using PRA-EPR, in (a) and (b) arrow-head shows the location of a small area near the edge.

To solve twin image problem and maintaining uniqueness, we perform the simulation with the EPR by changing the amplitude c of 2nd beam from 0 to 100. Location, where 2nd beam needs to be focused, is denoted near the edge of the complex object with arrow-head, as shown in figures 3.4 (a) and (b). Far-field intensity at $c = 100$, is displayed in figure 3.4 (c). Amplitude part of the autocorrelation obtained from the intensity is shown in figure 3.4 (d). It can be seen from this figure that due to the EPR, a copy of the object and its twin generated in the autocorrelation become enhanced. These copies, however, remain merged with the background terms i.e., 1st and 2nd terms as mentioned in equation (3.5), thus, making it infeasible to be retrieved directly. Note also that even though the object

has mirror symmetry about the vertical axis, however, incorporating the EPR, the illumination field can be made asymmetric by controlling the amplitude of the 2nd beam. The amplitude of the 2nd beam should be increased till the value at which the overall field scattered from the object becomes asymmetric irrespective of the symmetry of the object. This field produces an autocorrelation that is also become asymmetric about the vertical axis, with a portion on the right side having more object information compared to its twin part, as shown in figure 3.4 (d). By cropping this portion from the autocorrelation bounded with object support, as indicated by a solid circle in figure 3.4 (d), and using it as an initial guess in the phase retrieval algorithm, the twin image free solution can be obtained. Since information about the symmetry of the object is not always available as a priori, amplitude and phase of the object are reconstructed at different values of c by changing its amplitude from 0 to 100. The respective reconstruction results are shown in figure 3.4 (e), where 1st and 2nd rows show the amplitudes (normalized) and phases obtained at different values of c. From figure 3.4 (e), it can be observed that reconstruction of amplitude and phase becomes similar to the complex object used for the simulation at the value of $c \geq 45$. However, we should note that in EPR scheme, as mentioned in equation (3.1), two fields are scattered due to the illumination of 1st and 2nd beams. Therefore, we must not choose the amplitude of 2nd beam too weak or too strong; otherwise, it would become difficult to sense weaker field over the strong one, and a camera with high dynamic range must be required in that case. In practice, we measure the intensities rather than the amplitudes of the fields scattered from the object. In the recorded intensity, in order to obtain high contrast in the interference pattern generated due to overlapping of the scattered fields, intensity of 2nd beam should be adjusted with respect to the 1st beam. The adjustment in the intensities of the two beams should be kept such that the scattered fields generated from both the beams should contain similar intensities.

Figure 3.5: Convergence rates of the PRA with respect to the number of iterations for two cases at $c = 45$ and at $c = 50$.

In order to show the performance of the proposed algorithm, the convergence rates of the PRA algorithm for two cases: at $c = 45$ and at $c = 50$, are plotted as shown in figure 3.5. The convergence rate is calculated based on a normalized root-mean-squared (nrms) error (the amount by which the output image violates the object-domain constraint) measured in object domain [13]. It is clear from figure 3.5, that by increasing the amplitude c of 2nd beam, convergence rate becomes faster; therefore, number of iterations and computational time can be reduced. Uniqueness of PRA algorithm for random and improved guesses is further analyzed in Appendix B.

3.4 Effect of noise

The reconstructed results shown in figure 3.3 and 3.4 are obtained without the noise. Similar to the investigation carried out in the previous chapter, here simulations are carried out when noise levels 0.05%, 0.5 %, 5% and 50% , respectively are added with respect to the average intensity value present in the measured intensity pattern. During this study value of c is chosen 100.

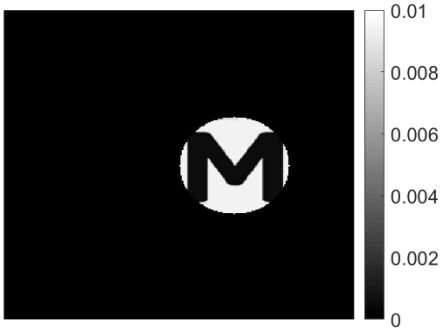
0.01
0.008
0.006
0.004
0.002
0

(a)

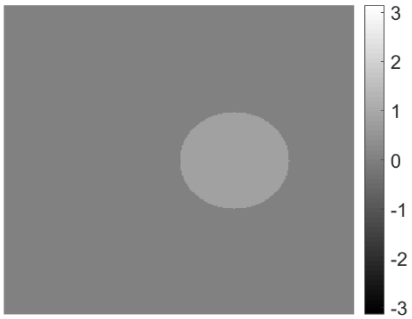
3
2
1
0
-1
-2
-3

(b)


0.01
0.008
0.006
0.004
0.002
0

(c)

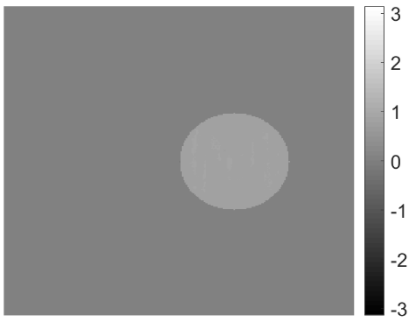
3
2
1
0
-1
-2
-3

(d)

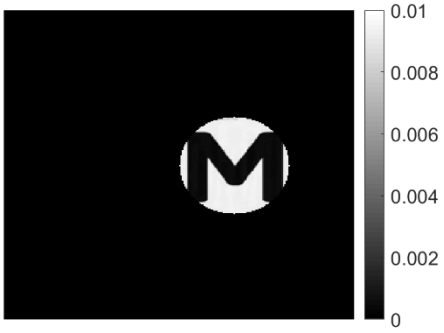
0.01
0.008
0.006
0.004
0.002
0

(e)

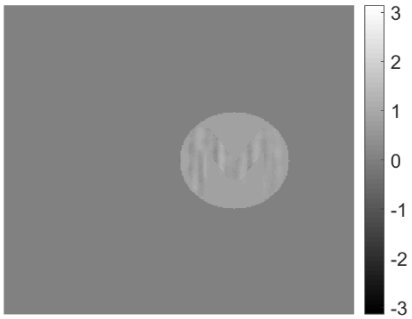
3
2
1
0
-1
-2
-3

(f)

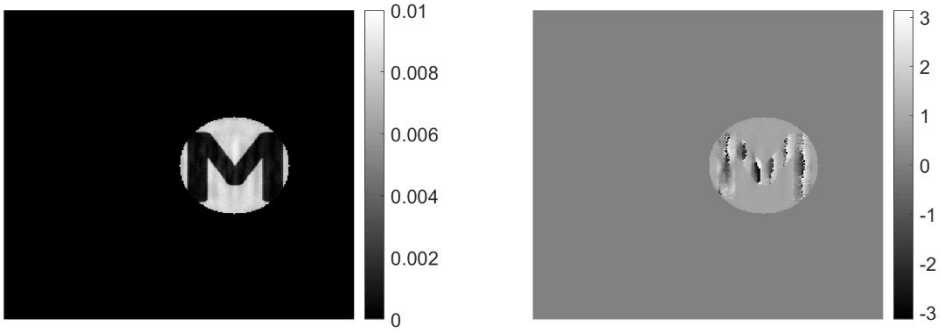

(g) (h)

Figure 3.6: Simulation results when noises are added in the measured data, reconstruction of amplitude and phase (a) and (b) respectively when noise level is 0.05%, (c) and (d) when it is 0.5 %, (e) and (f) noise is 5% and (g) and (h) 50% noise is added with respect to the average intensity value.

Similar to the previous chapter, reconstruction quality is degraded when noise level is 50% as shown in figures 3.6 (g) and (h). It can be improved to some extent as mentioned in the chapter 2 and also by increasing the value of c. For processing, size of intensity pattern is chosen 256 ×256 pixels^2 and number of iterations is selected 25. Processing time required to complete the HIO + GS iterations for the aforementioned image size is 22 seconds in a system as mention in the introduction chapter.

3.5 Experimental setup

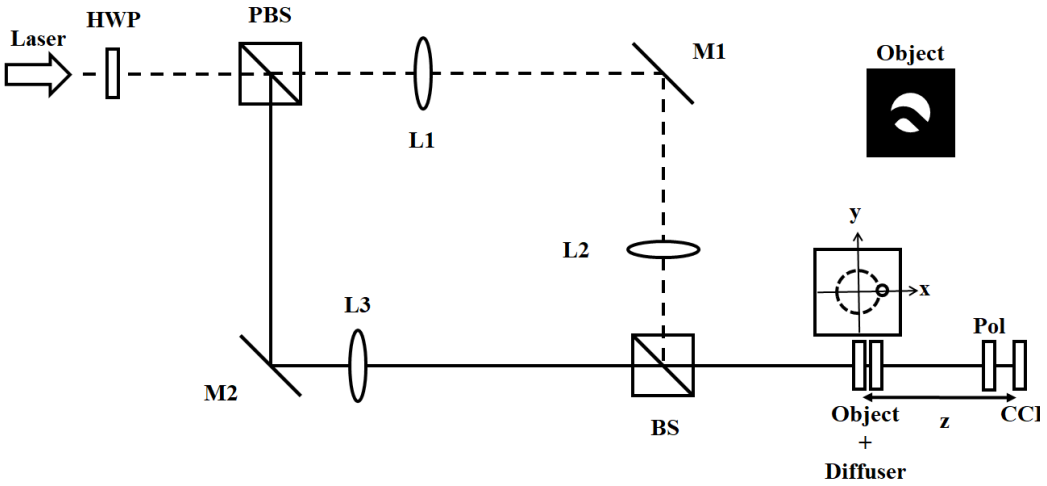

Figure 3.7: Experimental setup, HWP: half wave plate, PBS: Polarizing beam splitter, BS: Beam splitter, M1 and M2: mirrors, L1-L3: Lenses, Pol: polarizer and CCD: charge coupled device or a camera. Intensity of the beams can be controlled via rotating HWP and for generating an interference pattern a Pol is placed and oriented at 45 degree.

Using the Mach-Zehnder interferometer setup shown in figure 3.7, we implement the EPR. In the experimental setup, a uniform coherent polarized plane laser beam is divided using a polarizing beam splitter PBS. The transmitted part of the light denoted by a dotted line in the above figure, is imaged using 4F geometry with the help of two lenses L1 and L2 at a plane where object is placed. On the other hand, the reflected beam (solid line) is Fourier transformed or converged at the object plane using the lens L3. By shifting the mirror M2 and the lens L3; the position of the converged beam can be controlled transversely at the object plane. The diagram provided at the top of the object plane in figure 3.7 shows the beam profile, indicating the asymmetry in the beam profile with respect to the vertical direction. The scattered fields from the object and that arises from the small area near the edge are made to interfere by incorporating a polarizer at the output of the interferometer, and resulting intensity distribution at far field is captured using a camera (CCD). Note, the relative intensities of beams propagating through the arms of Mach-Zehnder interferometer can be controlled by placing a HWP before the PBS.

3.5.1 Experimental results

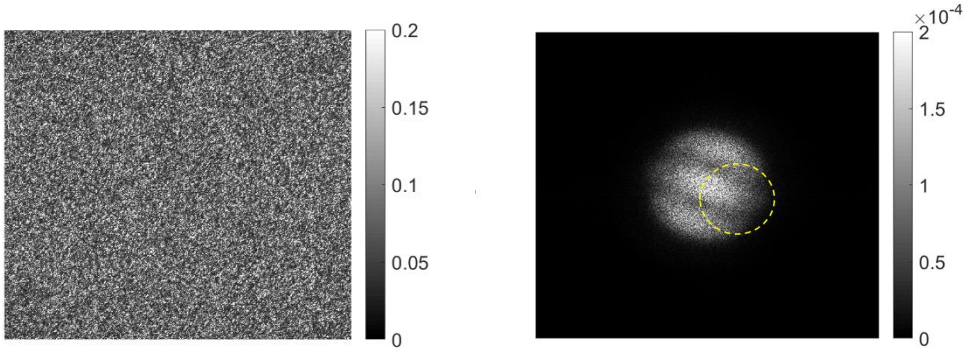

(a) Far-field intensity pattern

(b) Amplitude of the object autocorrelation

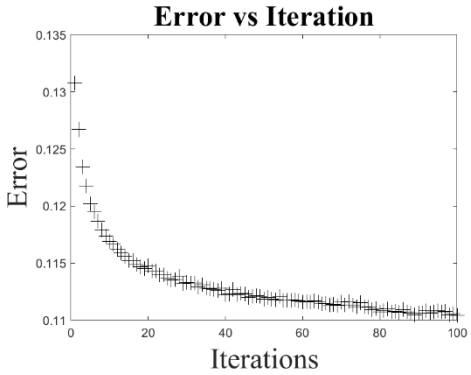

(c) Convergence of the PRA with respect to the number of iteration

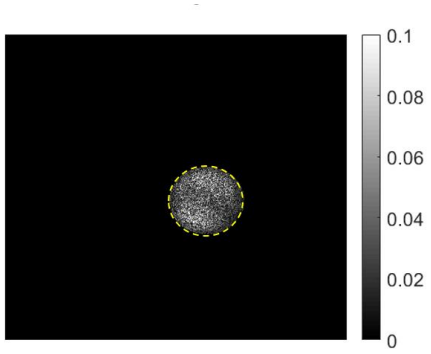

(d) Reconstructed amplitude of the object

Figure 3.8: Experimental result without the edge point referencing

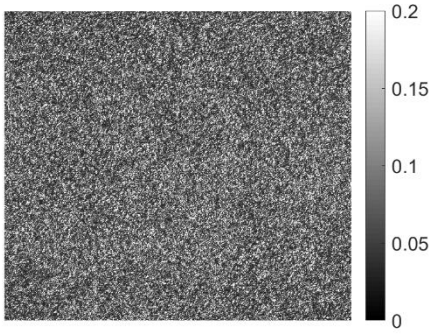

(a) Far-field intensity pattern

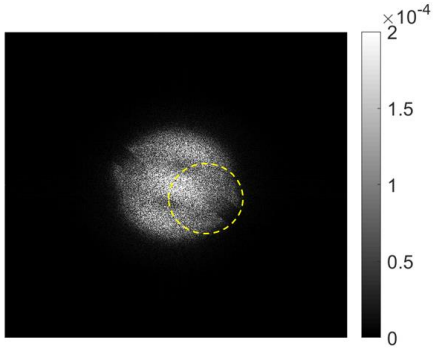

(b) Amplitude of the object autocorrelation

(c) Convergence of the PRA w.r.t number of iteration

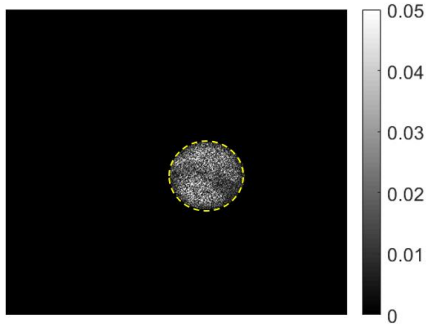

(d) Reconstructed amplitude of the object

Figure 3.9: Experimental result with edge point referencing

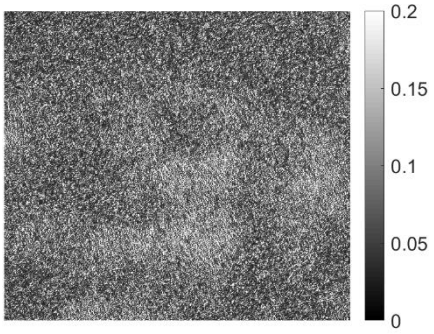

(a) Far-field intensity pattern

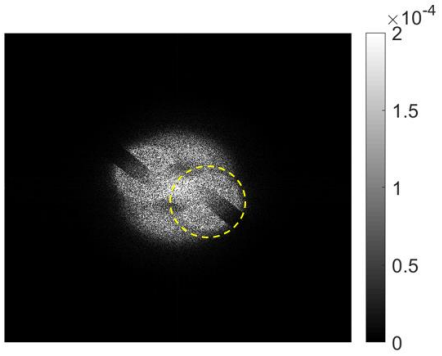

(b) Amplitude of the object autocorrelation

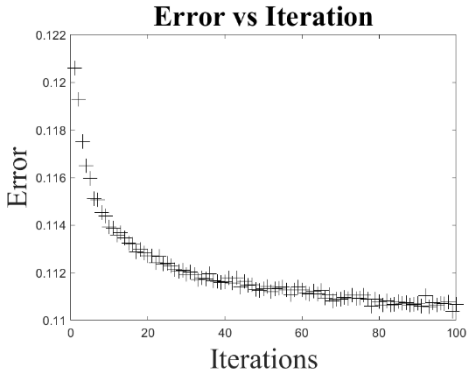

(c) Convergence of the PRA w.r.t number of iteration

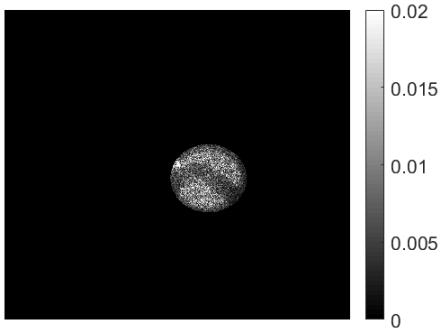

(d) Reconstructed amplitude of the object

Figure 3.10: Experimental result with intense edge point referencing

An object having the shape shown in inset in figure 3.7 is used in the experimental setup. It is a curved metallic wire placed across the path of the beam, immediately followed by a diffuser screen. This object is first illuminated with a bounded uniform plane beam allowing the beam indicated with the dotted line and blocking the beam represented with a solid line in figure 3.7, hence the resulting far-field intensity without edge point referencing is captured as shown in figure 3.8 (a). The object autocorrelation is obtained from the intensity and its amplitude part is displayed in figure 3.8 (b). From the figure, object support is calculated which is half the size of the autocorrelation, and a portion bounded with the object support is then cropped from the autocorrelation as shown by the dotted circle in figure 3.8 (b), for more detail, refer Appendix B. This cropped portion is used in the phase

retrieval iterative algorithm as an initial guess. The convergence rate of the PRA is shown in figure 3.8 (c). The respective reconstructed amplitude of the object is shown in figure 3.8 (d). Due to the presence of the diffuser near the object shown in the inset in figure 3.7, the phase part of the object becomes completely random; therefore, the retrieved phase part of the object does not have any useful information; thus it is not shown here.

In the second case, both the beams are allowed: the bounded uniform plane coherent beam along with the 2^{nd} beam. By following the same procedure and principle, object amplitude is reconstructed as shown in figure 3.9 (d) from the far-field intensity captured with the edge point referencing as shown in figure 3.9 (a).

For the third case as shown in figure 3.10, we are using an intense beam for EPR, when an intense reference source is present near the object periphery, we may not require the phase retrieval algorithm; additionally, object information can be retrieved directly from the autocorrelation as mentioned in figure 3.10 (b). However, the reconstruction is only possible when an additional beam is tightly focused on the object plane and illuminates a single point of the object located at the edge. Whereas if the additional beam illuminates a small area instead of a point, several copies of the object are generated in the autocorrelation which are merged with each other. This causes blurring in the direct reconstruction. While by using the PRA, even the additional beam is not tightly focused, we can obtain the object without any blurring as shown in figure 3.10 (d). On top of that for some objects whose reflectivity or transmitivity is unknown, the portion near the edge of the object could scatter the light very weakly even when the intense beam is used. Besides, to obtain a good interference between the object and reference fields, the intensity ratio between the two beams should be kept almost equal. In such cases, DC terms will be more dominant compared to the cross terms; thus, we will not be able to retrieve the object information directly. Hence we included the PRA along with the edge point referencing so that the proposed technique works irrespective of the blurring, reflectivity or transmitivity of the object and intensity ratio of the illumination beams. For processing, size of the images is kept 2048×2048 pixels^2. Number of iterations used in this case is 100 and processing time required to

complete the HIO + GS iterations for the aforementioned image size is 3318 seconds.

3.6 Simulation result for deformation measurement

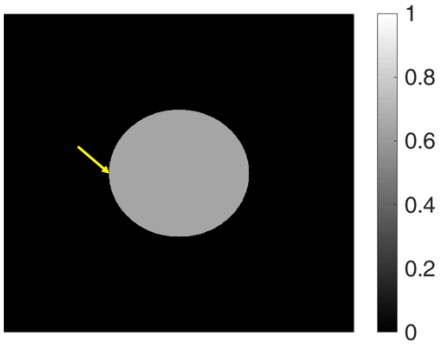

(a) Complex Object: amplitude

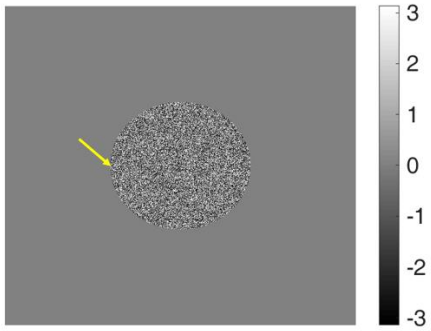

(b) Complex Object: phase

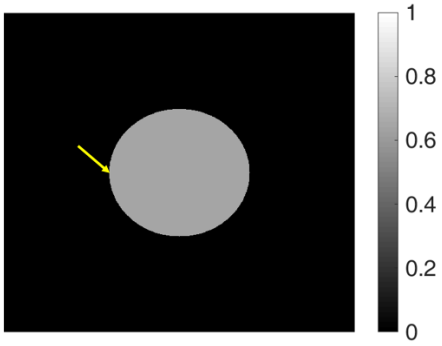

(c) Complex Object: amplitude after the deformation

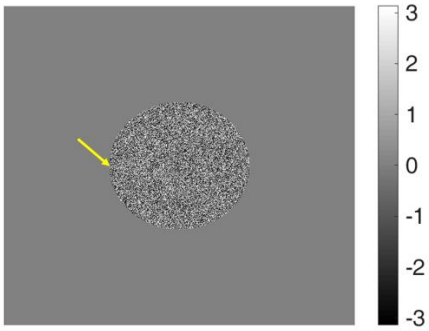

(d) Complex Object: phase after the deformation

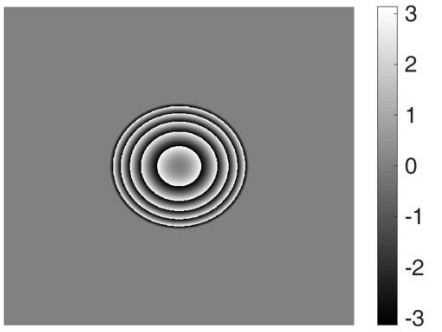

(e) deformation given

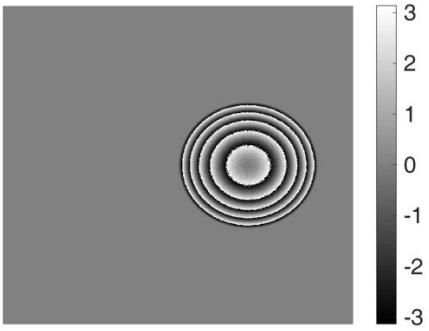

(f) deformation obtained

Figure 3.11: Deformation measurement using PRA-EPR. The arrow head shows the location of a small area near the object's edge.

In figure 3.11 simulation is delineated to measure the deformation using the phase retrieval algorithm with EPR. An object having uniform amplitude and random phase is used for the simulation and it is illuminated with edge point referencing. Object amplitude and phase are shown in figures 3.11 (a) and (b), location near the edge is denoted with arrow head where 2^{nd} beam needs to be focused. A deformation is introduced in the phase part of the object as denoted in figure 3.11 (e). After the deformation, object amplitude remains the same shown in figure 3.11 (c); while phase of the object changes accordingly as shown in figure 3.11 (d). The far-field intensities before and after the deformation at the Fourier plane are recorded. Corresponding autocorrelations are obtained numerically using the two dimensional Fourier transform operation on the recorded intensities. A portion is filtered from the autocorrelation obtained from the intensity pattern captured before the deformation as mentioned in earlier section, from the side of the autocorrelation. Using this portion in the phase retrieval algorithm complex object is reconstructed before the deformation. Similarly, another portion is cropped from the autocorrelation obtained from the intensity pattern recorded after the deformation; respective amplitude and phase of the object are reconstructed. Now to retrieve the deformation information, phases of the reconstructed objects obtained before and after the deformation are compared that shows the deformation information as displayed in figure 3.11 (f) which matches with the deformation introduced in the phase part of the object as shown in figure 3.11 (e). For processing, size of the images is kept 1000×1000 pixels^2. Number of iterations used in this case is 5 and processing time required to complete the HIO + GS iterations for the aforementioned image size is 172 seconds.

3.7 Summary

We have successfully proposed an edge point referencing method to reconstruct the amplitude as well as the phase of the complex object from a single far-field intensity using the phase retrieval algorithm. Our method produces twin image free and unique output with the fast convergence rate and it is applicable for asymmetrical as well as for symmetrical objects. To prove the concept and validate our method we have provided detailed theoretical analysis, simulation, and experimental results, making a strong case for our edge point referencing technique in PRA.

Apart from this, since it provides unique output in lesser number of iterations and irrespective of the number of times algorithm runs, Therefore, our approach can be applied in the cases where we need to compare the output results such as the deformation measurement of an object which is under the loading condition in real time. Since our technique provides consistent and unique results with the fast convergence rate, we think that our straightforward method can be a more effective substitute in all applications where holography technology is currently being used.

Chapter 4

Phase retrieval algorithm in volumetic holographic data storage and reconstruction

To retrieve the complex object information from a far-field intensity recorded at the Fourier plane is a difficult task. Whereas autocorrelation of the object can be obtained easily by performing the two dimensional Fourier transform operation on the recorded intensity. As we have seen so far that the autocorrelation of the object contains many copies of the object and its twin (complex conjugate and inverted of the object) or inverted-conjugate merged with one another and these objects and its twins pairs spread all over the autocorrelation region. Filtering a portion using the object support from the autocorrelation that holds the proportion of the object more compared to its twin self, one should have either an asymmetric object or one should create asymmetry in the beam itself using edge point referencing. This filtered portion then can be used as an initial guess instead of the random guess generally used in the phase retrieval iterative algorithms to achieve the unique solution without twin artifact. Apart from this, one should know the direction of asymmetry either due to the object or due to the illumination beams; as a result, one can crop a portion accordingly from the autocorrelation. Otherwise, it will take sufficient amount of time to search throughout the autocorrelation region using the object support as mentioned in the second chapter. Now the question comes, is it possible to have an imbalance in the autocorrelation for an object without incorporating asymmetry of the object or in the illumination beams? This imbalance in the autocorrelation should be such that the filtered portion from the autocorrelation, irrespective of the direction of cropping, without any knowledge of the direction of the asymmetry of the object and regardless of structuring the illumination beam, it should always hold the proportion of object higher over its inverted-conjugate. Fortunately, it is possible in the case of volumetric holographic data storage and

reconstruction [24], where one wants to reconstruct the amplitude and the phase of the object digitally from the hologram recorded optically.

4.1 Basic Idea

When coherent laser light illuminates an object, the optical field scattered from the object contains the object information. This optical field can be represented as a complex function containing both amplitude and phase parts. In some applications such as holographic data storage and biomedical imaging, the amplitude and the phase parts of the optical field contain valuable information.

To record and reconstruct the amplitude and the phase, several methods have been proposed in the past. Most famous among those methods is holography, where a hologram or interference pattern is recorded, which is created by interfering the optical field scattered from the object with the reference optical field. The recording in the holography can be done either digitally using cameras or optically using photographic plates.

To regenerate the object information digitally from the digital hologram is quite straightforward. One can use computational methods. Similarly, optical reconstruction from the hologram recorded optically in the photographic plate is also quite simple. One needs to illuminate the hologram with a coherent laser light, which reconstructs the field distribution of the recorded object optically. However, digital reconstruction from the hologram recorded optically is a challenging task. Digital reconstruction from the optically recorded hologram has immense potential in volumetric holographic data storage and reconstruction (VHDSR). Volumetric holography data storage and reconstruction technique [25] is mainly used for recording huge data in a small volume. This method has several advantages over the commercially used data storage techniques such as CDs, DVDs, and Blu-ray disc [26] .

Since an object created optically from the hologram has amplitude and phase information, capturing the amplitude and phase information of the object directly using a digital camera is not possible as mentioned in the previous chapters. To the best of our knowledge, most of the existing VHDSR techniques store and reconstruct only the amplitude part using the conventional camera from the

optically recorded hologram [27]. Here a method is proposed to retrieve the amplitude and phase informations digitally from the optically recorded hologram. Therefore, in the same volume, twice the data can be stored and retrieved. In the proposed method, either the hologram should be recorded optically in the Fourier plane or a lensless Fourier geometry [28] should be utilized. In such scenarios, optical reconstruction from the hologram generates object-inverted conjugate pair at the same plane. Object-inverted conjugate pair consists an object and its inverted-conjugate located with some separation. In this case, if one records the intensity of the propagated field at the Fourier plane using the camera for this object-inverted conjugate pair, one can achieve the desired imbalance in the respective autocorrelation obtained from the intensity. In addition, there are several advantages of digital reconstruction over optical reconstruction, several image processing techniques such as resolution and edge enhancement and Fourier filtering etc. can also be incorporated.

In this chapter, our main focus will be on the digital reconstruction of complex object data from the optically recorded Fourier hologram. To reconstruct objects digitally from the Fourier hologram, the Fienup hybrid input-output (HIO) [21] phase retrieval iterative algorithm (PRA) is used, for more detail refer Appedix D. Although the PRA provides complex object reconstruction using simple optical setup; however, the output result from the PRA at times, suffers non-uniqueness and twin image problem. This occurs due to the fact that one uses random initial guesses in the algorithm on different trails. In contrast, the proposed method involves cropping portions from the autocorrelation and utilizes these portions to form an initial guess for the PRA. Incorporating the cropped portions as an initial guess in the PRA, the algorithm provides unique and twin image free reconstruction with fast convergence rate.

4.2 Formulation

Our aim here is to have an imbalance in the autocorrelation for a special object without incorporating the asymmetry of the object or the edge point referencing. This imbalance in the autocorrelation should be such that the autocorrelation should have more information about the object located at one place and information of the

inverted-conjugate of the object at another place. As a result, a portion irrespective of the direction of cropping or its location can be filtered from the autocorrelation which contains more object information compared to inverted-conjugate of the object. Similarly, an another portion can also be selected from the autocorrelation which contains proportion of inverted-conjugate information higher as compared to object. Using these filtered portions as an initial guess in the PRA, one achieves the unique, twin image free complex object reconstruction with a fast convergence rate.

Effect on the object autocorrelations obtained from the far-field intensities recorded at the Fourier plane for different shapes of objects is shown in Appendix C. From the different cases mentioned in Appendix C, an interesting case is selected where the 'special object' has object-inverted conjugate pair separated with d distance away from each other. This object-inverted conjugate pair is located at the same plane as shown in figure 4.1 (a). The scattered field from this object-inverted conjugate pair has amplitude as well as phase part therefore can be written as a complex function and represented as $g(r)$. Where r represents the two dimensional coordinates system. The scattered field from this object-inverted conjugate pair contains two parts: 1) $o(r)$ which is generated due to the object copy and 2) $o^*(-r)$ generated due to the inverted conjugate copy. The total scattered field can be written as follows:

$$g(r) = o(r) + o^*(-r) \tag{4.1}$$

The propagated field at the Fourier plane can be described as follow

$$G(k) = F.T.(g(r)) \tag{4.2}$$

Where $F.T.$ represents the 2D Fourier transform operation. If a CCD camera is placed at this plane, the recorded intensity can be written as follows

$$I = |G(k)|^2 \tag{4.3}$$

The autocorrelation A_c can be obtained by performing inverse Fourier transform operation on the recorded intensity, as

$$A_c = I.F.T.(I) = g(r) \otimes g^*(-r) \tag{4.4}$$

Rewriting the above equation using equation (4.1) leads to:

$$A_c = o(r)\otimes o^*(-r) + o^*(-r)\otimes o(r) + o(r)\otimes o(r) + o^*(-r)\otimes o^*(-r) \quad (4.5)$$

1st 2nd 3rd 4th

Where 1st term and 2nd terms show the unmodulated part or DC part, while 3rd and 4th terms represent the convolution of the object with itself and convolution of the inverted-conjugate of the object with itself. Graphically, terms in autocorrelation for this object-inverted conjugate pair are shown in figure 4.1 (b).

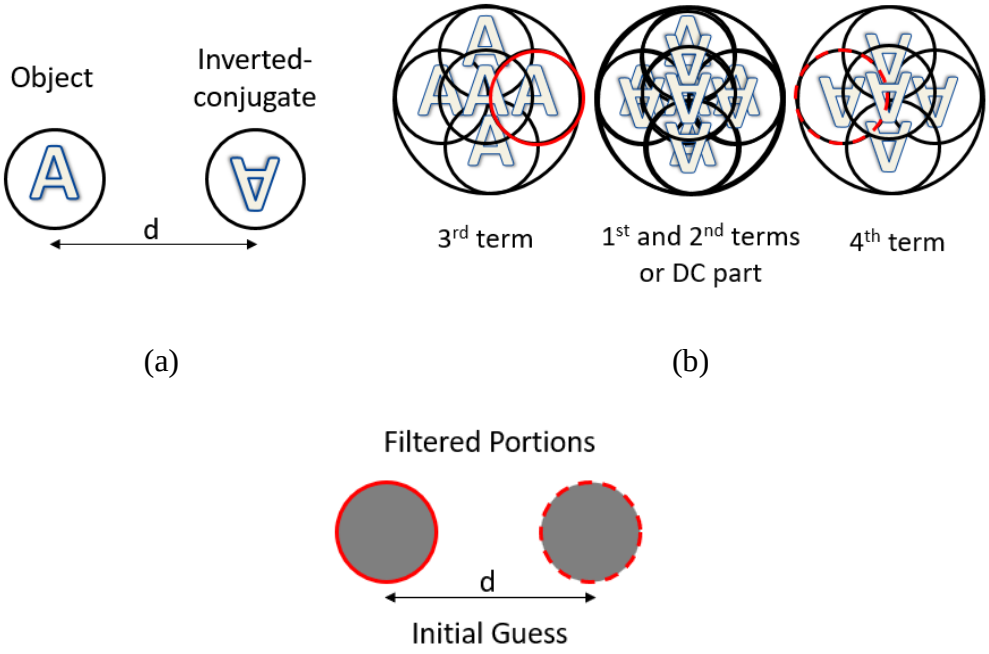

Figure 4.1: (a) Object-inverted conjugate pair, (b) Autocorrelation and 1st and 2nd terms show the DC part and 3rd and 4th terms represent the object convolution with itself or the object copies, and inverted-conjugate convolution with itself or the inverted-conjugate copies, solid and dotted circle show the object and inverted conjugate support, respectively, (c) Formation of initial guess by filtering portions from the autocorrelation using solid and dotted circles and placing them at a distance d from each other.

According to equation (4.5), autocorrelation contains three terms, 3rd term has multiple copies of the object, 1st and 2nd terms create an unmodulated or DC part and 4th term has multiple copies of the inverted-conjugate of the object. 3rd term, 1st

and 2nd terms, and the 4th term are shown in the figure 4.1 (b) located at left, center, and right sides respectively.

In figure 4.1 (b), object copies or the 3rd term mentioned in equation (4.5) appear only on the left side and inverted-conjugate copies or the 4th term mentioned in the aforementioned equation appear only on the right side. Therefore, if one filters a portion from the left side using the object support as mentioned with the solid circle in figure 4.1 (b) and irrespective of its location within the left side, it always contains the object information. Similarly, if another portion is cropped from the right side using the inverted-conjugate object support as shown with the dotted circle in figure 4.1 (b) and regardless of its location within the right side, it possesses the information about the inverted-conjugate of the object. Besides, since object-inverted conjugate pair or the 'special object' has a copy of the object and inverted-conjugate of the object separated with distanced d from each other, to match the filtered portions with the object-inverted conjugate pair, one has to place them d distance away from each other to form the initial estimation for this special object. Note, in order to form the initial guess, the separation between the filtered portions should match with the separation between the object-inverted conjugate pair as shown in figure 4.1 (c). This initial guess is used in the HIO - PRA (Appendix D) with the object-inverted conjugate support along with the amplitude of the far-field intensity pattern as an object and Fourier domain constraints for the reconstruction.

4.3 The procedure of recording and reconstruction

As discussed above the desired imbalance in the autocorrelation can be obtained for a case where one has object-inverted conjugate pair as a special object. This kind of situation arises in the case of volumetric holographic data storage and reconstruction where one wants to record and reconstruct the complex object digitally from the optically recorded Fourier hologram.

Our procedure has mainly three parts: optical recording, optical to digital conversion, and digital reconstruction. In the first part, to record the Fourier hologram, a complex object is illuminated with coherent light and the scattered field from the object is Fourier transformed using a lens, and at the Fourier plane the scattered field is interfered with a plane reference coherent beam. This interference

pattern is captured optically using the photographic film as shown in figure 4.2 (a). The lensless optical setup can also be used for the recording of the Fourier hologram as displayed in figure 4.2 (b) instead of the setup shown in figure 4.2 (a).

In the second part of the procedure, the Fourier hologram is illuminated with the coherent light and the scattered light from the hologram produces three fields at the reconstruction plane. These three parts of the complex field contain an object, DC part, and the inverted-conjugate separated with some distance away from each other as shown in figure 4.2 (c). By placing support at the reconstruction plane, the DC part located at the center is blocked and the remaining parts of the complex field containing only the object-inverted conjugate pair are allowed to propagate and Fourier transformed using a lens. The intensity of the Fourier transformed field is captured using the camera.

In the third part of the procedure, from the recorded far-field intensity, the respective complex autocorrelation is obtained by performing the numerical two dimensional Fourier transform operation. For the reconstruction, one should filter two portions from the autocorrelation. To form the initial guess, one has to place these filtered portions in such a way that the separation between those matches with the same separation as present in the special object. This initial guess is used in the HIO-PRA. The output of the PRA retrieves the twin-image free solution with fast convergence and with deterministic output in a single-shot. The flow diagram of the reconstruction from the recorded intensity is shown in figure 4.2 (d).

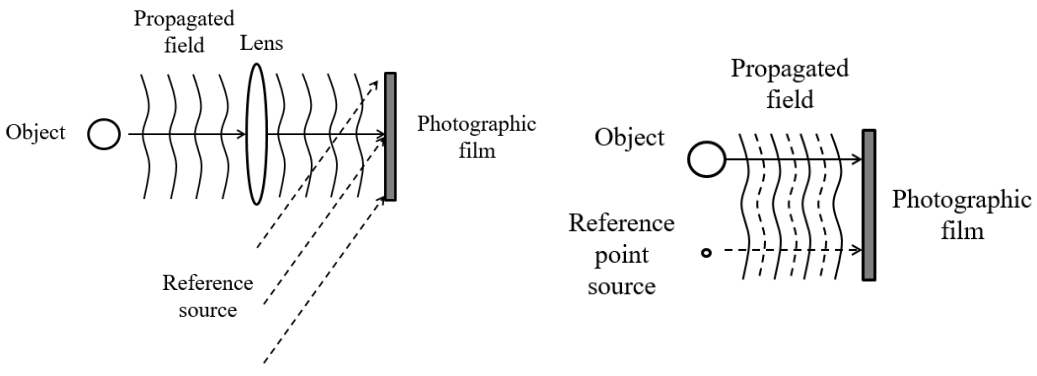

(a) (b)

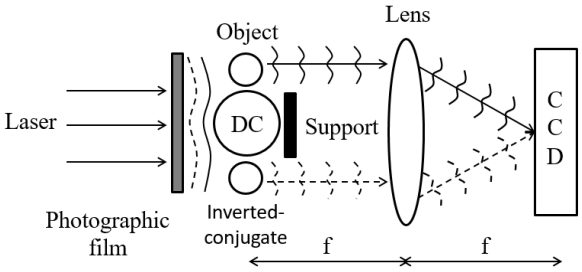

(c)

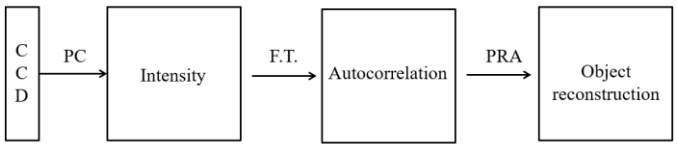

(d)

Figure 4.2: (a) Complex object data recording optically at the Fourier plane, (b) complex object data recording optically using lensless Fourier geometry, (c) optical to digital data recording and (d) complex object reconstruction digitally using PRA.

4.4 Simulation result

For the simulation, amplitude and phase information of the two dimensional complex object is shown in figures 4.3 (a) and (b). Our aim is to store this complex object optically in the Fourier hologram and then reconstruct it digitally. The Fourier hologram recorded optically for this complex object using the aforementioned procedure is shown in figure 4.3 (c). Amplitude and phase of object-inverted conjugate pair along with the DC terms reconstructed optically at the reconstruction plane, from the recorded Fourier hologram are shown in figures 4.3 (d) and (e). Object-inverted conjugate support as shown in figure 4.3 (f) is placed to block the DC part at the reconstruction plane.

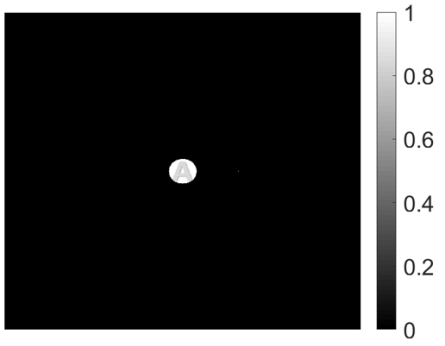

(a) Object: amplitude

(b) Object: phase

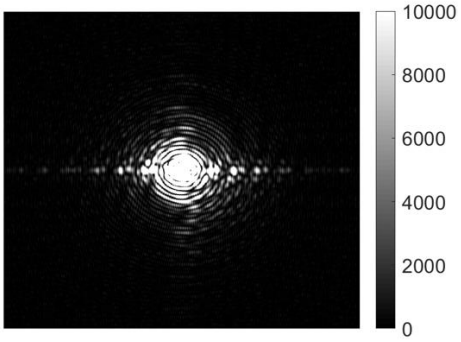

(c) Fourier Hologram

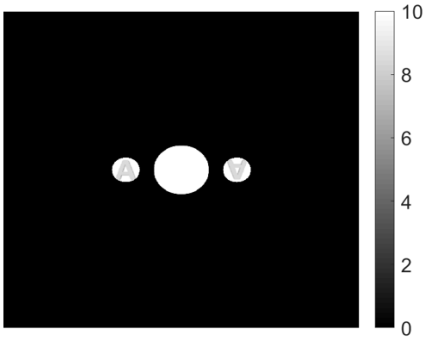

(d) Amplitude of the optical reconstruction

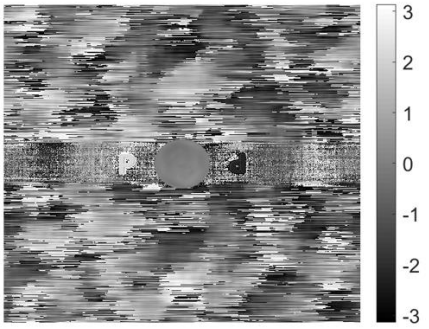

(e) Phase of the optical reconstruction

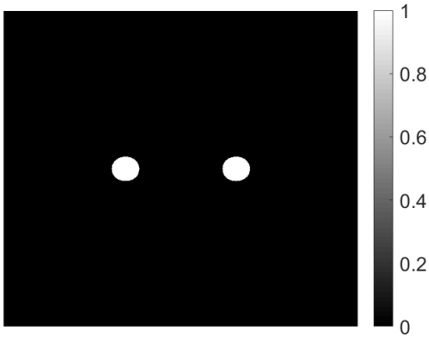

(f) Object-inverted conjugate support

Figure 4.3: Optical recording and optical reconstruction from the Fourier hologram

After placing the object-inverted conjugate support, the remaining parts of the field form the special object and its amplitude and phase parts which contain the object-inverted conjugate pair are shown in figures 4.4 (a) and (b). Intensity of the

propagated field at the Fourier plane for this object-inverted conjugate pair is shown in figure 4.4 (c). Amplitude and phase of the numerically generated autocorrelation from the intensity are shown in figures 4.4 (d) and (e). Locations of the portions for filtering from the obtained autocorrelation are highlighted in figures 4.4 (d) and (e) with a solid and dotted circle, respectively. To form the initial guess, the distance between these two filtered portions is matched with the separation between the object and its inverted conjugate as given in the object-inverted conjugate support. The amplitude and phase parts of the initial guess are displayed in figures 4.4 (f) and 4 (g), respectively. This initial estimation created from the filtered portions is used in the phase retrieval algorithm along with the object-inverted conjugate support and amplitude of the far-field intensity as the object and Fourier domain constrains. The converging error of the PRA has been plotted in figures 4.4 (h) with respect to the number of iterations. Amplitude and phase of the reconstruction results just after the 100 iterations are shown in figures 4.4 (i) and (j) respectively. Figures 4.4 (i) and (j) show the reconstruction of the special object digitally from the optical recorded holographic data. For processing, size of the images is considered to be 1024×1024 pixels^2. Number of iterations used in this case is 100, processing time required to complete the HIO iterations for the aforementioned image size is 35 seconds and noise level is 0%.

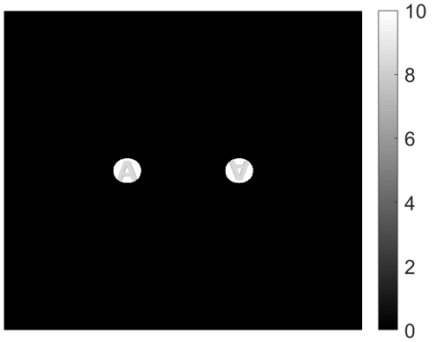

(a) Object-inverted conjugate pair: amplitude

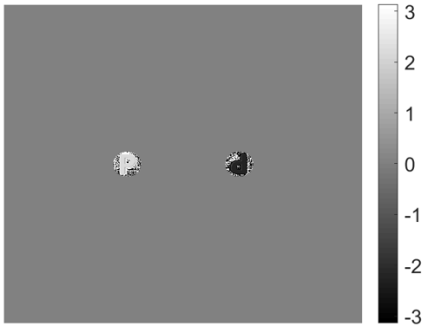

(b) Object-inverted conjugate pair: phase

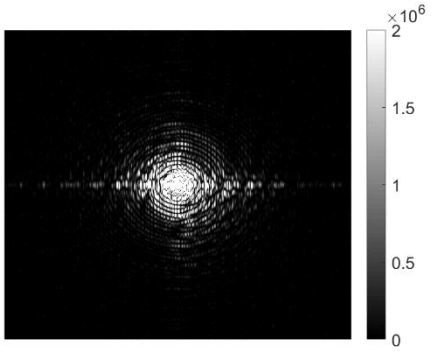

(c) Intensity at the Fourier plane

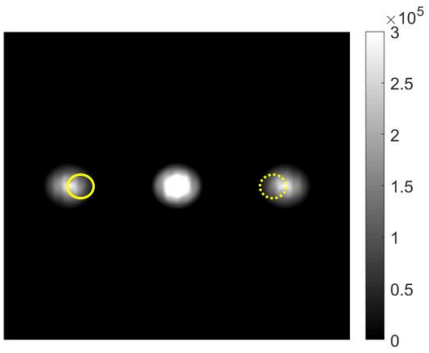

(d) Amplitude of the autocorrelation

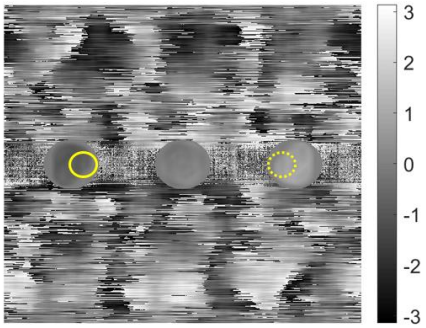

(e) Phase of the autocorrelation

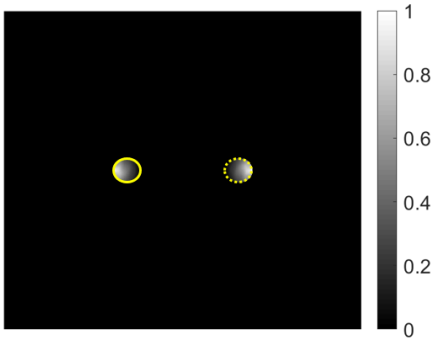

(f) Initial guess: amplitude

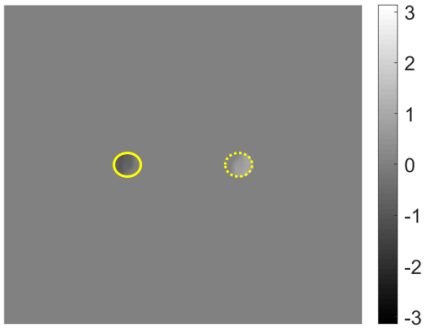

(g) Initial guess: phase

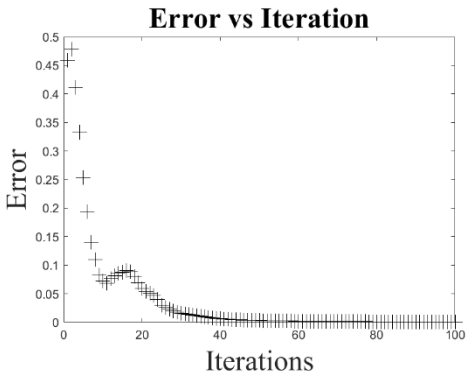

(h) Convergence error with respect to the iteration

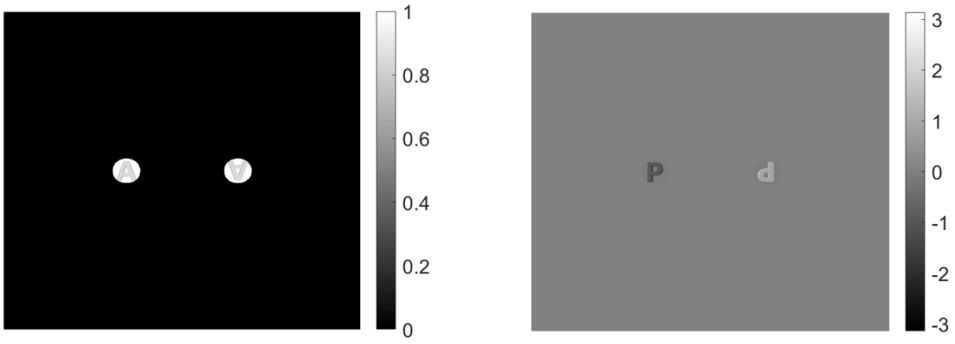

(i) Retrieved object: amplitude (j) Retrieved object: phase

Figure 4.4: Digital recording and digital reconstruction from the Fourier hologram.

4.5 Simulation results when noise is present

The proposed method is a two step process, in the first step optical hologram should be recorded and in the next; intensity scattered from the hologram should be recorded at the far-field. Since in actual experiment noise can be added while recording the hologram as well as when recording the intensity, to mimic the simulation with the experimental condition, simulations are carried out when noise levels 0.05%, 0.5 %, 5% and 50% respectively are introduced in both the steps with respect to the average intensity value present in the measured intensity. As can be seen from the figure 4.5, that reconstruction is possible till noise level of 5 % for the given image size.

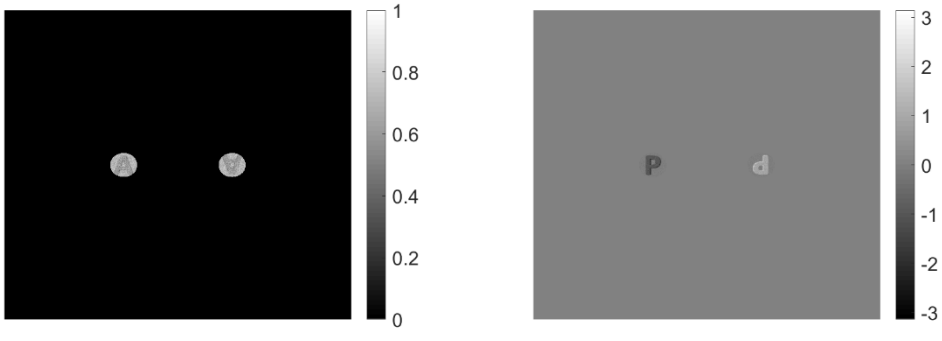

(a) (b)

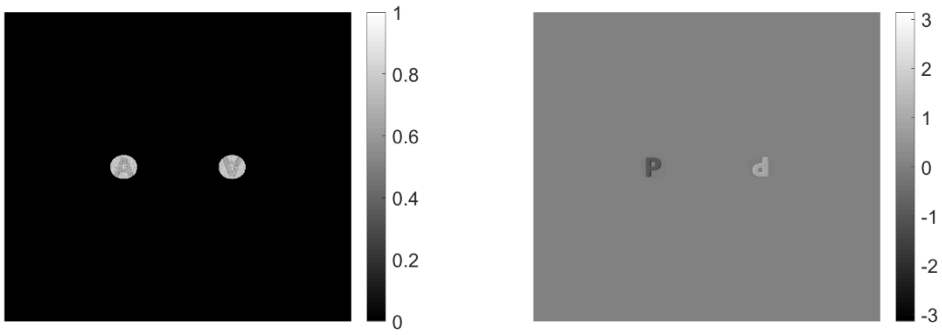

(c) (d)

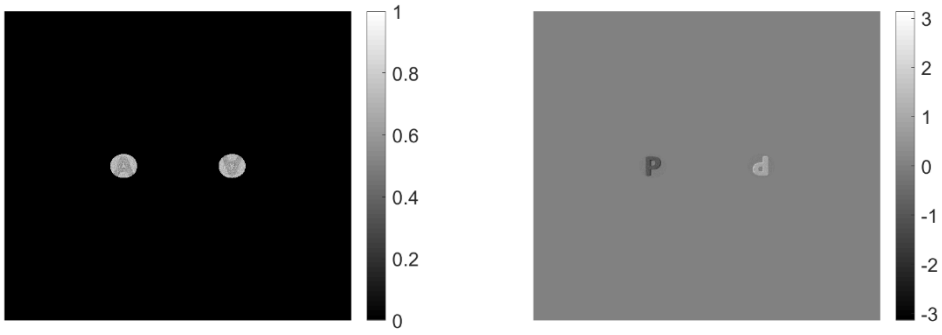

(e) (f)

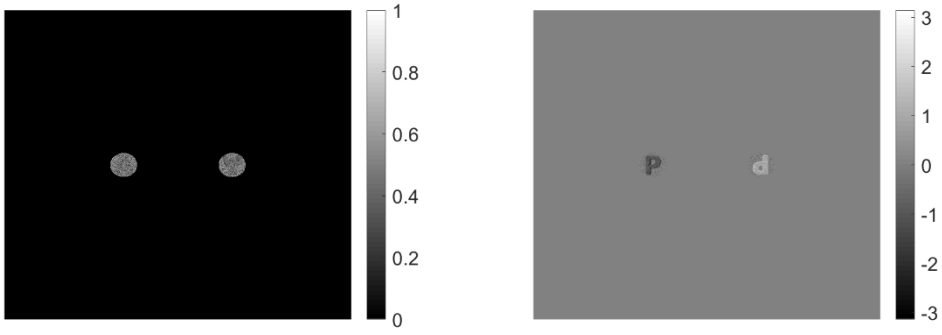

(g) (h)

Figure 4.5: Simulation results when noises are added in the measured data, reconstruction of amplitude and phase (a) and (b) respectively when noise level is 0.05%, (c) and (d) when it is 0.5 %, (e) and (f) noise is 5% and (g) and (h) 50% noise is added with respect to the average intensity value.

4.6 Conclusion

In this chapter, a technique is proposed that involved optical recording, optical to digital conversion, and digital reconstruction of the two dimensional complex object using phase retrieval iterative algorithm. In optical recording, the Fourier hologram is captured optically either by recording the hologram in the Fourier plane or utilizing lensless geometry for the recording. In optical to digital conversion, first the recorded hologram is optically illuminated that generates object-inverted conjugate pair along with DC terms at the reconstruction plane. For blocking the DC term object-inverted conjugate support is placed and the remaining fields are Fourier transformed, and an intensity pattern is digitally captured using a CCD. In the digital recontruction, complex object is digitally reconstructed without twin-image artifact and with fast convergence from the single shot intensity recorded at the Fourier plane. Since our method works only for special object consists object-inverted conjugate pair, our technique is best suited for volumetric holographic data storage and reconstruction, where one has access to such objects. Moreover, our technique works irrespective of the direction of asymmetry present either in object or in the illumination beam; therefore, the proposed method works even in the case where the plane beam is used for the illumination.

Chapter 5

Photograph assisted Phase retrieval algorithm

As mentioned in the previous chapters that, phase retrieval iterative algorithms is an efficient option instead of holography to obtain complex object information from far-field intensity. However, as pointed out earlier in the chapters that there are few drawbacks of the PRA technique over the holography: 1) occasionally reconstruction output from the PRA suffers from the twin-image problem, 2) existing PRA uses random guess as an initial estimation of the object, and on different trails, most of the existing algorithms start with different random guesses resulting non-deterministic outputs. In order to work PRA technique as good as holography, the output should be free from the twin-image problem and it should be unique irrespective of the number of times the algorithm run. To obtain such reconstruction output from the PRA, three methods have been proposed as discussed in 2nd, 3rd, and 4th chapters.

In the second chapter [22], the direction of asymmetry of the object has been incorporated in the PRA to obtain twin-image free unique solution; however, this method is limited to the asymmetric object only.

In the third chapter, a method has been proposed in which, an object is illuminated with EPR scheme to produce the aforementioned output along with fast convergence. This method works for all kinds of objects i.e., symmetric or asymmetric; however, one needs to structure the illumination beam.

In the fourth chapter, a method is suggested, which is limited to the special object containing object-twin pair. Therefore, this method is limited to the volumetric holographic data storage and reconstruction application, where one can have access to such object. The proposed approach works irrespective of the direction of asymmetry of the object. In addition, it operates even in the case of plane beam

illumination withput EPR; therefore, structuring of the illumination beam is also not required.

In the early development of the phase retrieval iterative algorithm, the researchers have employed an photograph of an object along with an intensity of the object recorded at the Fourier plane [29]. However, this technique needs to capture two shots; therefore, this approach is not applicable for real time dynamic objects. Later researchers have utilized holography assisted PRA [30], where the low resolution image obtained from the holography is used as an initial guess in the PRA. However, by incorporating the holography in the PRA, drawbacks associated with the holography get included in the experiments.

Therefore, here a simple method is proposed where a photograph of the object or the amplitude of the object is captured along with the intensity of the object at the Fourier plane. These two information are captured in a single shot by dividing the camera screen into two parts: left and right. Capturing the image and Fourier transform was done previously [31] [32]. Conceptually our method seems similar to the existing techniques referred above; however, we have improved the usability of the method by improving it experimentally. The referred methods need either two cameras or two shots of recording at two different planes. Whereas in our case, we have used only a single camera and recording is performed at a single plane. Apart from this, even though object photograph is available along with the intensity pattern; however, existing methods that employ random guesses produce different outputs on different trails, which results in repeatability problem in the existing method. For more clarity, we have included the simulation in this chapter, when the random guesses are used in different trails along with the photograph of the object and also compared it with our method.

5.1 The flow diagram of the proposed scheme

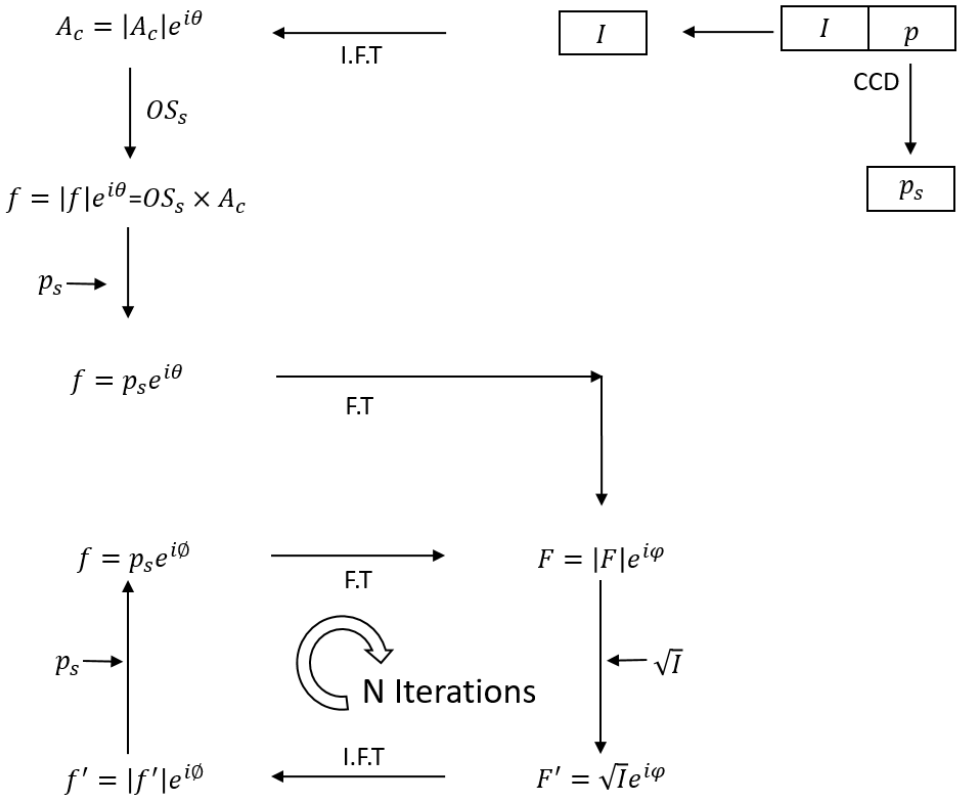

Figure 5.1 : Flow diagram of a photograph assisted PRA.

Flow diagram of a photograph assited phase retrieval algorithm is shown in figure 5.1. In the algorithm, the photograph of the complex object along with far-field intensity is recorded with the camera simultaneously in a single shot. These distributions are denoted with the notations p and I respectively. For processing, these two distributions are separated computationally. An object autocorrelation A_c (two dimensional complex function) is obtained from the intensity by performing a 2D inverse Fourier transform (I.F.T) operation numerically. From the autocorrelation, object support OS information is calculated as mentioned in Appendix B. Note, object support in this case, can also be measured accurately from the photograph of the object using its boundary information. Then to crop a portion from the autocorrelation located at the right side, shifted object support OS_s from the object support is obtained by introducing a shift equal to the radius of the object support along the horizontal direction. Similarly, the photograph of the object is also shifted accordingly and it is denoted with the symbol p_s . A two dimensional

complex function f is created at the object plane by multiplying the 2D complex autocorrelation with the shifted object support. To initiate the algorithm, an initial guess is formed by replacing the amplitude of the function f with p_s. The field at the Fourier plane F is calculated by operating 2D Fourier transform (F.T.) operation on the function f. Since at the Fourier plane one has recorded amplitude information which can be obtained from the recorded intensity I by calculating its square root, the amplitude of the function F is replaced with the square root of the intensity i.e., $\sqrt{I}$, and a new function F' is created. To obtain a field at the object plane f', 2D inverse Fourier transform (I.F.T) operation is performed on F'. At object plane, amplitude information of the function f' is replaced with p_s, and another function f is obtained, this completes the one loop or one iteration of the PRA. This newly formed function f is used in the next iteration in a similar way. Error E, in each iteration, is calculated as given below.

$$E = \frac{\sum\sum(|f'| - p_s)^2}{\sum\sum(|f'| + p_s)^2} \tag{5.1}$$

5.2 Optical setup

The optical setup for recording the far-field intensity at the Fourier plane along with the object photograph is shown in figure 5.2.

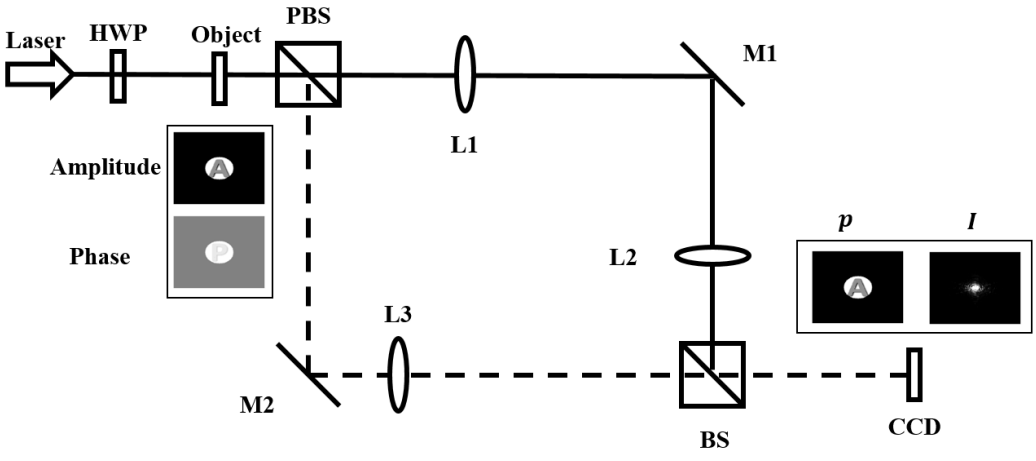

Figure 5.2: Optical setup, in the inset near the laser: amplitude and phase of the complex object is shown, and in the inset near the CCD: amplitude and far-field

patterns recorded simultaneously onto the camera screen in a single-shot are shown.

In the setup shown in figure 5.2, a bounded uniform plane polarized laser light illuminates the complex object. Then the scattered field from the object is propagated and divided into two arms by using a polarizing beam splitter (PBS). These fields recombine at the camera plane with the help of mirror M1, M2, and a beam splitter (BS). One part of the fields denoted with a solid line passes through lenses L1 and L2. These lenses L1 and L2 are formed the 4F imaging system to image the object onto the part of the camera screen. While another part of the field, denoted with a dotted line, passes through the lens L3 and Fourier transformed at the camera plane. To avoid the interference, these two fields are made orthogonally polarized with the help of PBS. In addition, a transverse shift is introduced between these two fields by sliding the mirror M2 or M1 or both accordingly, as a result, these two fields fall on a different part of the CCD screen and do not overlap with one another. Besides, the intensity ratio between the arms can be controlled by introducing a half wave plate before the PBS. The amplitude and phase parts of the complex object are shown in the inset near the laser in figure 5.2. The photograph p and the far-field intensity I at the Fourier plane captured with the camera is also displayed in the inset near the camera in the aforementioned figure.

5.3 Numerical result

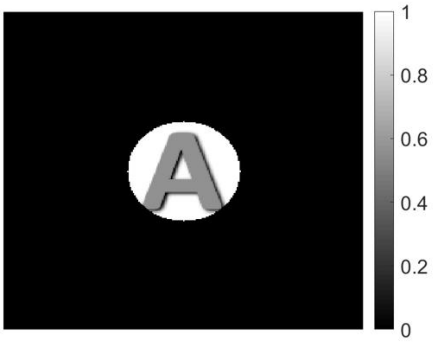

(a) Left: object photograph p

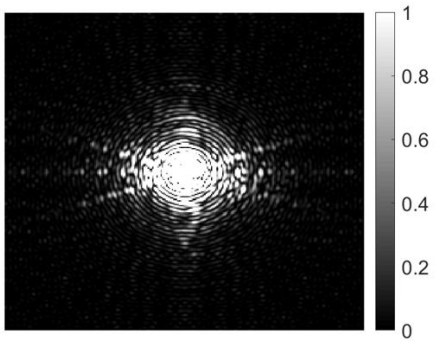

(b) Right: intensity at the Fourier plane I

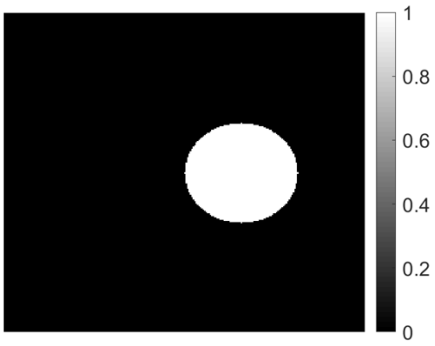

(c) Shifted object support OS_s

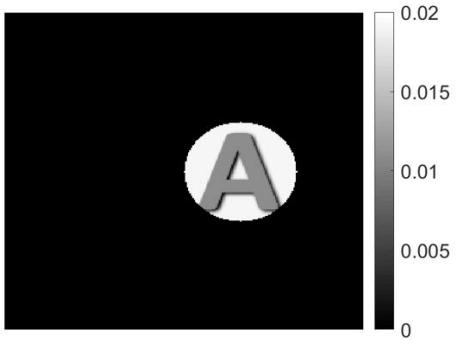

(d) Shifted object photograph p_s

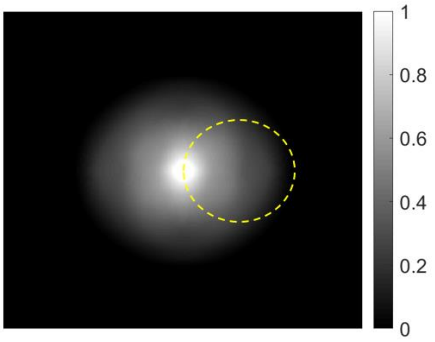

(e) Amplitude of the object autocorrelation

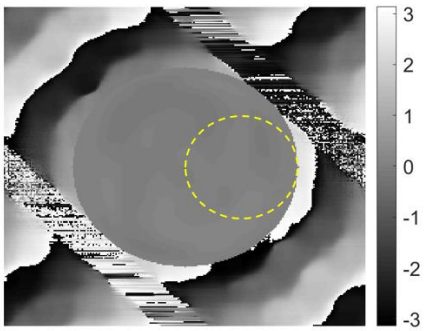

(f) Phase of the object autocorrelation

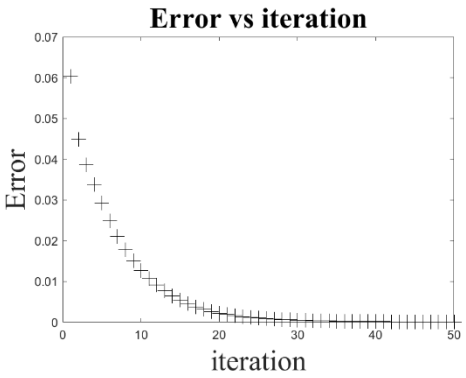

(g) Convergence error

(h) Retrieved phase

Figure 5.3: Numerical result.

For the numerical analysis, a complex object is created using the patterns shown in the inset near the laser in figure 5.2, as an amplitude and phase of the object. Object photograph and the far-field intensity recorded in a single shot are also shown in the inset near the CCD in the same figure. These two information are recorded side

by side in the left and right portions of the CCD screen in a single shot. For processing, these patterns are separated and illustrated in figures 5.3 (a) and (b), respectively. Object support and photograph of the object are obtained at the shifted location as mentioned in the previous section and are displayed in figures 5.3 (c) and (d). Autocorrelation of the object is obtained from the far-field intensity and its amplitude and phase are shown in figures 5.3 (e) and (f). A portion bounded with shifted object support having amplitude as well as phase as displayed with dotted circles shown in figures 5.3 (e) and (f) is cropped from the autocorrelation and used in the PRA as an improved initial guess. The convergence rate of the PRA is plotted in figure 5.3 (g) with respect to the number of iterations. As can be seen from this figure that the error calculated using the equation (5.1), convergences very fast. Reconstruction of the phase of the object only after the 50 iterations is shown in figure 5.3 (h), which matches the phase used for the numerical analysis. For processing, size of the images is considered to be 256×256 pixels^2. Number of iterations used in this case is 50, processing time required to complete the GS algorithm for the aforementioned image size is 11 seconds, and simulation result is carried out without the presence of noise.

5.4 Comparison with random Guess

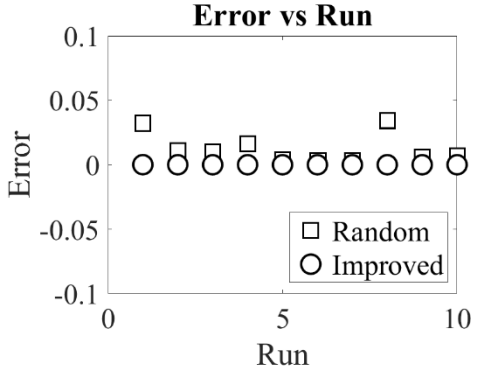

(a)

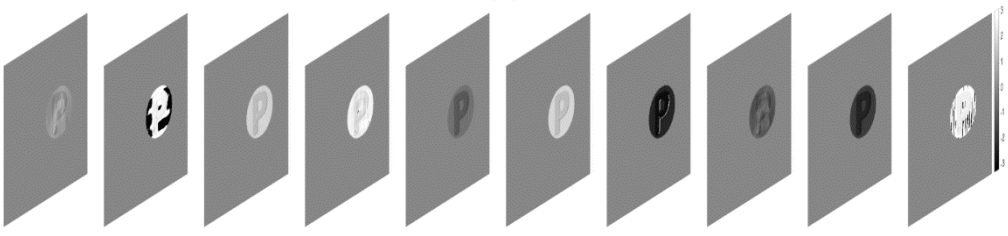

(b)

Figure 5.4: (a) Errors plotted for the reconstruction using random and improved guesses, (b) reconstructions of phase part of the object using random guesses in 10 different trails, each time a new random guess is used as an initial guess.

The errors are calculated using equation (5.1), for two cases 1) random guess, (2) improved guess and are plotted in figure 5.4 (a), these errors are shown with square and circle boxes, respectively. From this figure, it is clear that the error remains constant irrespective of the number of times the algorithm runs, while the error changes when the random guesses are employed as an initial estimations along with the photograph of the object. In 10 different trails, reconstructions of the phase of the object using PRA with random guess are shown in figure 5.4 (b), each time PRA starts with different random guess. From this figure, it can be concluded that even in the case where object photograph is available and employed in the PRA; however, using the random guesses as an initial estimations, the algorithm produces different outputs in different trails.

5.5 Effect of noise

Here simulations are carried out when noise levels 0.05%, 0.5 %, 5% and 50%, respectively are introduced with respect to the average intensity value present in the measured intensity pattern.

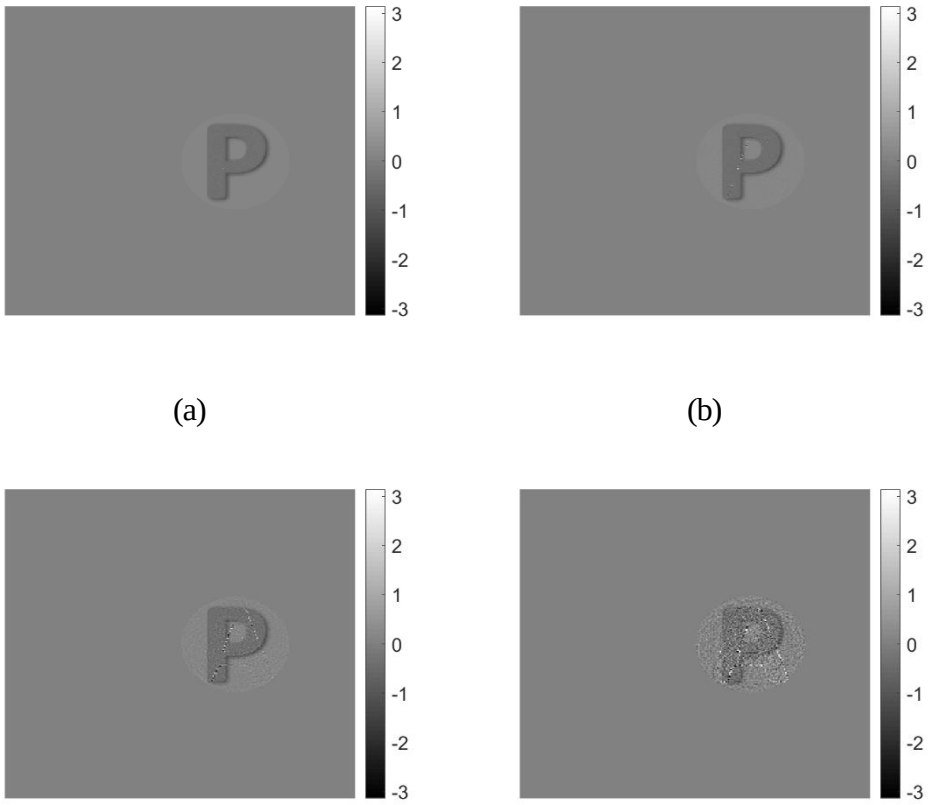

Figure 5.5: Simulation results when noises are added in the measured data, reconstruction of phases (a), (b), (c) and (d), when noise levels are 0.05%, 0.5%, 5% and 50% , respectively are added with respect to the average intensity value.

From the above figure, it can be seen that reconstruction is possible till the noise level of 50 % with respect to the average intensity value present in the intensity pattern for a given image's size and number of iterations.

5.6 Conclusion

The proposed method successfully reconstructs the phase of the object from a single-shot intensity pattern. In this technique, the far-field intensity along with the photograph of the object is captured on a single screen of the camera side by side. The proposed method performs well for all kinds of objects i.e., symmetric and asymmetric and due to the single shot in nature, it can be applied for dynamic real-time situations also. In the proposed method, plane beam illumination is used therefore, one does not need edge point referencing scheme. This technique can be used in various situations where the phase part of the object contains valuable information e.g., biomedical imaging, deformation measurement in real time, wavefront sensing etc.

Chapter 6

Reconstruction of complex-object using edge point referencing

For imaging the complex-valued object, generally Digital Holography (DH) is used. In holography, the requirement of a separate reference source could restrict its application. Investigating objects through recording multiple holograms demands a vibration free platform to keep the reference field stable. Without the reference field, one can obtain only the object autocorrelation from the far-field intensity pattern. A compact, robust, lensless, common path and non iterative method is designed and developed here to retrieve the complex object information directly from the object autocorrelation using edge point referencing, in which the field at a point located at the periphery of the beam illuminating the object is controlled. The results show that the object field can be reconstructed and object dynamics can be monitored with high fidelity.

6.1 Introduction

The analogue holography introduced by Gabor [33] allowed encoding of the complex optical field $o(r)$, upon interference with a coherent reference field $R(r)$, in the intensity of the superposed fields which could then be detected using a photo emulsion plate. Although the plate can capture the intensity pattern with very high spatial resolution and dynamic range thanks to its small grain size and sensitivity, the fact that it can only be used once and requires further chemical processing has limited its usability. While, digitizing the hologram [34], by directly recording the intensity using CCD or CMOS sensors allows subsequent signal processing in a computer.

$$H = |o(r)|^2 + R(r)^2 + o(r)\, R^*(-r) + o^*(-r)R(r). \qquad (6.1)$$

In a single digital hologram H representing the intensity of the superposed fields, in addition to the useful term that represents the object field multiplied by conjugate

and inverted of the reference field $o(r)\ R^*(-r)$, there are also unwanted terms such as intensity of object field $|o(r)|^2$, intensity of reference field $|R(r)|^2$ and the conjugate and inverted of the object field multiplied by reference field $o^*(-r)R(r)$. During the reconstruction process, when numerically propagated to the plane of the object from the plane of the hologram, these unwanted terms undesirably contribute to the reconstruction. Approaches have been suggested either to separate these unwanted terms spatially at the object plane or to remove them from the hologram itself. The off-axis holography proposed by Leith and Uptneiks [9], where a single hologram is captured by introducing an angle between object and reference beam such that the desired term in the reconstruction becomes separated from the unwanted terms. The retrieval of the complex field representing the object is thus achieved by a single acquisition; hence, one can achieve the high temporal resolution. This, however, comes at the cost of sacrificing some spatial resolution. Due to the present of unwanted terms in the reconstruction and employed spatial frequency filtering for the useful term; the achievable spatial resolution is confined. The Phase Shifting Holography (PSH) [10] proposed by Yamaguchi and Zhang, where the reference and object fields can still be in-line (propagated parallel to each other), provides higher spatial resolution. Since there is no spatial filtering involved, the whole area of the recording is exploited. In this case, the retrieval of the complex field can only be achieved by recording multiple holograms. One can get the object reconstruction by introducing sequential phase-shifts to the reference field; however, on the cost of low temporal resolution. Thus the access to the complex field comes at the cost of either spatial or temporal bandwidth/resolution.

The schemes employing recording of three or multiple holograms, demand precise introduction of phase-shifts and a vibration-free environment, restricting their use in real-time conditions. Therefore, several schemes have been proposed which optimize the recording procedure and bring down the number of recordings to two. Guo and Devaney [35] and Wang et al. [36] experimentally demonstrated a Quadrature Phase Shifting Holography (QPSH) technique, also known as two-step phase shifting, as first proposed by Gabor and Goss in 1960s [37]. In QPSH, two quadrature holograms along with object and reference beam intensities are recorded

in order to retrieve the complex valued object. Meng et al. [38] evolved the idea of QPSH, where the two holograms and only the intensity of the reference beam are needed to fully recover the object. This idea is further improved by Liu and Poon [39], who showed that two quadrature holograms alone are sufficient to retrieve the object information. However, this approach works well only when the intensity of the reference beam is higher than the object beam. The scheme introduced by Takaki et al. [40], employs two shutters and a liquid crystal phase modulator to remove the undesired terms. However, this technique still requires capturing three distributions: interference pattern, reference and object intensities. Demoli et al. [41], presented a method based on subtracting two holograms recorded at two different movements of time, which are stochastic in nature. The issue with this method is that it needs an uncontrolled vibration environment and the authors do not fully account for the unknown phase-shift that might have been introduced between the object and the reference fields. Another drawback of this approach is that justification of the removal of object autocorrelation based on the Taylor series expansion is unsatisfying.

During the back propagation from the far-field intensity pattern recorded for an object, a pair of object and its inverted-conjugate known as twin are produced for every object point. The location, orientation and overlap of the object-twin pair is decided by the location of the object point. Resulting distribution from the superposition of the pairs is the object autocorrelation. Therefore, without the reference field, one can obtain only the object autocorrelation from the far-field intensity pattern. We show that a single pair of object and its twin can be extracted from these several overlapped pairs by modulating phase or amplitude of an object point located at the periphery of the illuminating beam, by employing an additional beam. As compared to the iterative method mentioned in 3rd chapter, here additional beam needs to be focused tightly onto the object surface. In addition, far-field intensity patterns are sequentially recorded by modulating the intensity of this additional beam. With the proper weighted subtraction and back-propagation through a numerical Fourier transform operation on these recorded intensities, the proposed scheme can uniquely capture the amplitude and phase information of the complex object non-iteratively.

The control of the amplitude of a point source at the periphery of the illuminating beam seems similar to that implemented in the 'subtraction holography' [41], 'Slightly off-axis Holography' [42], and dOTF method proposed by Codona et al [43]. Some points are discussed here to draw out the novelty. As mentioned earlier, the subtraction holography depends on randomly introduced phase-shift between the object and the reference fields, that get reflected as amplitude or intensity change at the hologram. This makes it hard to decide the right time for the hologram recording. The resolution can be improved and aberrations caused by lenses can be reduced in slightly off-axis lensless geometries shown in figures 6.1 (a) and (b) as compared with fully off-axis geometry. Being only slightly off-axis, in principle, it demands recording of more than one hologram to recover the object and its twin. The reference being separate and independent of the object field, surrounding vibrations can introduce an unknown amount of phase shifts in the investigation of object dynamics as well. For the interference, the path delays between the object and the reference fields should be within the coherence length. This puts a restriction on the location and path of the reference point source as mentioned in figure 6.1 (c).

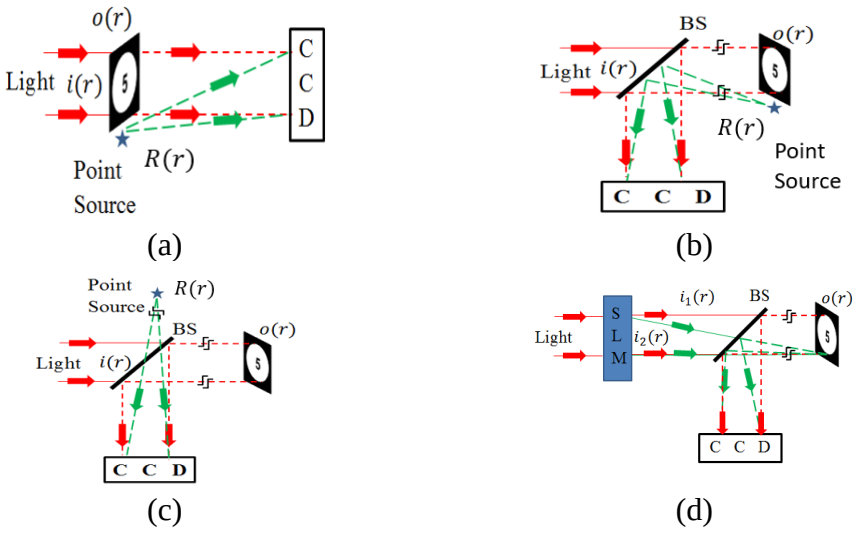

Figure 6.1: (a) Conceptual diagram for slightly off-axis lensless geometry for transparent object, (b) and (c) for reflecting object, (d) conceptual diagram with edge point referencing. $o(r)$, $R(r)$and $i(r)$ denote the object, reference and

illumination field, BS and CCD denote the beam splitter and charge couple device camera.

In proposed approach as shown in figure 6.1 (d), by controlling the field at the extreme point of the illuminated object, shows that the object field can be reconstructed and object dynamics can be monitored with high fidelity. Since object edge point is acting as a reference point and located on the object plane, the overall setup becomes a common path and immune to the external vibration. Additionally, path length between the object and reference (edge point of the object) is almost zero in our case, as compared to the methods shown in figures 6.1 (a) to (c), where one needs to place the reference source within the coherence length. In Codona approach, where modifying the field near the edge using bits of wire, or a needle, one can obtain the object; however, inserting a wire or a needle near the edge modifies a larger area of the object near the edge that leads to the blurring in the reconstruction, which can be seen from their reconstruction result. On the other hand, in our approach, we are also controlling the area of the illumination near the edge by focusing the beam tightly onto the object surface. The illumination beam is tightly focused or not onto the object surface is also verified by measuring the speckle size generated at the camera plane. Since to obtain a interference pattern with high contrast or with a high signal to noise ratio, one should have almost equal intensities in the reference as well as in the object fields. Therefore, by modifying the field near the edge using a single DM actuator as mentioned in the dOTF method, one can change the phase of few points of the object near the edge and in their case, reconstruction may be possible without any blurring, however, due to the single DM modification, strength of the modification will be very small, which changes the interference pattern slightly that results in low signal to noise ratio. Therefore, in their case, for capturing the interference pattern, a high dynamic range camera may be required to sense that small modification. Additionally, by modifying the phase instead of amplitude one can control the SNR to some extent only. While, by modifying the amplitude one can control the SNR accordingly by changing the intensity ratio between the two beams. Besides, it has been shown that by using an intense reference point source near the object, the object-twin pair generated can be enhanced over the object autocorrelation [44] [45] significantly.

This phenomenon is utilized here to monitor the dynamic object in real time i.e., thermal and mechanical loading effect. In practice, it will require an image sensor with high dynamic range to capture superposition of weaker object field with the intense reference field. By modulating the phase near the edge or inserting a wire as suggested in Codona approach, real time analysis is not possible due to the faint signal of the cross terms over the unmodulated terms.

The illumination beam in our scheme should have capability for edge point referencing. This kind of beams can easily be obtained with the help of spatial light modulator (SLM) as mentioned in introduction chapter. The capability of the proposed scheme is also explored to reconstruct a three dimensional object. For the proof of the principle, in this chapter, a Sagnac interferometer to generate the illumination beam with edge point referencing capability is used. This can be a cost-effective option. In comparison, SLM can bring the flexibility in dealing with objects located at different distances and having different sizes. In implementation using Sagnac interferometer, the object is illuminated with two coherent beams simultaneously. One beam stays collimated; and where it meets the object surface, the other beam converges tightly at a point on its edge. Due to the diffraction limited imaging and possibility of focal spot not coinciding with the object surface, converging beam may illuminate a few edge points instead of a single point of the object. To understand its effect in object reconstruction, a simulation study is also carried out.

6.2 Principle

Any object can be considered as a spatially distributed points having complex amplitudes. The object autocorrelation results in the generation of spatially distributed object copies weighted by the conjugate of complex amplitude of the corresponding individual points. In addition, the conjugate and inverted (twin) of these copies will also be generated at diagonally opposite locations. To select a single copy of the object from the overlaps resulting from the autocorrelation, an edge point referencing scheme is presented, where the object is simultaneously illuminated with two beams having transverse distribution $i_1(r)$ and $i_2(r)$ respectively.

Let us suppose a portion of reflected (or transparent) object $o(r)$ is illuminated with beams $i_1(r)$ and $i_2(r)$, the radius of the illuminated portion of the object is equals to x_o as shown in figure 6.2. The scattered field $g(r)$ can be written as,

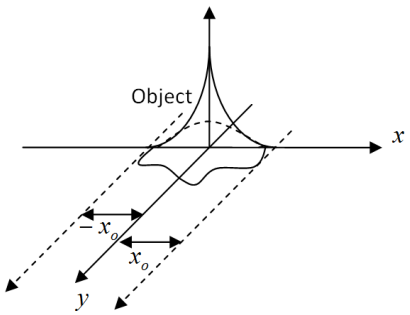

Figure 6.2: Two dimensional complex valued object field.

$$g(r) = \sum_{p=1,2} i_p(r) \times o(r) \quad . \tag{6.2}$$

Where $r = (x, y)$ represents a two-dimensional coordinates system and $o(r)$ is the complex object. The diffraction pattern at the far-field can be obtained by simply taking its Fourier transform as,

$$G(k) = F.T.\left[g(r)\right] \quad . \tag{6.3}$$

Where $k = (k_x, k_y)$ is the two-dimensional spatial frequency coordinates, $F.T.$ denotes the Fourier transform operation. Let us suppose a camera is placed at this plane to record the intensity of the diffraction pattern, which can be written as

$$I = \left|G(k)\right|^2 \quad . \tag{6.4}$$

The inverse Fourier transform $(I.F.T.)$ of the recorded intensity can be described as,

$$\tilde{g}(r) = I.F.T.\left[I\right] = g(r) \otimes g^*(-r) = \sum_{p,q=1,2} i_p(r) \times o(r) \otimes i_q^*(-r) \times o^*(-r) \quad . \tag{6.5}$$

Where the operators $*$ and $\otimes$ denote the complex conjugate and convolution operations, respectively. $\tilde{g}(r)$ represents the autocorrelation of $g(r)$, containing four terms in the right hand side of equation (6.5). However, unlike the holographic equation (6.1), each term in equation (6.5) contains the object information, therefore, even if object oscillates due to the surrounding vibration, edge point of the object also moves in a similar manner; therefore, edge point referencing

provides immunity against the external vibration, which is hard to achieve in holography as mentioned in the introduction chapter. Therefore, our method results in repeatable and stable reconstruction.

Consider a case where $i_1(r)$ and $i_2(r)$ are chosen to be a uniformly distributed plane beam of radius x_o and a focused Gaussian or converging beam (shifted delta function) at the object surface, respectively. Mathematically they are expressed as,

$$\begin{aligned} i_1(r) &= 1 \qquad (r \le x_0) \\ i_1(r) &= 0 \qquad (r > x_0) \\ i_2(r) &= c\delta(r - x_0) \end{aligned} \tag{6.6}$$

Where c represents the weighted complex amplitude and $\delta(r - x_0)$ denotes the shifted Dirac delta function. The object is thus illuminated by $i_1(r)$ and one of its points located at x_o receives an additional contribution from $i_2(r)$. Size of $i_1(r)$ should be smaller or equal to the extent of the object. The choice of the location of reference point will be explained later in this section. Substituting $i_1(r)$ and $i_2(r)$ from equation (6.6) into equation (6.5) leads to:

$$\begin{aligned} \breve{g}(r) = o(r) \otimes o^*(-r) + |c|^2 |o(x_o)|^2 \otimes \delta(r) + \\ c^* o^*(x_o)[o(r) \otimes \delta(r + x_o)] + c\, o(x_o)[o^*(-r) \otimes \delta(r - x_o)]. \end{aligned} \tag{6.7}$$

Our goal is to extract the 3rd term from the autocorrelation, which contains the object information. Graphically, terms in autocorrelation can be illustrated as shown in figure 6.3 (a).

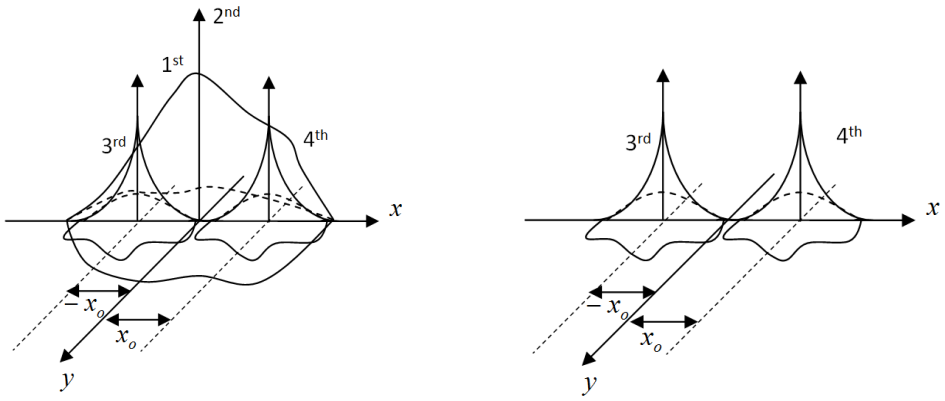

(a) (b)

Figure 6.3: (a) object autocorrelation : 1st term in equation (6.7) shows the DC term, 2nd term shows the edge point intensity and 3rd and 4th terms correspond to the object and its twin weighted by complex amplitude (b) Extracted object $o(r)$ and its twin $o^*(-r)$ (2nd and 3rd terms in equation (6.10), respectively).

According to the equation (6.7), 3rd term, which contains the object information $o(r)$ depends on the amplitude (c) of the 2nd beam. By modulating the amplitude of 2nd beam to c_1 to c_2 and recording two diffraction patterns sequentially lead to the following expressions

$$\breve{g}_1(r) = o(r)\otimes o^*(-r) + |c_1|^2|o(x_o)|^2\otimes\delta(r) + c_1{}^* o^*(x_o)[o(r)\otimes\delta(r+x_o)] + c_1\, o(x_o)[o^*(-r)\otimes\delta(r-x_o)]. \quad (6.8)$$

$$\breve{g}_2(r) = o(r)\otimes o^*(-r) + |c_2|^2|o(x_o)|^2\otimes\delta(r) + c_2{}^* o^*(x_o)[o(r)\otimes\delta(r+x_o)] + c_2\, o(x_o)[o^*(-r)\otimes\delta(r-x_o)]. \quad (6.9)$$

Since 1st term is independent from the complex amplitude c . Hence, subtracting equation (6.8) from equation (6.9) leads to

$$\breve{g}_2(r) - \breve{g}_1(r) = (|c_2|^2 - |c_1|^2)|o(x_o)|^2\otimes\delta(r) + (c_2{}^* - c_1{}^*)o^*(x_o)[o(r)\otimes\delta(r+x_o)] + (c_2 - c_1)\, o(x_o)[o^*(-r)\otimes\delta(r-x_o)]. \quad (6.10)$$

First term in equation (6.10) is located at the center and one can easily remove this term by setting the value of center's few pixels to zero in the reconstructed distribution and last two terms in the equation (6.10) represent the object and its twin. These terms are located at diagonally opposite locations and completely separated from each other as mentioned in the figure 6.3 (b).

Therefore, In equation (6.7), a single point from the object located at x_o, being at the periphery of the illumination, spatially separates the copy of the object and its twin that it generates in its autocorrelation. By controlling either or both the phase and amplitude at this point through the introduction of 2nd beam (additional beam), the copy of the object and its twin that are located at the $-x_o$ and x_o positions alone can be enhanced/controlled and duly retrieved as shown in figure 6.3 (b).

In our case, without a separate reference point, the highest spatial frequency content in the far-field is decided by the maximum span of object, $2x_o$ as displayed in figure 6.2 [46]. In doing so, as compared to the off-axis holography, where the separation between the reference and extreme point of the object has to be maintained at $4x_o$, a two-fold improvement in field of view is achieved.

6.3 Simulation Results

In the previous section, it was considered that 2nd beam illuminates only a single point of the object. Thus, the 2nd beam is assumed to be a Dirac delta function. However, as described earlier, because of the diffraction limited imaging and possibility of focused spot not coinciding with the object surface, the 2nd beam may illuminate a few points instead of a single point of the object. Therefore, the scattered field, in this case, may not be as uniform as in the case of holography, where a separate reference point source is used. The recovered field is no longer convolved with the delta function as mentioned in equation (6.7) and leads to blurring in the reconstructed object. In order to show this effect, a simulation study is carried out.

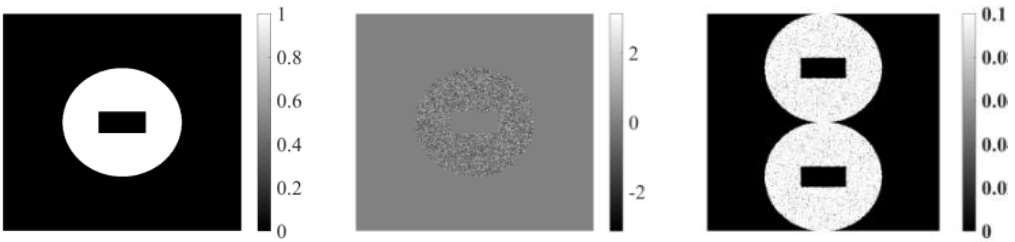

(a) (b) (c)

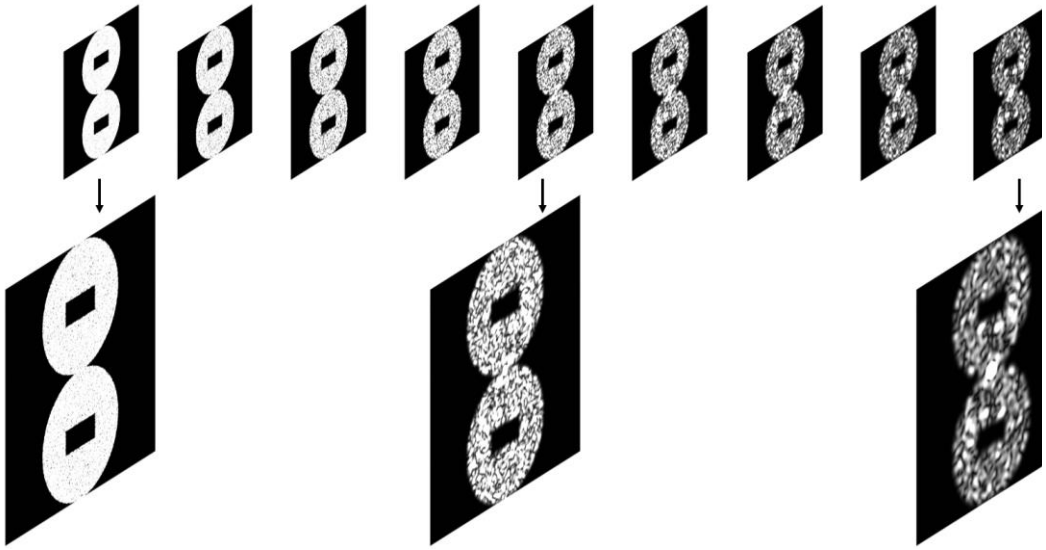

(d)

Figure 6.4: A simulation study, (a) and (b) modulus and phase part of 2D object, (c) reconstructed distribution and (d) effect on the reconstruction with the size of edge point referencing, colorbar in (a) and (c) show the amplitude and in (b) it shows the phase distribution.

For the simulation analysis, a square window of size 4000×4000 pixels^2 is chosen. Pixel size is taken as 5 μm and wavelength of light is set to 0.632 μm. An object restricted within a radius of 5 *mm* as shown in figure 6.4 (a) is selected. A horizontal slit having length of 4 *mm* and width of 2 *mm* is created. To mimic the rough surface, object is also multiplied with the random phase with 20 μm correlation length, phase part of object is shown in figure 6.4 (b). Then the intensity patterns at the Fourier plane are generated with and without the edge point referencing. By using our approach reconstructed pattern is obtained which is shown in the figure 6.4 (c).

To show the effect of the size of 2nd beam, the spot size of 2nd beam is varied from 40 μm (tightly focused) to 240 μm (loosely focused) with a step size of 25 μm. The corresponding reconstructed patterns are shown in the figure 6.4 (d) along with the enlarge patterns. The analysis clearly shows that the reconstruction quality depends on the size of the focused spot of 2nd beam. As long as the size of the speckle generated from this loosely focused beam covers the whole area of CCD sensor, the reference field can effectively be treated as uniform.

6.4 Experimental Procedure

To structure the illumination beams a compact robust common path illumination beam setup (IBS) is designed and developed as shown in figure 6.5 (a) enclosed by the dashed rectangle. IBS consists of a coherent He-Ne laser, which emits light at a wavelength $\lambda = 632.8\, nm$, a half wave plate (HWP) to change the polarization of input light, a collimation unit (CU) and a Sagnac interferometer (SI). CU utilizes the microscope objective lens (MO), a spatial filter (SF) and a lens (L). And SI consists of a polarizing beam splitter (PBS), two mirrors M1, M2 and two lenses L1, L2 each of them having focal length equal to 25 cm.

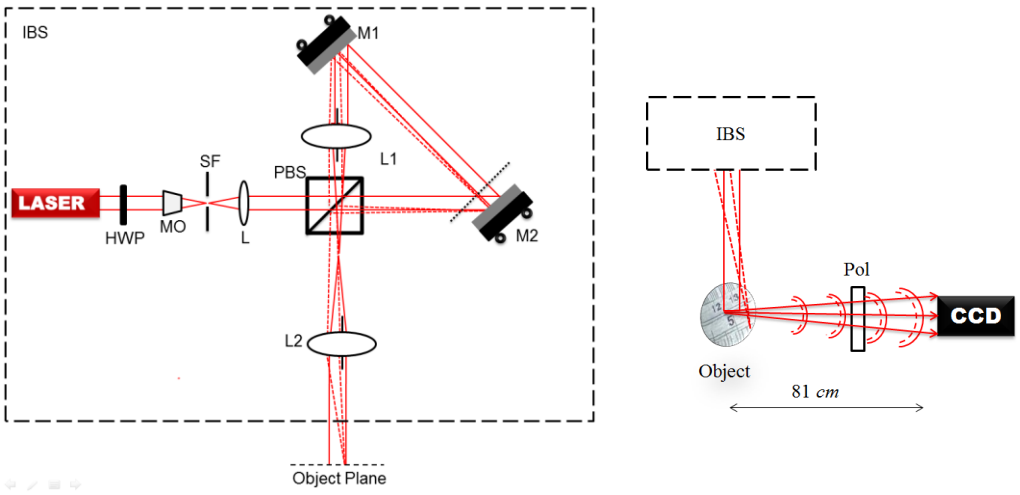

(a) (b)

Figure 6.5: (a) Shows the compact robust common path illumination beam setup (IBS): solid line shows the collimated beam and dotted lines show the converging beam. (b) The lensless imaging setup to image the complex object in reflection geometry. HWP: half wave plate, MO and SF: microscope objective lens and spatial filter, L, L1 and L2 are the biconvex lenses, PBS: polarizing beam splitter, M1 and M2 show the mirrors.

In the setup, laser beam is first collimated by the collimation unit and then passes through the PBS. PBS divides it into two beams: transmitted (horizontally polarized) and reflected (vertically polarized), as delineated by solid and dotted lines, respectively. By introducing HWP before the PBS, the intensity ratio between these two beams can be adjusted. When HWP is oriented at 0^0 , it makes the beam completetly horizontally polarized and in this case, intensity of 2^{nd} beam becomes

almost zero. While, at any other orientation e.g., 4^0, intensity of 2^{nd} beam can be made non-zero. The Lens L1 focuses the beams inside and outside the triangle part of the Sagnac, and lens L2 is placed such that focused point of transmitted beam is collimated, while the focused point of reflected beam is imaged or converged at the center of the collimated beam. Now to shift the focused point or spot from the center to the edge of the illumination, the position of mirror M2 is slightly moved along the direction perpendicular to its plane, at the location indicated by the black dotted line near M2 in figure 6.5 (a). Size of speckle generated by a beam is inversely proportional to its size at the object surface. By scanning the object position longitudinally, one can find the best focused plane of the converging beam onto the object surface by monitoring the size of the speckle pattern it generates at the recording plane. The speckle fields resulting from the object illumination from the two orthogonally polarized beams interfere at the camera by the introduction a polarizer, as shown in figure 6.5 (b).

6.5 Results

For capturing the intensities, a CCD camera (pco pixelfly) having the resolution of 1392×1040, pixel pitch equals to 6.45×6.45 μm^2 and dynamic range of 16 bit is utilized in the experimental setup. For processing the images, out of the full image, sub images of size 1024×1024 pixels are cropped. And to see the results clearly, smaller images of a size of 600×600 are used here for the display. In the experiment, the distance between the camera and object is kept 81 *cm* and diameter of collimated beam is restricted to 1.5 *cm*. These parameters are chosen to make sure that the size of the reference speckle generated by illuminating edge point of the object covers the whole area of the CCD detector.

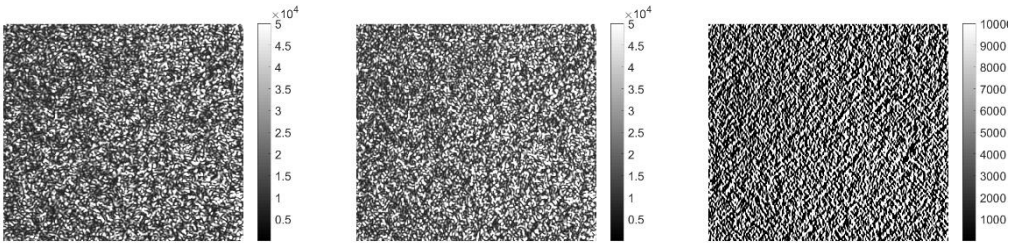

(a) (b) (c)

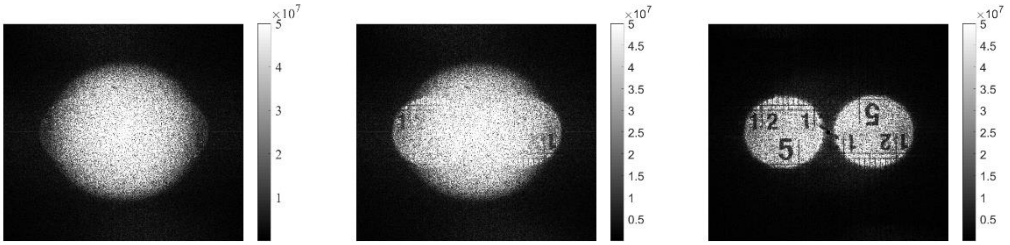

(d) (e) (f)

Figure 6.6: Recorded intensities with HWP oriented at: (a) 0^0 (b) 4^0, (c) Subtracted intensity pattern, (d-f) moduli of autocorrelation corresponding to (a-c), respectively. The colorbar beside each diagram indicates the amplitude values distribution for the respective image.

A portion of metal ruler is used as a reflective object in the setup as illustrated in figures 6.5 (b). Figures 6.6 (a) and (b) display the far-field intensity patterns recorded with the HWP oriented at 0^0 (without 2^{nd} beam) and 4^0 (with 2^{nd} beam) respectively. Figure 6.6 (c) shows the weighted subtracted pattern calculated numerically. Moduli of the autocorrelations obtained by performing inverse Fourier transformation on the patterns shown in figures 6.6 (a-c) computationally, are shown in figures 6.6 (d-f), respectively. It can be concluded that with edge point referencing, in the reconstruction, one copy of object and its twin pair corresponding to the point illuminated with the 2^{nd} beam alone can be enhanced over the distribution by the other copies as shown in figure 6.6 (e). The other copies in figure 6.6 (e) can be eliminated by subtracting the reconstruction pattern obtained without the 2^{nd} beam as shown in figure 6.6 (d). Hence a single pair of object and its twin alone can be extracted as shown in figure 6.6 (f).

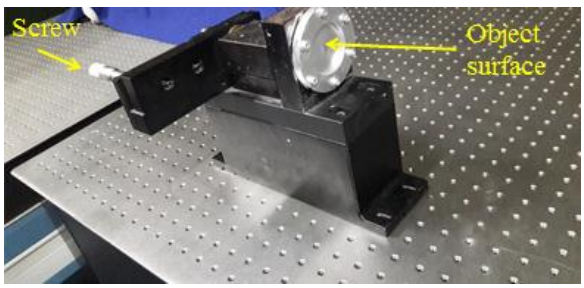

(a)

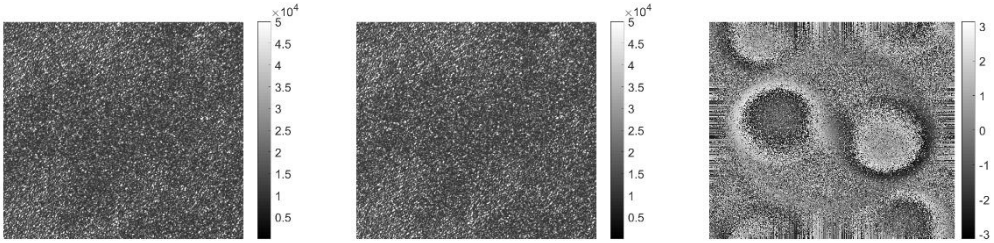

(b) (c) (d)

Figure 6.7: Real-time deformation measurement: (a) deformable object, (b) and (c) show the intensity patterns recorded in undeformed and deformed conditions and compared phase part of autocorrelation is shown in (d), colorbar for (b) and (c) show the intensity values distribution, and in (d) it shows the phase value distribution.

The above technique is suitable only for stable object since two intensities with and without the 2^{nd} beam need to be recorded. In order to capture the dynamic phenomenon, one should increase the intensity of the 2^{nd} beam [44] [45], such that the pair produced from it over the other distributed copies in the reconstruction can be made significant. And contribution from the other copies can be considered as negligible. To prove this part, a centre loaded metal plate is employed as a second object as shown in figure 6.7 (a). A spherical deformation can be introduced in the object by moving the screw forward and backward. With 2^{nd} beam (HWP at 4^0 degree) far-field intensity patterns are captured in unloaded and loaded conditions and are shown in figures 6.7 (b) and (c). Phase of object autocorrelation, obtained in loaded case when compared with unloaded case shows the deformation information as shown in figure 6.7 (d).

Thus far, a two dimensional objects (planar) is used, where; both the reference point and object are located in same plane. To demonstrate the three dimensional object reconstruction where reference and object could lie in different planes, as shown in figure 6.8 (a), two metal rulers separated by 8.5 *cm* is utilized. Some part of collimated beam falls on 1^{st} ruler and illuminates the letter '4' and other part falls on the 2^{nd} ruler and illuminates letter '2'. The converging beam focuses at the 1^{st} ruler at the periphery of the collimated beam.

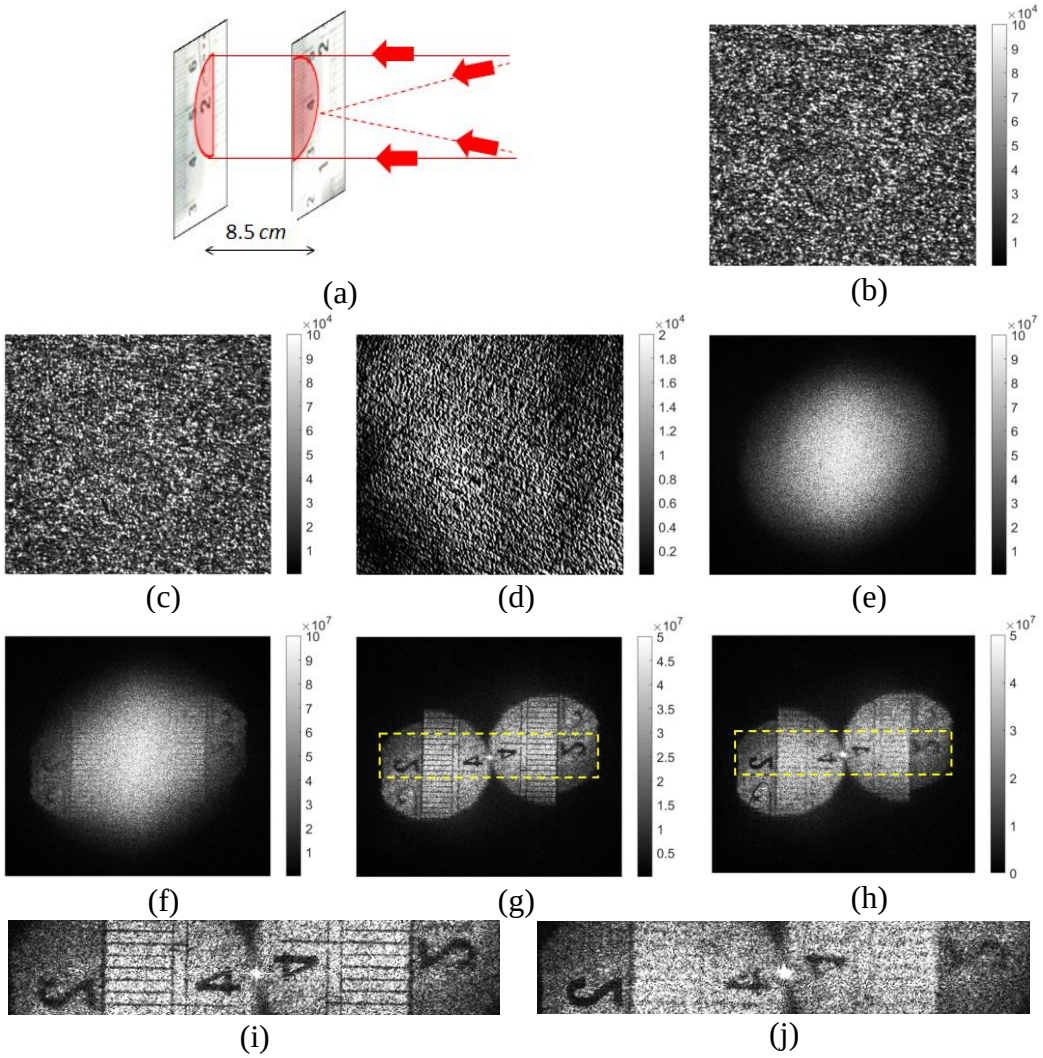

Figure 6.8: (a) Two metal rulers, separated by 8.5 *cm*, are used as a 3D object and solid and dotted lines show the collimated and converging beam, (b) and (c) recorded intensties with HWP oriented at 0^0 and 4^0, (d) subtracted intensity pattern, (e-g) moduli of autocorrelations corresponding to (b-d) respectively, and (h) modulus of propagated field, (i) and (j) enlarged portions of the area enclosed with the dotted lines shown in (g) and (h), respectively.

We record two diffraction patterns as shown in figures 6.8 (b) and (c). Their subtracted pattern is shown in figure 6.8 (d). Moduli of object autocorrelation corresponding to figures 6.8 (b-d) are shown in figures 6.8 (e-g). From the enlarged portion shown in 6.8 (i), one can see the letter '4' (middle portion) in proper focus whereas letter '2' (left hand side) looks defocus. Using the angular spectrum method [47], one can propagate the recovered field for 8.5 *cm*, as shown in figure 6.8 (h). From the enlarged portion shown in 6.8 (j), one can see that letter '2' (left

hand side) comes in sharp focus whereas the letter ‘4’ (middle portion) gets blurred and the twin of letter ‘2’ (right hand side) gets completely defocused. Therefore, using the propagation algorithms, one can numerically focus any plane of the object and reconstruct the 3D object.

6.6 Discussion

In our initial experiment, we were trying to modify the scattered field by placing a NDT (neutral density filter) filter near the object as mentioned in 1st chapter. This NDT filter has a uniform coating throughtout its region except at a small region located near the boundary. We placed this filter near the object such that the location of the edge point of the object matches with the small region where coating is absent. Therefore, intensity of the scattered field reduces uniformly throughout the desired region of the object except near the edge. With this arrangement, we captured the two images with and without blocking the edge point of the object by inserting a black paper infront of a small region. Similar to the Codona approach, the quality of the reconstruction obtained with NDT arrangement was very poor. This degradation in the reconstruction happens because size of small region was not smaller enough to produce speckle pattern that can cover the whole area of the camera in the recording plane. Therefore, we opted the arrangement using optical components as mentioned in figure 6.5 (a), where we can control the size of the 2nd beam onto the object surface as discussed earlier.

6.7 Conclusion

Here a novel method is proposed and demonstrated experimentally to retrieve the 2D as well as the 3D complex object from its autocorrelation. The method utilizes edge point referencing, therefore, does not require any separate reference to record the hologram. The proposed setup is common path and robust to external vibrations. The employment of the amplitude shifting in the proposed setup as opposed to phase shifting also avoids using expensive components required to perform phase shifting operation. By choosing the reference point at the desired/illuminated object boundary leads to two-fold improvement in the field of view as compared to that in off-axis holography. In addition, by keeping the reference point at the desired/illuminted object boundary reduces the highest frequency content (spatial

carrier frequency) in the hologram leading to better sampling of the hologram/ recording larger size hologram by using same size and pixel resolution of a CCD camera as compared to that in off-axis holography. This inturn improves the resolution of the reconstruction. However, unlike digital holography, in this scheme the converging beam, needs to be at focus precisely on the object surface for good quality object reconstruction. The theoretical analysis of the proposed technique and the experimental results highlight the complex object reconstruction abilities and advantages over the in-line phase shifting and off-axis holography. The proposed method also shows great potential in some practical applications such as measuring the real time deformation.

Chapter 7

Discrete and quantitative reconstruction of the out of plane non-linear deformation using local autocorrelations

7.1 Concept

Non-destructive optical technique for deformation measurement has several applications in various fields. Existing methods for deformation measurements either use holographic technique which is limited to vibration free environment or digital image correlator method which uses complicated setup and needs high computing power. Here, a simple optical technique is proposed that is based on the fact that nonlinear deformation can be treated as linear within a small region. Therefore, the whole object surface deformation can be measured by dividing the entire surface of the object into many smaller regions or sub-regions by employing a mask. Thus by calculating the linear deformation for all the sub-regions and stitching those in their respective locations; discrete version of the deformation can be measured in less computational steps. In addition, how full-field deformation can be measured using our method for quantitative purposes is also discussed. Besides, the results are also compared against the established technique such as speckle correlation method where mask is not present in the setup. The comparison shows that by utilizing the mask, we achieve higher signal to noise ratio compared to speckle correlation technique. For the validation of the concept, theoretical analysis along with simulation and experimental results is presented.

7.2 Background

Prerequisite conditions for existing techniques such as deformation measurement [48] and wavefront sensing [49] are based on measuring change in phase between the optical fields scattered from the object before and after the deformation. Deformation measurement technique is most commonly used in the automobile industries and in the construction of buildings or bridges to monitor the loading conditions, while wavefront sensing is beneficial in astronomy and metrology for

monitoring the wavefronts. In such areas, the amplitude part contains no useful information; however, capturing the phase change of the optical fields remains crucial. In order to do so, several techniques have been proposed in the past. The most commonly used techniques are Shack Hartmann sensor [50] and digital image correlator (DIC) [51] [52].

In the Shack Hartmann wavefront sensor technique, a mask is used before the sensor which contains grid of cells and each cell contains a small converging lens [50]. The role of each lens is to converge or focus the light onto the sensor at some location. Based on the mask, sensor's screen is devided into many small images or sub-images. Location of the focused light within the sub-image changes according to the linear tilt present in the part of the wavefront which falls within the respective cell. For each sub-image, shift in locations between the points containing the maximum intensity due to the focused light is measured before and after the deformation. Finally, a change in the phase between the overall optical fields is obtained by calculating all the shifts or displacement vectors for all the sub-images and using modal or zonal method [53-58].

As there are several advantages of the aforementioned technique, there are disadvantages as well [59]. First, mask must have identical lenses for better wavefront reconstruction. Therefore, fabricating such precise identical micro lenses is very difficult. Secondly, generally the size of each lens of the wavefront sensor is of the order of 100 μm; hence, spatial resolution of the sensor is quite low. Thirdly, lenses should have minimum aberration. Fourthly, once the mask is fabricated, one cannot change the number of cells. Lastly, wavefront sensor is mostly used to measure the smooth wavefronts, it does not work for rough surfaces, therefore, this kind of sensors are not suitable for measuring deformation.

DIC technique measures the deformation of a rough object highly suitable for automobile industries. DIC technique can be divided into two: 1) 2D DIC [60] [61]: measures the shape and in-plane deformation i.e., translation and rotation motions, 2) 3D DIC [62]: suitable for measuring the shape of the object and complete deformation information i.e., in-plane and out of plane deformation due to the loading effect. In the 3D DIC, as the name suggests, two separate intensities of the

object should be captured at slightly different angles. In order to do so, either a stereo camera with an imaging setup generally consisting of two cameras for imaging the object [62] [63] is needed or a single camera with complicated optical setup or an optical element to divide the wavefront of the object into two parts [64] [65] is required. The optical setup or optical element is designed and utilized with the intention of capturing stereo images of the object onto a single camera.

Although the DIC technique is currently very popular since it necessitates neither the laser light [66] [67] nor the reference beam [48] [67], nor multiple micro lenses [48] as in the Shack Hartmann sensor. However, there are still some limitations of this technique. First, to record the stereo images, either a complicated high resolution stereo camera or a complicated setup is required to divide the object wavefront into two parts. Second, most of the time the object surface needs to be painted with a random speckle pattern [65]. Sometimes painting the object surface with the random pattern is also not possible, it may damage the surface or the object surface may be located far away (from the reach). Third, since two patterns of the object should be taken at one instant with two cameras, it needs a mechanism to synchronize both the cameras simultaneously [68] [69]. Fourth, 3D DIC measures the large deformation at the cost of low sensitivity [70]. Moreover, before doing the experiment with the object, one needs to calibrate the stereo images with some calibrated pattern [62] [71]. Hence the calibration process in the 3D DIC is also a tedious and time consuming job. Finally, mapping and shape functions are required to find the similarity between the two stereo images as well as in the intensity patterns captured before and after the deformation [62] [72-75]. Considering all these points, DIC method requires high computational power. Besides, in the case of large deformation, matching the similarity between the patterns taken before and after the deformation is difficult and at times, if algorithm is unable to match, it results in junk data [60].

In order to solve all the aforementioned limitations, a technique is proposed here, which incorporates the benefits of the wavefront sensor as well as the DIC technique. Unlike DIC, our technique uses a single camera without any complicated setup to measure the out of plane deformation of an object which is under thermal or mechanical loading. In this method, one needs to illuminate the object with a

coherence source and then one needs to capture the intensity of the scattered field from the object at the far plane. In our method, only two intensity distributions are recorded: before and after the deformation. Besides, unlike the Shack Hartmann sensor, no fabrication of a complicated mask containing the micro lenses is required. Since, in our case, only a single image is needed to be captured at an instant, no need to divide the camera screen into two or three regions as required in the single camera 3D DIC technique [64]. Therefore, our method has higher spatial resolution as compared to single camera 3D DIC technique. Additionally, requirement of the mapping algorithms, the stereo images and the synchronization of cameras are unnecessary. Since, only the object far-field intensity is captured; imaging setup is also not required. Moreover in our case, since recordings have been made in far-field instead of imaging plane, it manages to achieve a higher sensitivity [67] [76].

Our method is based on the fact that comparing the local autocorrelations numerically obtained from a part of the intensity patterns captured before and after the deformation preserves the linear deformation or tilt information of the object. If object is subjected to a nonlinear deformation due to the loading effect, to measure the nonlinear deformation using the above method, we assume that even if the entire surface of the object deforms non-linearly, the deformation of the surface of the object within a small region can still be treated as linear. Thus, entire surface of the object is divided into many small sub-regions using a mask. This mask contains no micro lenses; hence, it is different from the one used in Shack Hartmann sensor. Within a sub-region the linear deformation is first measured and then combined with the linear deformation measured in other sub-regions. This procedure estimates the discrete version of the deformation for the whole object surface by performing fewer numerical operations, as opposed to the DIC technique. Later, shown that full-field deformation or quantitative measurement of the nonlinear deformation is also possible by calculating the displacement vectors for all the sub-regions. Apart from this the situation where mask is absent from the setup is also simulated for the comparison purpose. This comparison shows that our method is better and provides high signal to noise ratio as compared to the situation where mask is absent. In the previous DIC methods, there are no rules to determine the

subset size (in our case size of the sub-image) [72], On the contrary, in our method, a relation is established later in this chapter, which relates the distance between the object and the camera with the size of the sub-image. Besides, for the imaging of the object, a telecentric imaging geometry has been incorporated which has several advantages [77] [78]. In addition to all the advantages of our technique, our technique also suffers from the limitation of measuring the complete object information i.e., amplitude and phase; our technique is only capable of measuring change in the phase or out of plane deformation.

7.3 Derivation

Deformation can be divided into two categories: linear and non-linear. Where linear deformation means tilting the object surface with respect to the initial position and non-linear deformation means deformation in the object surface other than the tilting such as spherical deformation. Let us suppose we have an object whose surface is rough and can deform under mechanical or thermal loading condition. Our aim is to determine the object surface deformation non-destructively induced due to the loading condition.

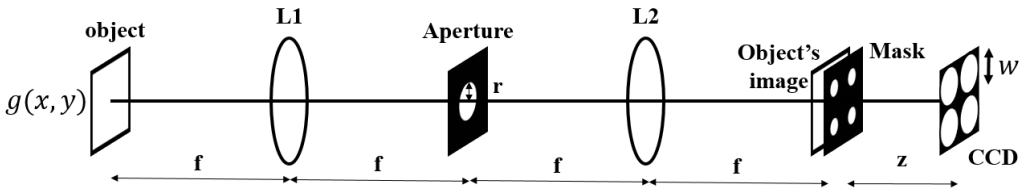

(a)

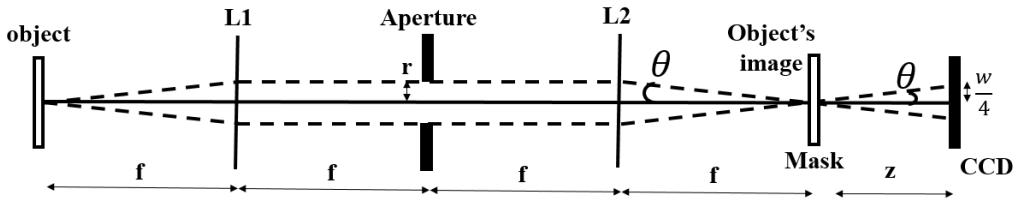

(b)

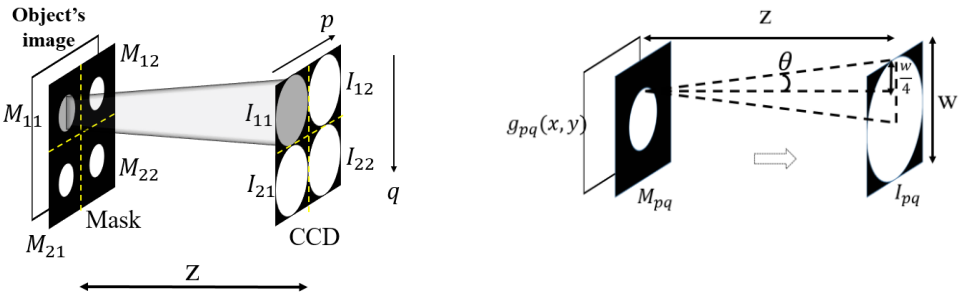

(c) (d)

Figure 7.1: (a) Setup for measuring deformation, (b) ray diagram of the setup, (c) shows how a mask having 2 × 2 cells divides the object into 2 × 2 sub-regions and results in creating 2 × 2 sub-images, this figure also shows that scattered field from a sub-region of the object that is behind a cell of the mask (M_{11}) propagates and falls on a small part the camera i.e., sub-image (I_{11}), (d) enlarged portion of a sub-region of the object $g_{pq}(x, y)$ which is behind M_{pq} and respective sub-image I_{pq}, where subscript p and q represent the corresponding location, located at pth row and qth column.

To measure the deformation, we illuminate the object with a coherent laser light of uniform intensity. Then the scattered field from the object is first imaged using a telecentric system employing two lenses L1 and L2 having equal focal lengths as shown in figure 7.1 (a). Under loading condition, surface of the object can deform into any shape; however, the deformation within a smaller region can still be treated as linear and it can be measured calculating respective autocorrelation. To divide the entire surface of the object into sub-regions, a mask is fabricated and placed at the imaging plane of the telecentric geometry as shown in figure 7.1 (a). The mask is an opaque plate that contains many small circular openings located at periodic locations. In contrast to the Shack Hartmann sensor; the mask that is used here does not employ micro lenses. Apart from this, a variable aperture is used inside the telecentric system to control the divergence θ of the scattered fields. Ray diagram of the setup is shown in the figure 7.1 (b). According to the figure 7.1 (b), a geometrical relation can be established as given below,

$$\tan\theta = \frac{\mathrm{r}}{\mathrm{f}}. \qquad (7.1)$$

The scattered fields from different sub-regions diverge according to equation (7.1) and the divergence θ can be controlled by varying the aperture radius r. The advantage of placing the mask and variable aperture is that scattered fields propagate and fall on respective small parts or sub-images of the CCD camera without overlapping with one another. Therefore, for each sub-region of the object, one can find a respective sub-image at the camera plane that captures the intensity of the field falling onto it. Note, for an ideal mask where spacing of the openings is located at equal distances from each other, corresponding sub-images are also located at periodic locations. A portion of the setup shown in figure 7.1 (a) is enlarged and shown in figure 7.1 (c), in which a mask having 2×2 cells is shown for simplicity. Each cell of the mask contains an opaque square window with a small opening; shown in with black and white color, respectively. This mask divides the object surface into 2×2 sub-regions and respectively 2×2 sub-images can be found from the intensity captured using the camera. Figure 7.1 (d) shows a particular sub-region of the object $\mathrm{g}_{pq}(\mathrm{x},\mathrm{y})$ which is behind a cell of the mask M_{pq} and respective sub-image I_{pq} located at p^{th} row and q^{th} column. From the figure 7.1 (d), if a camera is placed at distance z away from the mask the size of sub-image can be determined as follows,

$$\mathrm{w} = 4\mathrm{z}\tan\theta\,. \tag{7.2}$$

Substituting $\tan\theta$ from equation (7.1) into equation (7.2), and rewriting in terms of z

$$\mathrm{z} = \frac{wf}{4r}\,. \tag{7.3}$$

Where $\frac{wf}{4r}$ represents the defocused distance. For this method to work efficiently, two conditions should be met; 1) the fields scattered from sub-regions should not overlap with one another at the camera plane as displayed in figure 7.1 (c), the overlapping begins when the distance between the mask and camera is greater than the defocused distance, i.e., $z > \frac{wf}{4r}$, 2) the distance between the mask and the camera should be kept such that the field scattered from a sub-region of the object's image diverges and covers the whole area of the respective sub-image as shown in

figure 7.1 (d), if the distance between the mask and the camera is less than the defocused distance, $z < \frac{wf}{4r}$, the field scattered or diverged from a sub-region does not cover the whole area of the respective sub-image of the CCD. Therefore, in order to meet the above two conditions equation (7.3) should be satisfied.

By designing the experimental setup using the relations mentioned in equations (7.1) to (7.3) as shown in figure 7.1 (a) two intensities are captured i.e., one before and one after the deformation i.e., I and I'. For processing these intensities, whole procedure is depicted in figure 7.2. In the procedure, first we need to find all the sub-images locations. As we have mentioned before for an ideal mask, all the sub-images are having equal size and located at periodic location and their locations can be obtained easily. Note, for a particular design of mask, locations of sub-images are fixed and required to be measured only one time; therefore, in our case we do not require to search the sub-image location after the deformation thus eliminating the need of a mapping algorithm as required in DIC. Second, for measuring deformation within a smaller region, sub-images I_{pq} and I'_{pq} from the intensities I and I' are cropped and selected. Here onwards we refer the function calculated within the sub-image as local.

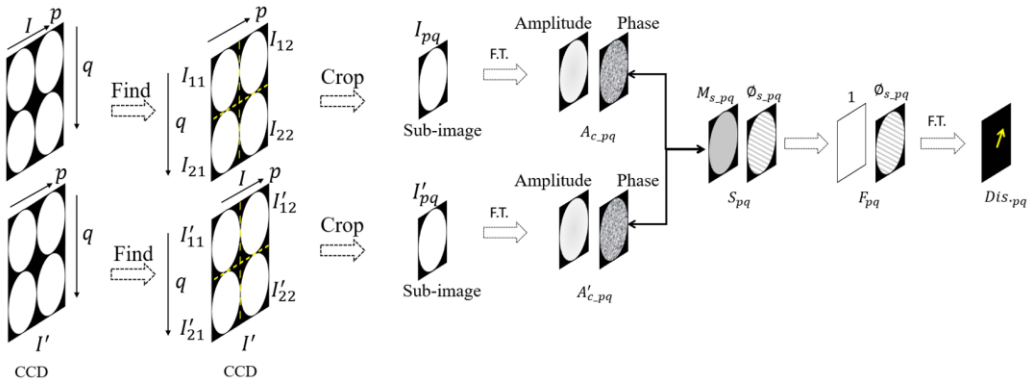

Figure 7.2: Procedure for measuring nonlinear deformation.

According to figure 7.1 (d), a part of object's image which is behind a cell of the mask M_{pq} can be written as a complex-function, represented by $g_{pq}(x, y) = |g_{pq}(x, y)|e^{i(\emptyset_{pq}(x,y))}$ having amplitude as well as phase part. Where x, y denote the coordinates at the image plane, $|g_{pq}(x, y)|$ and $e^{i(\emptyset_{pq}(x,y))}$ denote the amplitude

and phase respectively and p and q represents the location of a sub-region located at p^{th} row and q^{th} column.

The scattered field from the corresponding sub-region propagates at Fourier plane and can be obtained as follow

$$\mathrm{G}_{pq}(\mathrm{k_x}, \mathrm{k_y}) = \mathrm{F.T.}\left(\mathrm{g}_{pq}(\mathrm{x}, \mathrm{y})\right). \tag{7.4}$$

Where $\mathrm{F.T.}$ represents the Fourier transformation and $\mathrm{k_x}, \mathrm{k_y}$ denote the spatial coordinates in the Fourier plane. This field falls on a sub-image $\mathrm{I_{pq}}$ which captures the intensity of the field falling onto it and that can be written as follow

$$\mathrm{I_{pq}} = \left|\mathrm{G}_{pq}(\mathrm{k_x}, \mathrm{k_y})\right|^2. \tag{7.5}$$

Since from the equation (7.5), the sub-image contains only the amplitude part, we cannot retrieve the $\mathrm{g}_{pq}(\mathrm{x}, \mathrm{y})$ directly by simply applying the inverse Fourier transformation. Instead by performing the inverse Fourier transformation operation on the $\mathrm{I_{pq}}$, the local autocorrelation $\mathrm{A_{c\_pq}}$ of the sub-region of the object's image is obtained as

$$\mathrm{A_{c\_pq}} = \mathrm{I.F.T.}\left(\mathrm{I_{pq}}\right) = \mathrm{g}_{pq}(\check{\mathrm{x}}, \check{\mathrm{y}}) \otimes \mathrm{g^*}_{pq}(-\check{\mathrm{x}}, -\check{\mathrm{y}}). \tag{7.6}$$

Where $\check{\mathrm{x}}, \check{\mathrm{y}}$ represent the coordinates of the reconstruction plane. Rewriting the above equation by expanding the convolution operator results in

$$\mathrm{A_{c\_pq}} = \int \mathrm{g}_{pq}(\zeta, \eta)\mathrm{g^*}_{pq}(\zeta - \check{\mathrm{x}}, \eta - \check{\mathrm{y}})\mathrm{d}\zeta\, \mathrm{d}\eta. \tag{7.7}$$

After the deformation, as we mentioned before that deformation within a smaller region could be considered linear; therefore, the field of the object's image which is behind the same cell M_{pq} can be modified with a linear phase factor as follow

$$\mathrm{g'}_{pq}(\mathrm{x}, \mathrm{y}) = \mathrm{g}_{pq}(\mathrm{x}, \mathrm{y})\mathrm{e}^{\mathrm{i(kx+ky)}}. \tag{7.8}$$

The phase of the factor $\mathrm{e}^{\mathrm{i(kx+ky)}}$ indicates the linear deformation, our purpose is to find the phase part of this factor

Similar to the equations (7.4) and (7.5), expressions $G'_{pq}(k_x, k_y)$ and I'_{pq} can be found for $g'_{pq}(x, y)$. By operating the inverse Fourier transformation on the I'_{pq}, the respective local autocorrelation A'_{c_pq} is obtained as

$$A'_{c\_pq} = I.F.T.\left(I'_{pq}\right) = \int g'_{pq}(\zeta, \eta) g'^{*}_{pq}(\zeta - \check{x}, \eta - \check{y}) d\zeta \, d\eta. \qquad (7.9)$$

Substituting $g'_{pq}(x, y)$ from equation (7.8) into equation (7.9) leads to

$$A'_{c\_pq} = \int g_{pq}(\zeta, \eta) e^{i(k\zeta + k\eta)} \, g^{*}_{pq}(\zeta - \check{x}, -\check{y}) e^{-i(k(\zeta - \check{x}) + k(\eta - \check{y}))} d\zeta d\eta. \qquad (7.10)$$

Simplify and rewriting the above equation using equation (7.7)

$$A'_{c\_pq} = e^{i(k\check{x} + k\check{y})} A_{c\_pq}. \qquad (7.11)$$

From the above equation it is clear that the linear deformation factor is invariant and can be extracted from the local autocorrelation. To find this factor, let us define a complex function S_{pq} by multiplying the above equation with the conjugate of the A_{c_pq},

$$S_{pq} = A'_{c\_pq} A^{*}_{c\_pq} = e^{i(k\check{x} + k\check{y})} \left|A_{c\_pq}\right|^2 \qquad (7.12)$$

Since S_{pq} is a complex function, it can also be written as

$$S_{pq} = M_{s\_pq} e^{i\emptyset_{s\_pq}} \qquad (7.13)$$

Where M_{s_pq} indicates the amplitude part and $\emptyset_{s\_pq}$ represents the phase part of the S_{pq}. Using equations (7.12) and (7.13), these two terms can be extracted by calculating modulus and phase of the function S_{pq} and can be written as below

$$M_{s\_pq} = \mathrm{mod}\left(S_{pq}\right) = \left|A_{c\_pq}\right|^2 \qquad (7.14)$$

and

$$\emptyset_{s\_pq} = \mathrm{phase}\left(S_{pq}\right) = k\check{x} + k\check{y} \qquad (7.15)$$

Using the above equation, linear deformation introduced in the sub-region of the object is retrieved by calculating the $\emptyset_{s\_pq}$. Displacement vector or shift

corresponds to this linear deformation is measured by defining another function F_{pq} as below

$$F_{pq} = 1.\, e^{i\emptyset_{s\_pq}} \tag{7.16}$$

The above function is similar to the expression S_{pq} given in equation (7.13), however, since M_{s_pq} carries no useful information; this term is replaced with the uniform amplitude of unity, leading to the expression mentioned in the equation (7.16). According to equation (7.15), $\emptyset_{s\_pq}$ depends linearly on $\check{x}$ and $\check{y}$ coordinates, it represents a line equation, thus, F_{pq} expresses a linear or a tilt introduced in the sub-region. Since the function F_{pq} is purely a phase function and it carries the linear deformation or the tilt information, the two-dimensional Fourier transform operation on this function ideally leads to a Dirac delta function ($DDF_{.pq}$); a 2D image which is having a maximum intensity at a single point located at a shifted position from the origin of the respective sub-image, given as,

$$DDF_{.pq} = \delta_{pq}(x' - x'_s, , y' - y'_s) = F.T.(F_{pq}) \tag{7.17}$$

The coordinates where Dirac delta function $\delta_{pq}(x' - x'_s, , y' - y'_s)$ is defined, represented by (x', y'). This function is having the maximum intensity concentrated at the single point located at (x'_s, y'_s) away from the center point or origin of the corresponding sub-image. Further, the shift from the origin or displacement vector $Dis._{pq}$ is calculated by finding the location of the pixel containing the maximum amplitude and subtracting the coordinates of the location of the origin of the respective sub-image.

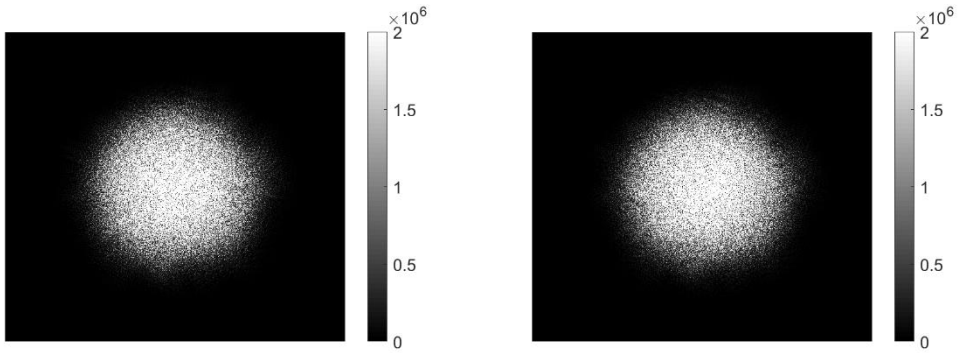

(a) (b)

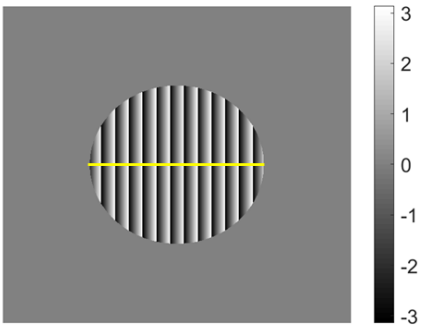
3
2
1
0
-1
-2
-3

(c)

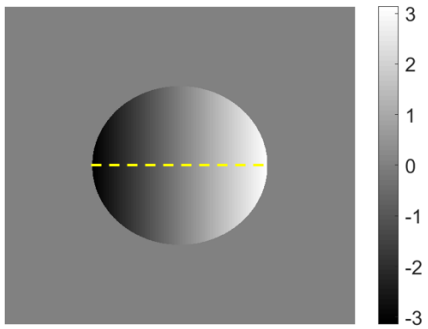
3
2
1
0
-1
-2
-3

(d)

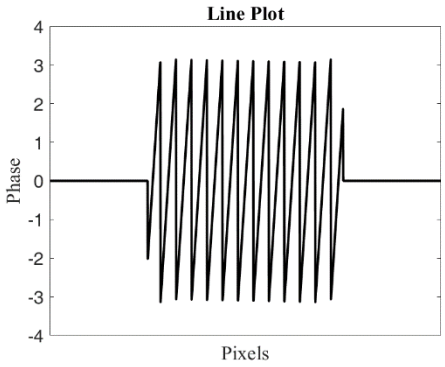
Line Plot
Phase
Pixels
4
3
2
1
0
-1
-2
-3
-4

(e)

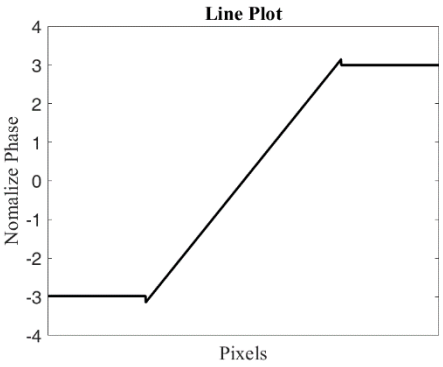
Line Plot
Nomalize Phase
Pixels
4
3
2
1
0
-1
-2
-3
-4

(f)

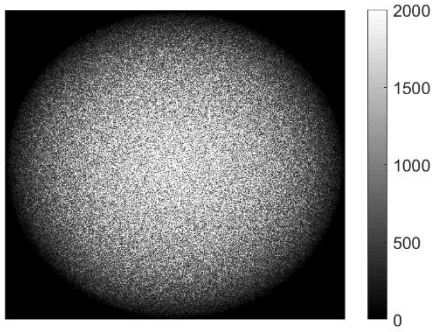
2000
1500
1000
500
0

(g)

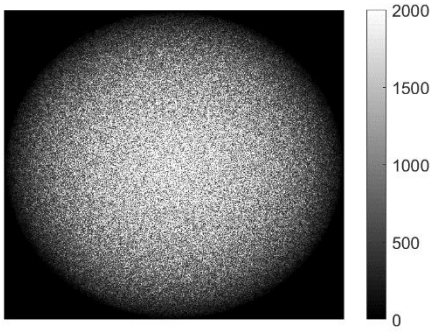
2000
1500
1000
500
0

(h)

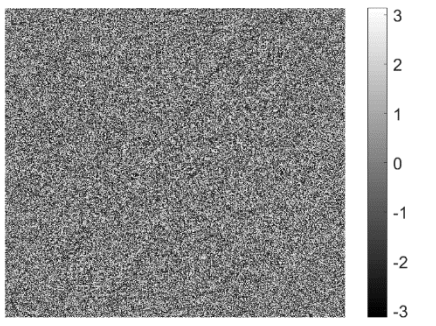
3
2
1
0
-1
-2
-3

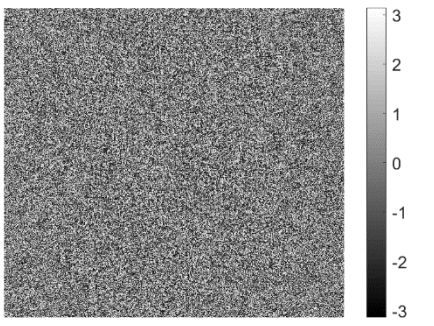
3
2
1
0
-1
-2
-3

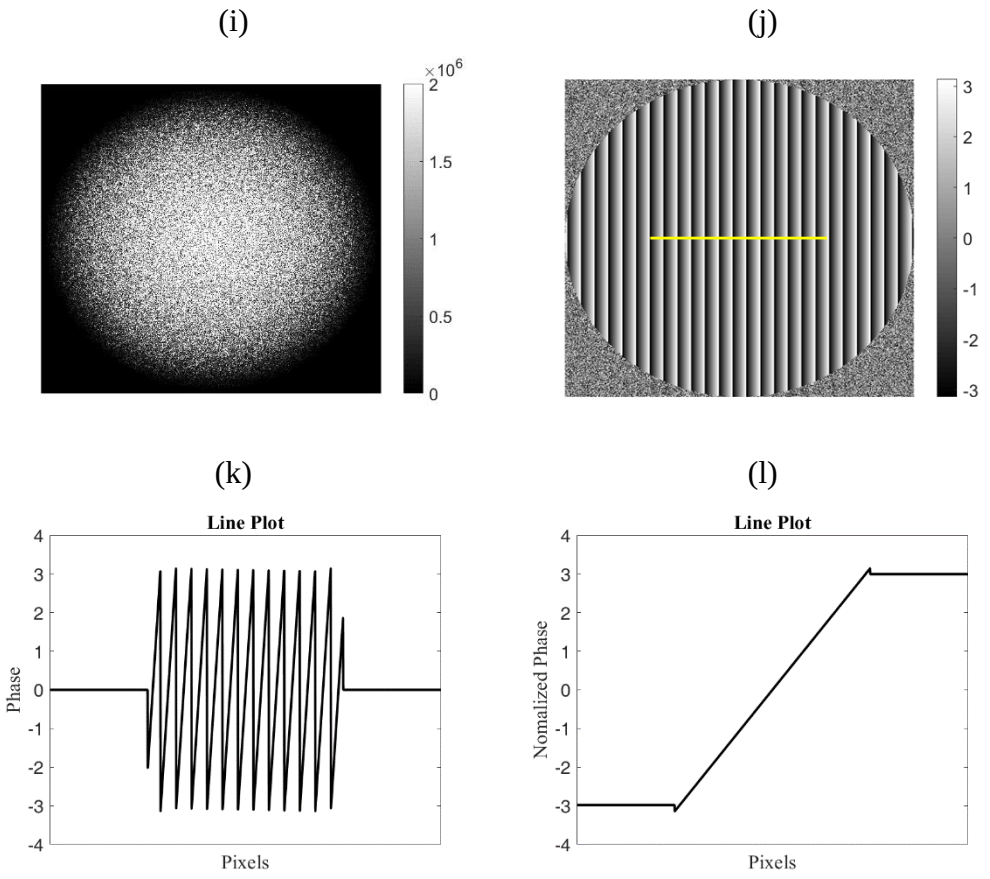

Figure 7.3: (a) and (b) sub-images i.e., I_{pq} and I'_{pq}, (c) linear deformation introduced in the sub-region of the object behind a particular cell, (d) unwrap and normalized version of the (c) shows the linear deformation or tilt, (e) and (f) show the respective line plots plotted with respect to the solid and dotted lines shown in (c) and (d) respectively, (g) and (h) amplitudes of the local autocorrelations obtained computationally from the sub-images (a) and (b), (i) and (j) show the corresponding phases of the local autocorrelations, (k) and (l) amplitude M_{s_pq} and phase $\emptyset_{s\_pq}$ information of the function S_{pq}, (m) and (n) wrapped, and unwrapped and normalized line plots; with respect to the line indicated in (l).

In this section, a simulation study is presented in which a part of object surface or a sub-region of the object undergoes a linear deformation. For this particular sub-region, the respective sub-images before and after the deformation i.e., I_{pq} and I'_{pq} are displayed in figures 7.3 (a) and (b). The deformation introduced which is

wrapped between –π to π is shown in figure 7.3 (c) and unwrapped and normalized between –π to π version of it is shown in figure 7.3 (d). The line plots corresponding to the solid and dotted lines shown in aforementioned figures are plotted in figures 7.3 (e) and (f). From figure 7.3 (f), one can clearly see that introduced deformation is linear. Respective local autocorrelations A_{c_pq} and A'_{c_pq} are obtained computationally using two dimensional Fourier transform operation in MATLAB. Amplitudes of the local autocorrelations are displayed in figures 7.3 (g) and (h) and corresponding phases are shown in figures 7.3 (i) and (j). The amplitude M_{s_pq} and phase $\emptyset_{s\_pq}$ information of the function S_{pq}, are calculated and are shown in figures 7.3 (k) and (l) respectively. It is clear that $\emptyset_{s\_pq}$ shown in the figure 7.3 (l), contains the linear deformation information which matches with the deformation introduced as shown in figure 7.3 (c). The line plots are plotted and shown in figure 7.3 (m) and (n), these two are also matching with the ones shown in figures 7.3 (e) and (f).

Note, intensity of the object in undeformed case (reference pattern) is needed to be recorded only once. This intensity pattern then can be used with the single intensity distribution recorded at any point of time during the loading. However, we must keep in mind that while recording intensities for the undeformed and deformed object, external vibration should be kept minimum. Besides, any additional changes except for the deformation should be kept minimum e.g., laser and ambient light fluctuations, movements of optical components used in the setup. Hence, under such conditions, once we have the reference intensity pattern, we only need to record a single intensity pattern of the object in the deformed condition. Thus, our method is suitable for static as well as for real-time deformation measurements under the conditions mentioned before. For comparison reference image needs to be recorded. However, it does not mean the reference image should be taken without the deformation. Even an image captured during the deformation can be considered as a reference image, then with respect to that reference image further image recorded during the loading can be used for the comparison.

7.4 Simulation results without and with the mask

For the simulation, the size of all the images is chosen 2000×2000 pixels^2, whereas the pixel pitch is considered to be 8 μm. The mask contains 10×10 cells, thus

mask divides the object's image into 10×10 sub-regions. In the same way, the recorded intensities of the camera are also divided equally into 10×10 sub-images with each sub-image spanning an area of 200×200 pixels^2. The radius of the aperture used inside the telecentric geometry is considered to be 5 *mm*. Focal length for the simulation is chosen to be 200 *mm*. According to equation (7.3), a defocused distance 16 *mm* is calculated.

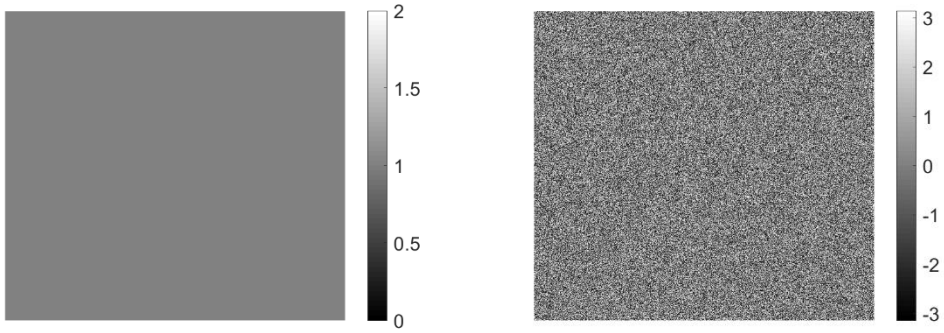

(a) (b)

Figure 7.4: (a) and (b) amplitude and phase of the object used for the simulation. The value of amplitude is chosen unity throughout the entire region, and the value of the phase is varying spatially between –π to π randomly.

To mimic the rough surface, an object having a uniform amplitude and random phase distribution is considered for our simulation, as shown in figures 7.4 (a) and (b), respectively.

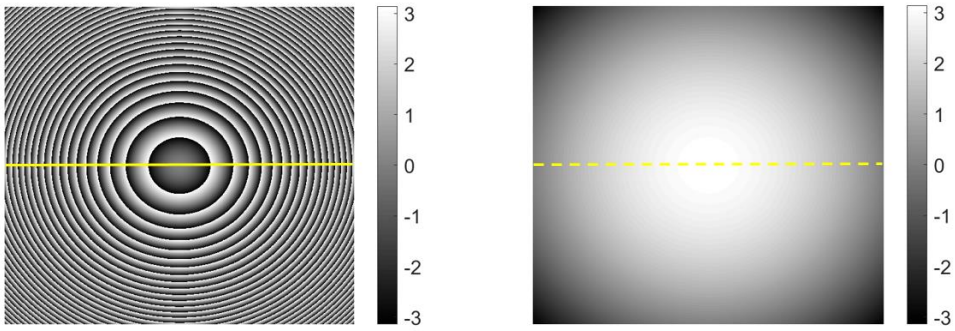

(a) Wrapped

(b) Unwrapped and normalized between –π to π

Figure 7.5: Deformation introduced in the phase part of the object.

Linear function can be expressed as $\emptyset = k\check{x}^1 + k\check{y}^1$,while non-linear function can be written as $\emptyset = k\check{x}^n + k\check{y}^m$ where $n > 1$ and $m > 1$. To mimic the bulging effect due to the loading, a spherical deformation i.e., $\emptyset = k\check{x}^2 + k\check{y}^2$ is introduced in the phase term of the object, as shown in figure 7.5.

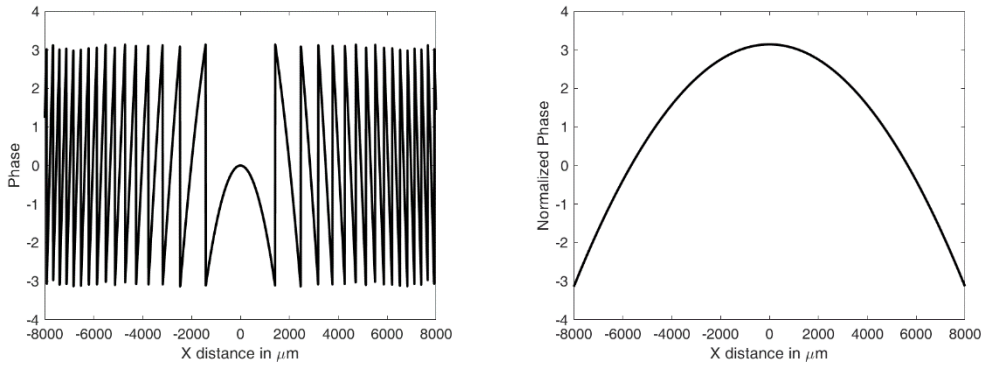

(a) (b)

Figure 7.6: (a) and (b) line plots are plotted with respect to the solid and dotted lines shown in figures 7.5 (a) and (b) respectively.

After the deformation amplitude of the object remains the same, while phase of the object deformed according to the deformation introduced. Using the setup shown in figure 7.1 (a), to see the advantage of our technique where mask is used with the already esisting technique e.g., speckle correlation technique where mask is absent, two sets of data are simulated without and with the mask.

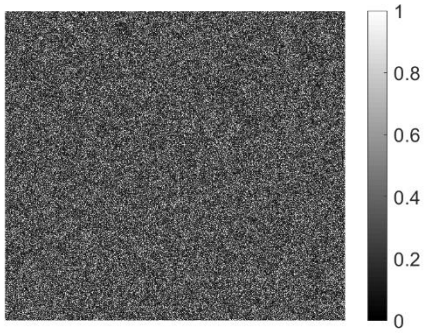

(a) Intensity I for the undeformed object

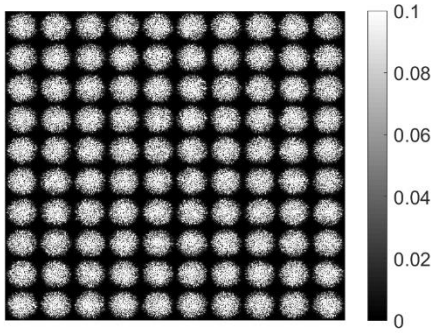

(a) Intensity I for the undeformed object

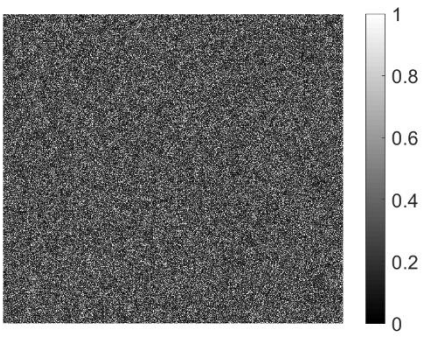

(b) Intensity I' for the deformed object

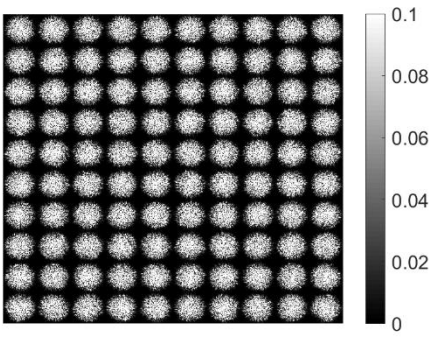

(b) Intensity I' for the deformed object

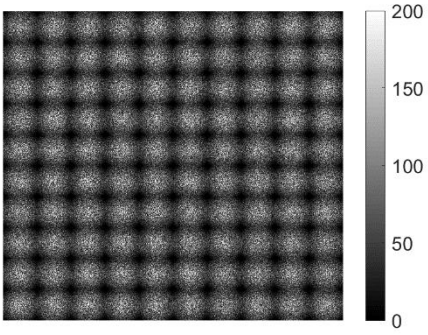

(c) Amplitudes of the local autocorrelations calculated across all the sub-images for I

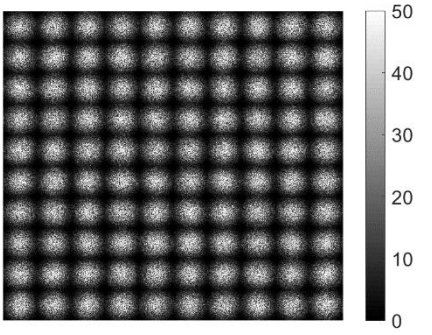

(c) Amplitudes of the local autocorrelations calculated across all the sub-images for I

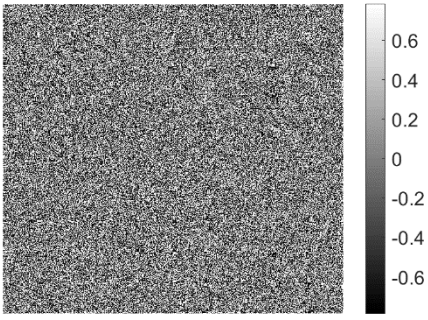

(d) Phases of the local autocorrelations calculated across all the sub-images for I

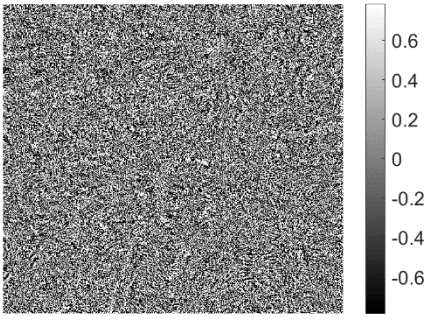

(d) Phases of the local autocorrelations calculated across all the sub-images for I

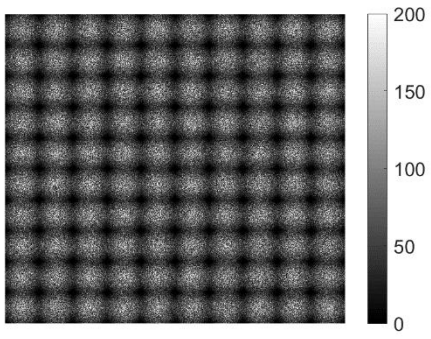

(e) Amplitudes of the local autocorrelations calculated across all the sub-images for I'

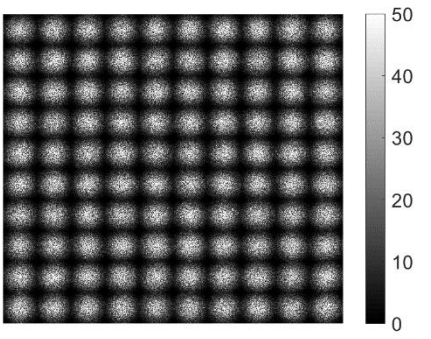

(e) Amplitudes of the local autocorrelations calculated across all the sub-images for I'

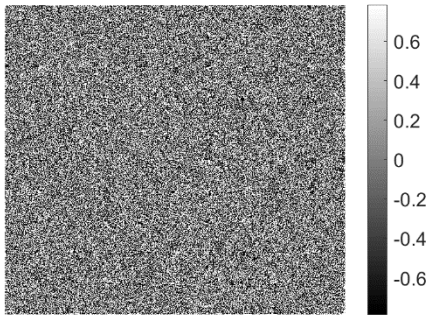

(f) Phases of the local autocorrelations calculated across all the sub-images for I'

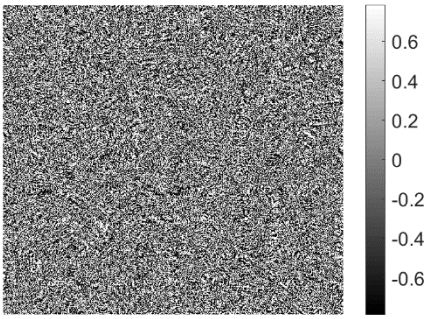

(f) Phases of the local autocorrelations calculated across all the sub-images for I'

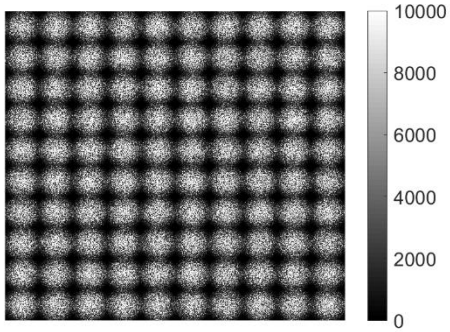

(g) Amplitudes M_{s_pq} calculated across all the sub-images

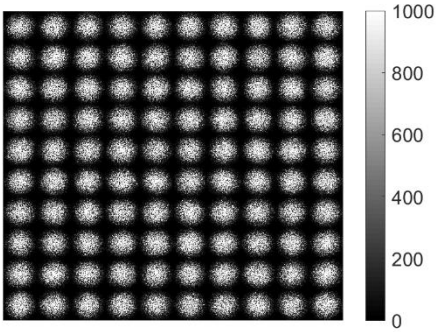

(g) Amplitudes M_{s_pq} calculated across all the sub-images

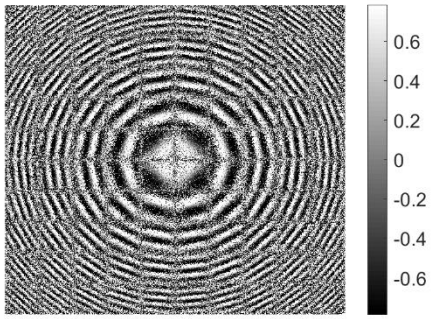

(h) Phases $\emptyset_{s\_pq}$ calculated across all the sub-images

Figure 7.7: Simulation without the mask

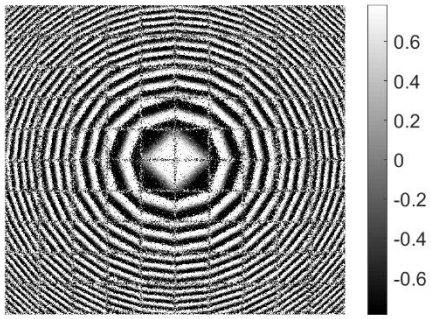

(h) Phases $\emptyset_{s\_pq}$ calculated across all the sub-images

Figure 7.8: Simulation with the mask

A camera is placed at the defocused distance away from the image of the object. The intensity I and I' are recorded at this distance, before and after the deformation as shown in figures 7.7 (a) and (b) respectively. From these figures it is clear that due to the absence of the mask, fields scattered from the different parts of the object's image are overlapped with one another in the camera plane. In this case, we can divide the screen of the camera into any number of partitions since the mask is absent; however, to make a comparison similar to one where mask is used, to process the recoded intensities, we divide these intensities into 10×10 sub-images. For a sub-image, local autocorrelations A_{c_pq} and A'_{c_pq} are obtained using the method proposed in the derivation section for the undeformed and deformed case respectively, where p, q show the location of the sub-image located at p^{th} row and q^{th} column. And this process is repeated for all sub-images. Amplitudes and phases of the local autocorrelations A_{c_pq} are calculated across all the sub-images and placed according to their location located at p^{th} row and q^{th} column and are shown in figure 7.7 (c) and (d). Similarly, amplitudes and phases of the local autocorrelations A'_{c_pq} are measured and are shown in figures 7.7 (e) and (f). Amplitudes M_{s_pq} and phases $\emptyset_{s\_pq}$ of the local functions S_{pq} are calculated for all the sub-images and are shown in figures 7.7 (g) and (h). Figure 7.7 (h), is quite similar to the deformation introduced in the object shown in figure 7.5 (a). More precisely, phases $\emptyset_{s\_pq}$, measured across all the sub-images capture the tilts

information present across all the sub-images. In a similar fashion, keeping all the conditions same, another set of data is simulated with the presence of the mask. The respective functions and their respective distributions are shown in figure 7.8. The phases $\emptyset_{s\_pq}$ calculated across all the sub-images shown in figure 7.8 (h), show a discrete version of the deformation induced in the object due to the loading. From figure 7.8 (h), one can estimate the deformation shape discretely, which is spherical in this case, and is obtained in lesser computational steps as compared to DIC method. Figure 7.8 (h), as compared to the pattern shown in figure 7.7 (h), has sharp features of the deformation, therefore, it has high signal to noise (SNR) ratio. The high SNR, in the result shown in the figure 7.8 (h) occurs due to the presence of the mask, since the fields scattered from the sub-regions propagate till the camera plane and confine within the respective sub-images, do not overlap with one another as shown in the figures 7.8 (a) and (b), leading to the better reconstruction i.e., figure 7.8 (h) as compared to the result obtained with speckle correlation technique as shown in figure 7.7 (h).

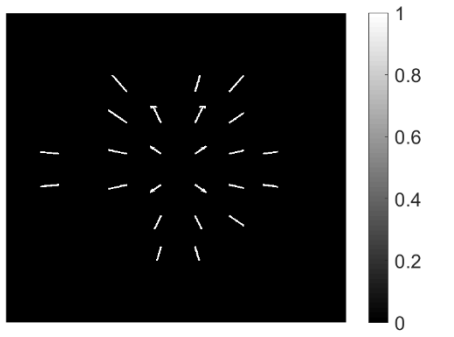

(a) Displacement vectors

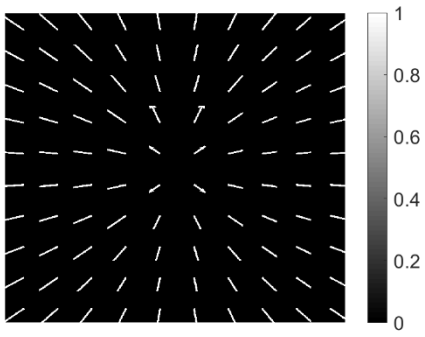

(a) Displacement vectors

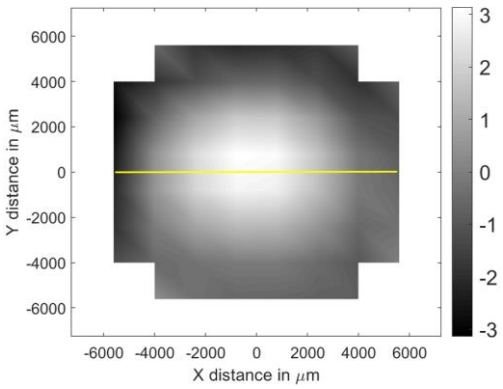

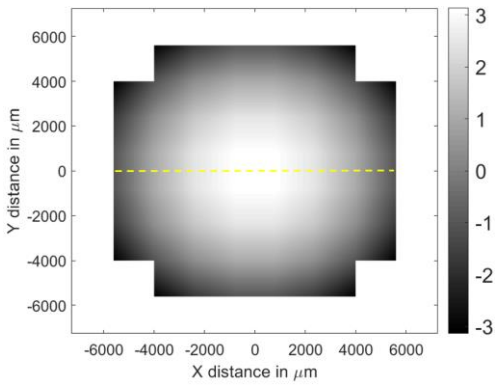

(b) full-field non-linear deformation obtained from the displacement vectors using modal wavefront reconstruction method.

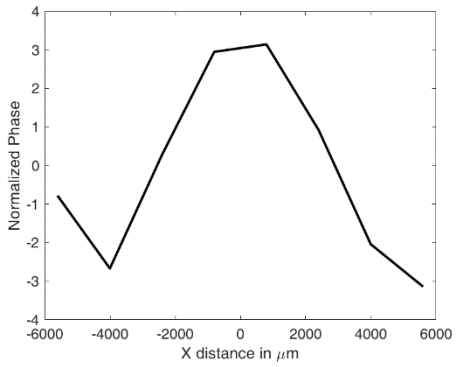

(c) line plot with respect to the solid line shown in the (b)

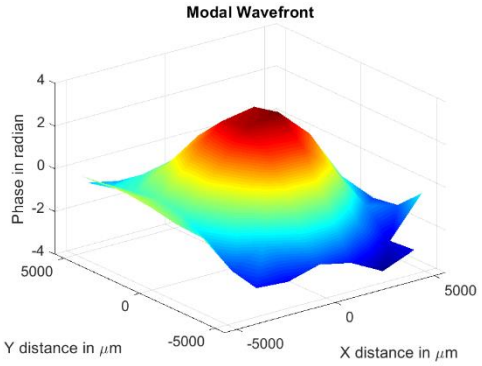

(d) 3D full-field non-linear deformation obtained from the displacement vectors using modal wavefront reconstruction method.

Figure 7.9: Simulation result without the mask

(b) full-field non-linear deformation obtained from the displacement vectors using modal wavefront reconstruction method.

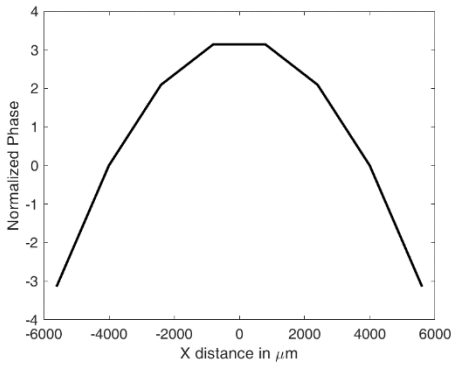

(c) line plot with respect to the dotted line shown in the (b)

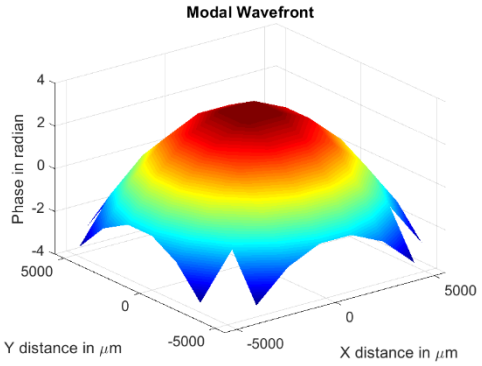

(d) 3D full-field non-linear deformation obtained from the displacement vectors using modal wavefront reconstruction method.

Figure 7.10: Simulation result with the mask

From the figures 7.7 (h) and 7.8 (h), displacement vectors are obtained as discussed in the derivation section and are shown in figures 7.9 (a) and 7.10 (a). It is clear from figure 7.9 (a) that without the mask signal to noise ratio is less, and displacement vectors for the locations where large tilts or linear deformations occurred, such as those located far from the center are hard to measure due to the

poor SNR. Lastly to reconstruct the full-field deformation for quantitative analysis a modal wavefront reconstruction method [53-58] is adopted. Utilizing the figures 7.9 (a) and 7.10 (a), the corresponding reconstructions are shown in figures 7.9 (b) and 7.10 (b). Line plots are plotted in figures 7.9 (c) and 7.10 (c) with respect to the solid and dotted lines depicted in figures 7.9 (b) and 7.10 (b). 3D full-field non-linear deformation obtained from the displacement vectors using the modal wavefront reconstruction method for two cases are shown in figures 7.9 (d) and 7.10 (d). From these two cases, it can be concluded that when the mask is present in the setup, deformation can be calculated more accurately compared to when the mask is absent.

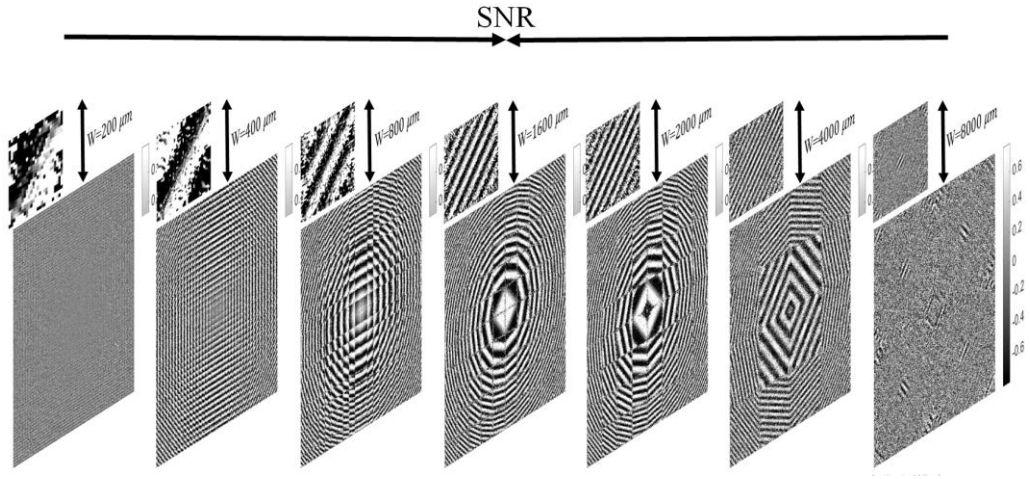

(a)

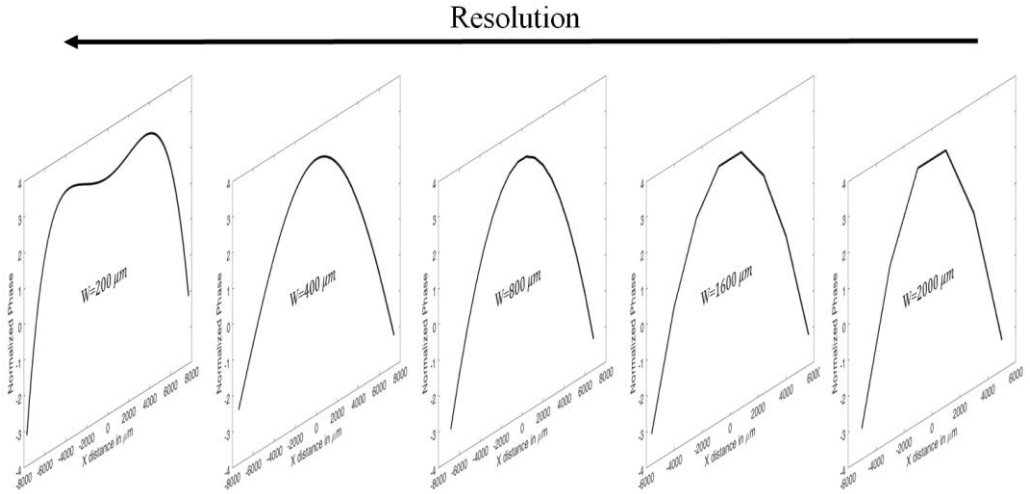

(b)

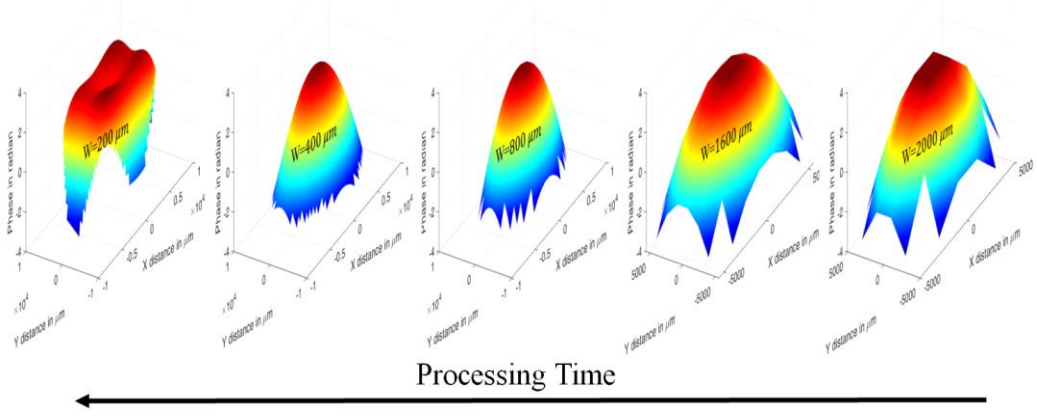

(c)

Figure 7.11: Effect with respect to the size of the sub-image on signal to noise ratio, resolution, and processing time (a), (b) and (c) respectively.

Note that for an intensity, by increasing the number of sub-images one can increase the spatial resolution; however, in order to increase the number of sub-images, the size of sub-image should be decreased, which leads to the low single to noise ratio. Therefore, in order to get the high single to noise ratio and good spatial resolution, one has to optimize the number of sub-images and size of the sub-image for the particular camera. Since without the mask we can select size of the sub-images according to our need as mentioned earlier. Without the mask, a simulation study is presented here to see the effect of changing the size of the sub-image in the following steps $w = 200, 400, 800, 1600, 2000, 4000, 8000\ \mu m$ on the signal to noise ratio as shown in figures 7.11 (a). From figure 7.11 (a), one can see that SNR is very poor when sub-image size is high e.g., $w = 4000\ \mu m$ and $w = 8000\ \mu m$, to reconstruct the deformation information. Therefore, last two steps are removed and for the remaining steps the resolution and processing time are measured. The resolution and processing time increase when decreasing the sub-image size as shown in figures 7.11 (b) and (c) for obvious reason. To optimize these parameters we need to select a sub-image size, which provides high SNR to reconstruct the object deformation, having acceptable resolution in lesser amount of time. According to the figure 7.11, one can conclude that any value of w can be chosen within a range from $w = 400\ \mu m$ and $w = 1600\ \mu m$ for a given image size of $w = 16000\ \mu m$.

7.5 Experiment and results

For the experiment, fabricating the mask where the openings are located equally spaced from each other, and all openings have identical radius is difficult, due to the imperfections in the fabrication process. In this situation, knowing the respective sub-image location at the camera is not an easy task. Therefore, once the mask is fabricated, at least one time, we need to find all the sub-images locations for this particular mask before performing the experiment as discussed before.

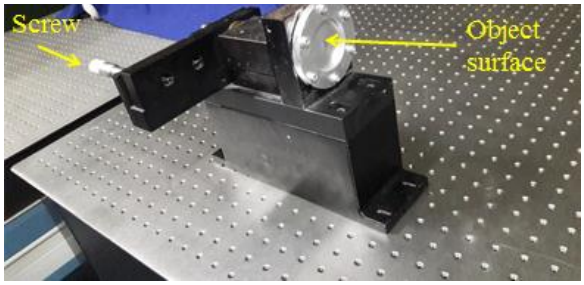

Figure 7.12: Deformable object

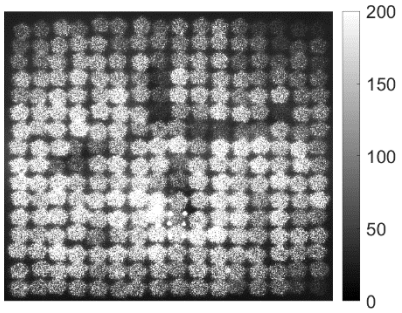

(a) Intensity I for the undeformed object

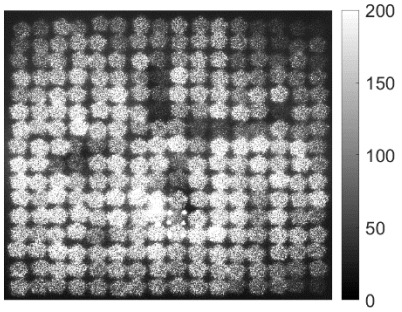

(b) Intensity I' for the deformed object

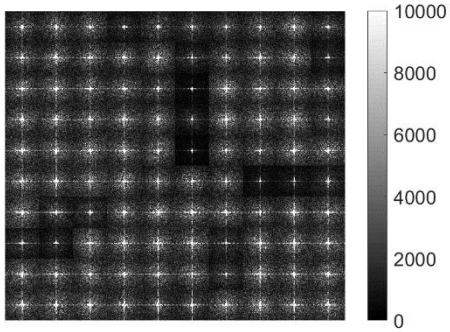

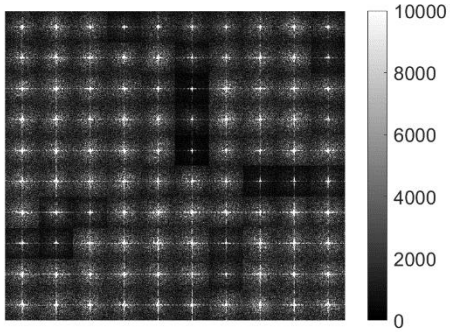

(c) Amplitudes of the local autocorrelations calculated across all the sub-images for I

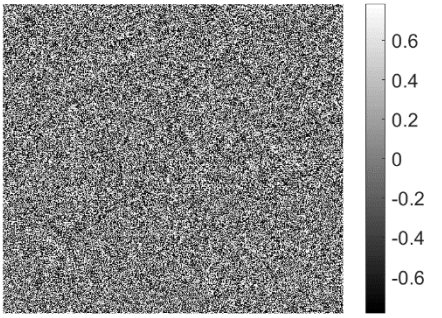

(d) Amplitudes of the local autocorrelations calculated across all the sub-images for I'

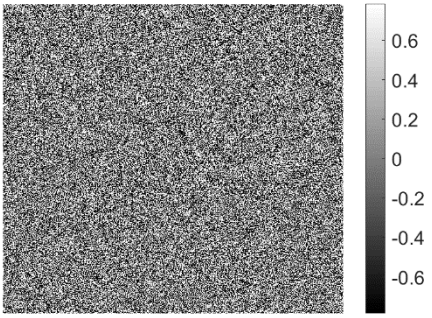

(e) Phases of the local autocorrelations calculated across all the sub-images for I

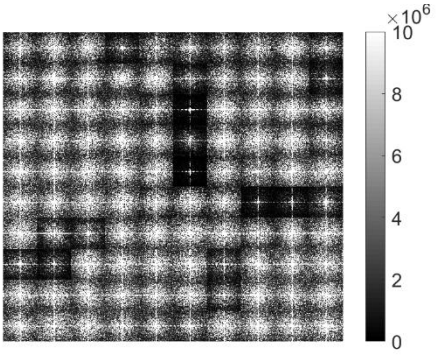

(f) Phases of the local autocorrelations calculated across all the sub-images for I'

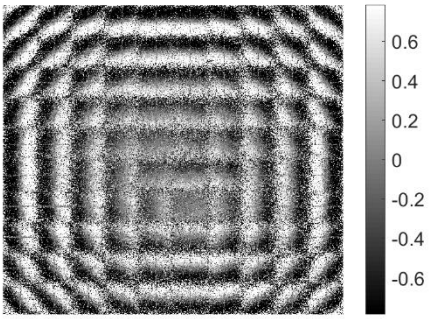

(g) Amplitudes M_{s_pq} calculated across all the sub-images

(h) Phases $\emptyset_{s\_pq}$ calculated across all the sub-images

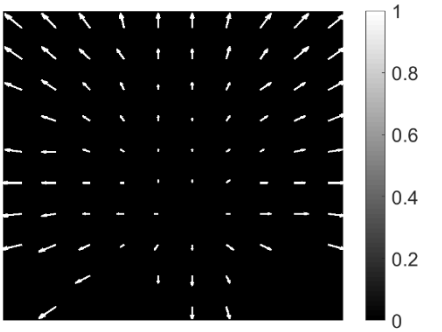

(i) Displacement vectors calculated across all the sub-images

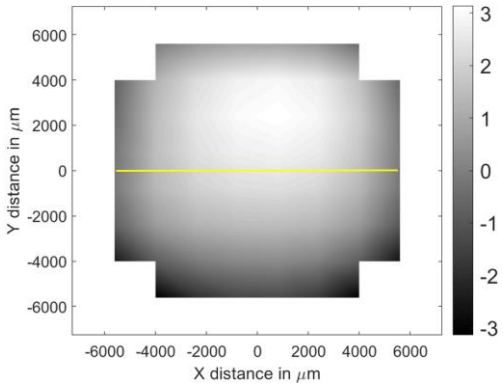

(j) full-field non-linear deformation obtained from the displacement

vectors using modal wavefront reconstruction method.

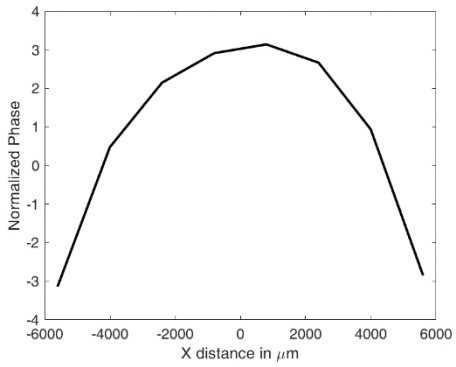

(k) line plot for the solid line indicated in (j)

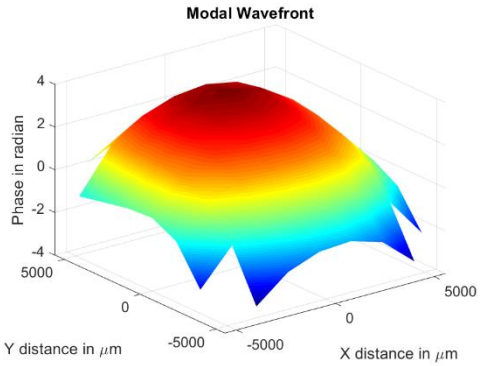

(l) 3D full-field non-linear deformation obtained from the displacement vectors using modal wavefront reconstruction method

Figure 7.13: Experimental results with the mask

An experiment is performed for measuring the deformation of the object's surface by introducing mechanical loading. An object having a rough surface is used for the experiment, as shown in figure 7.12. The nonlinear deformation or a bulging effect is introduced in the object surface by rotating the screw. This deformable object is illuminated with a single coherent laser light beam. An experimental setup similar to the setup shown in figure 7.1 (a) is adopted here. And recordings have been captured by placing a fabricated mask. The intensity patterns are recorded before and after the deformation of the object surface and are shown in figures 7.13 (a) and (b), respectively. First locations of all the sub-images are calculated and then across all the sub-images, local autocorrelations are obtained for undeformed and deformed object. For these two cases, amplitudes of the local autocorrelations are calculated across all, and are shown in figures 7.13 (c) and (d). Similarly, phases of the local autocorrelations are calculated, and are shown in figures 7.13 (e) and (f). Amplitudes M_{s_pq} and phases $\emptyset_{s\_pq}$ are calculated and are shown in figures 7.13 (g) and (h). Each sub-image of figure 7.13 (h) contains the tilt information present within the sub-region and across all the sub-images, figure 7.13 (h), depicts discrete version of spherical deformation. Displacement vectors are obtained across all and shown in figure 7.13 (i). Utilizing the displacement vectors and employing the

modal method, full-field deformation is obtained for the quantitative purpose as shown in figure 7.13 (j). Line plot and 3D full-field non-linear deformation are shown in figures 7.13 (k) and (l), respectively.

7.6 Conclusion

We have successfully developed a method to reconstruct the deformation of the object surface from a single far-field intensity recorded after the loading and comparing it with the reference intensity pattern recorded before the loading. To prove the concept, a detailed theoretical derivation has been formalized. Further, simulation has been conducted without and with the mask. Furthermore, experiment is performed with the presence of the mask. From the simulation results, we can conclude that when the mask is present in the setup high signal to ratio is achieved compared to when the mask is absent. Apart from this, our method provides discrete version of the full field deformation in fewer numerical operations by measuring $\emptyset_{s_{pq}}$ across all the sub-images that gives the discrete version of the full field deformation that will be beneficial knowing the shape of the deformation. Moreover, with our method the 3D full-field deformation is also obtained for the quantitative purpose.

Conclusions and Future Scope

- **Conclusions**

Several non-destructive optical methods for recording and reconstructing the complex object i.e., amplitude and phase information are proposed and discussed in this thesis. How these methods can be utilized for various applications e.g., volumetric holographic data storage and reconstruction, and deformation measurement of an object which is under mechanical loading condition are also presented. The reconstruction results show the capabilities of the proposed methods over the existing methods. Extensive derivation along with the simulation and experiments is performed for supporting these methods.

In the first chapter, fundamental problem associated with the conventional camera is discussed and how to overcome this by using the existing techniques is also examined, in addition drawbacks of the existing techniques are also pointed out. To realize such techniques mathematically along with the parameters associated with the techniques is also discussed. The image format used throughout the thesis is also specified in the last section of the first chapter.

A novel method is discussed in chapter second, for reconstructing the object information without the twin-image problem that occur sometimes in the phase retrieval iterative algorithm. It is well known that the twin-image problem is severe in the case of the asymmetric object, and in second chapter, asymmetry of the object is used to overcome the aforementioned problem.

In the third chapter, a modified PRA approach is developed for general objects. The proposed method is suitable for all kinds of objects i.e., asymmetric or symmetric. In this PRA method, an edge point referencing approach is used to create asymmetry in the beam; therefore, irrespective of the objects having asymmetry or

not, this method ensures twin-image free reconstruction with fast convergence. Owing to the fact of using a portion from the autocorrelation, the algorithm produces a unique output; therefore, how this method can further be utilized to measure the deformation is also discussed.

An iterative PRA technique is proposed in the fourth chapter and its application in volumetric holographic data storage and reconstruction are presented. In this case, a special object is created by illuminating the optically recorded Fourier hologram. This special object contains object-twin pair and using a conventional camera its far-field intensity is recorded. From the intensity pattern, one can obtain promising results without structuring the illumination beam or utilizing asymmetry of the object.

In the fifth chapter, a photograph assisted iterative approach is discussed, simulation results and a novel optical setup are also presented. In this technique, the far-field intensity pattern along with the photograph of the object is captured on a single screen of the camera side by side. The proposed method performs well for all kinds of objects i.e., symmetric and asymmetric. Due to the single-shot in nature, this method can be applied for real-time dynamic situations also. Further, it can be performed in the case of plane beam illumination; hence structuring the beam is also not required.

In the sixth chapter, a novel non-iterative method is proposed and demonstrated experimentally to retrieve the 2D as well as the 3D complex object from its autocorrelation. The method utilizes edge point referencing; therefore, it does not require any separate reference to record the hologram. The proposed setup is a common path and robust to the external vibrations. The proposed method is also examined in an application for measuring the real-time deformation.

In the last chapter, the reconstruction of the deformation of the object surface from the far-field intensity patterns recorded before and after the loading has been successfully demonstrated. The proposed method provides discrete version as well as quantitative reconstruction. From the discrete version, one can roughly estimate the shape of the deformation in fewer calculations, while for the analytical purpose, one can utilize the quantitative reconstruction.

- **Future scope**

There are areas where the proposed methods can be utilized; however, those areas are not examined in the thesis which are as follows

1. In most of the thesis chapters, one needs to record a far-field intensity at the Fourier plane, and to obtain such a pattern, one needs to place a camera at the far-field, or a Fourier transforming optical lens should be placed before the camera. Besides, the concepts of most of the proposed methods are derived for the far-field. In an application such as microscopic imaging, generally, a camera is placed very close to the object, therefore, in such a scenario, it is difficult to obtain the far-field intensity pattern or to place a Fourier transforming lens before the camera. Thus the effect of using the proposed techniques in the near field should be explored and examined.
2. In some methods, edge point referencing scheme is employed in which an additional beam is used along with a plane beam for illuminating the object. To generate such beams, the proposed method employs an optical setup that contains several optical components. However, one can obtain the same by fabricating an optical element e.g., filter, or utilizing a spatial light modulator that structures the optical beam identical to the edge point referencing. By utilizing SLM or filter one can make the optical setup more compact and robust; however, experimentally, it is not verified.
3. In some methods, only simulations are provided; to further support the theory experiments should also be conducted.
4. Retrieving the complex object information from the far-field intensity has several advantages in various applications other than the applications mentioned in the thesis; however, those applications are not explored in this thesis.

Appendix A

We observe that object autocorrelation obtained from the far-field intensity pattern of asymmetric object contains the object features. This fact is utilized here in the phase retrieval algorithm (PRA) to remove the twin image problem.

A.1 Introduction

Reconstruction results of the PRA are suffered by twin image or inverted image problem, in addition, twin image problem is severe when object is asymmetric. Here a new PRA method is presented and discussed, in which one can use the asymmetry of the object as a tool to remove the twin image problem from the reconstruction result obtained from the single-shot measurement. The basic idea of the proposed technique is described below.

A.2 Principle

Consider an object which is illuminated with a coherent beam of radius r_o , smaller than the object dimension. The desired object g(r) (confined within the illumination) can be treated as a composition of several points. Two points of the object located at the peripheries of the desired object can be written separately as follows,

$$g(r)=f(r)+c_1\delta(r-r_o)+c_2\delta(r+r_o). \quad (A.1)$$

Where r=(x,y) is the position vector at the object plane, f(r) represents the remaining part of the object. Object periphery points are denoted by Dirac delta functions as $c_1\delta(r-r_o)$ and $c_2\delta(r+r_o)$ with complex amplitudes c_1 and c_2. These points are located at diagonally opposite locations near the boundary of the desired object at a distance r_o from the center. The diffraction pattern of the object g(r) at the Fourier plane can be obtained by simply taking its Fourier transform as,

$$G(k)=F(k)+c_1\exp(-ik.r_o)+c_2\exp(ik.r_o). \quad (A.2)$$

Where G(k), F(k) , k, and "." represent the diffraction pattern at Fourier plane, Fourier transform of f(r), wave vector, and the dot product, respectively. Let us suppose a camera is placed at the Fourier plane to record the intensity of the diffraction pattern, which can be written as

$$I=|G(k)|^2. \tag{A.3}$$

The numerically inverse Fourier transform of the diffraction pattern can be described as,

$$\begin{aligned}\check{g}(r) = g(r)\otimes g^*(-r) = f(r)\otimes f^*(-r) + (|c_1|^2 + |c_2|^2)\otimes\delta(0) + \\ c_2c_1^*\otimes\delta(r + 2r_o) + c_1c_2^*\otimes\delta(r - 2r_o) + \\ (f(r)c_1^* + f^*(-r)c_2)\otimes\delta(r + r_o) + (f(r)c_2^* + f^*(-r)c_1)\otimes\delta(r - r_o).\end{aligned} \tag{A.4}$$

Where '$*$' denotes the complex conjugate and $\check{g}(r)$ represents the object autocorrelation of the object $g(r)$, and "$\otimes$" represents the convolution operation. Since object autocorrelation is a convolution between an object and its twin $g^*(-r)$, it spans in a circular region of radius $2r_o$. For an unknown object, from the size of autocorrelation, object support information (in this case circular aperture of radius r_o) which is exactly half the size of the object autocorrelation, can be measured. Additionally, for the chosen points located at the edges, the last two terms (5^{th} and 6^{th}) in equation (A.4), are completely separated from each other. Therefore, the region corresponding to 5^{th} term can easily be cropped out using the measured object support from the object autocorrelation and can be written as follow,

$$5^{th}\text{ term} \propto (f(r)c_1^* + f^*(-r)c_2). \tag{A.5}$$

For asymmetric object, considered a case where edge points have different amplitudes i.e. $|c_1| \neq |c_2|$, by following equation (A.5), it leads to a different proportion of object $f(r)$ over its twin $f^*(-r)$ in the cropped region. If one uses this cropped portion in any existing PRA algorithms as an initial guess, depending on the strength of the complex amplitudes c_1 and c_2 , either PRA converges to upright ($|c_1| \gg |c_2|$) or the twin ($|c_1| \ll |c_2|$) but never both. Note for the sake of the simplicity of the above derivation, two single points near the edges are taken, which are denoted by $c_1\delta(r - r_o)$ and $c_2\delta(r + r_o)$; however, to check the asymmetry of

the object more precisely, comparison between these single points may not be sufficient, one should take collection of points of the object near the periphery as discussed in chapter 2.

A.3 Simulation, results and discussion

Simulation is carried out using a complex object created by patterns of a letter 'M' and a uniform distribution as an amplitude and phase information as shown in figures A.1 (a) and (b). The desired object is confined within a circular boundary of 40 pixels as shown in figures A.1 (a) and (b). To show the effect of asymmetry and symmetry of the object on the reconstruction of PRA using hybrid input-output HIO (Appendix D), the amplitude of the object is chosen in such a way that it is asymmetric with respect to the x-axis viz top portion is different from bottom part i.e. $|c_3| \neq |c_4|$. Additionally, about the y-axis, the object is symmetric specifically left portion is the mirror image of the right portion i.e., $|c_1| \approx |c_2|$.

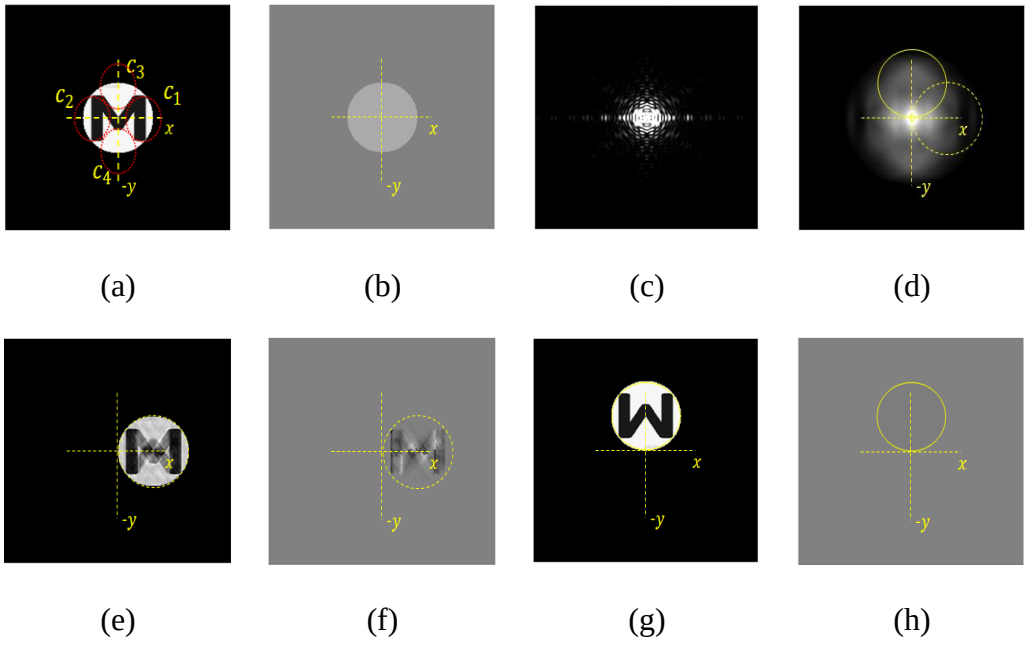

(a) (b) (c) (d)

(e) (f) (g) (h)

Figure A.1: Patterns of (a) Letter 'M' and (b) uniform distribution, show the object amplitude and phase used in the PRA respectively, collections of points near the peripheries of the desired object are denoted by red color/dotted circled $\boldsymbol{c_1}$, $\boldsymbol{c_2}$, $\boldsymbol{c_3}$ and $\boldsymbol{c_4}$ (c) intensity recorded at the Fourier plane, (d) object autocorrelation, dotted and solid circles show the cropping locations using object support from x and y directions respectively. Reconstructions using a

portion cropped from the autocorrelation displaced by a dotted circle in (d) are shown in (e) and (f) as amplitude and phase, respectively, (g) and (h) show the retrieved amplitude and phase information, for the portion filtered from the autocorrelation using a solid circle as shown in (d). Here images of all the amplitudes and phases are normalized between $[\mathbf{0}, \mathbf{1}]$ and $[-\boldsymbol{\pi}, \boldsymbol{\pi}]$.

The intensity recorded at the Fourier plane is shown in figure A.1 (c). And the object autocorrelation obtained from the intensity pattern is shown in figure A.1 (d). For the letter 'M' as shown in figure A.1 (a), since the left and right portions are almost symmetric i.e. $|c_1| \approx |c_2|$ or collection of points on the left are almost identical as the right within the desired object, filtering from the left or right portion from the object autocorrelation as shown by the dotted circle in figure A.1 (d), produces the twin-image problem as mentioned in the figures A.1 (e) and (f). While filtering from the top or bottom location as shown in by the solid circle in figure A.1 (d), since the object is having asymmetry about x-axis or collection of points on the top of the desired object is having different intensity value than the collection of points of the desired object near the bottom i.e. $|c_3| \neq |c_4|$, the corresponding reconstructed amplitude and phase results are displayed in the figures A.1 (g) and (h) which are free from, twin image problem.

Appendix B

A comparison study is presented here, to show the effect on the reconstruction of the phase retrieval algorithm using random initial guess and a region filtered from the autocorrelation as an initial guess (improved guess). Besides, how one can find object support information from the object autocorrelation is also discussed.

B.1 Introduction

Here a method is proposed in which one should crop a region from the object autocorrelation obtained from the intensity captured at the Fourier plane. This filtered region is used as an initial guess or improved guess in the hybrid input-output HIO-PRA (Appendix D) to remove the twin image problem from the reconstruction. This method provides deterministic output, unlike the non-deterministic output as in the case where random initial guesses are used in the PRA on different trails. In this paper, the effect of the random verses the improved initial guess on the reconstruction of PRA is presented. Apart from this, the effect of the size of object support used in PRA in both cases is also presented.

B.2 Random verses improved initial guess

In addition to the chapter 2, where a complex object is used, to see the effect of asymmetry of the object more effectively, a pure amplitude object is utilized here. To form a pure amplitude object, patterns of a letter ‘M’ and a uniform distribution as an amplitude and phase information as shown in figures B.1 (a) and (b) are employed. The desired complex object is asymmetric with respect to x-axis and confined within a circular boundary of 40 pixels as shown in figures B.1 (a) and (b). The intensity recorded at the Fourier plane is shown in figure B.1 (c). The object autocorrelation obtained from the intensity pattern is shown in figure B.1 (d). For the letter ‘M’ as shown in figure B.1 (a), the object is having asymmetry with

respect to x-axis viz filtering from the top location as shown by the solid circle in figure B.1 (d), results in amplitude and phase reconstructions as displayed in the figures B.1 (e) and (f). These results are unique and deterministic irrespective of the number of times the algorithm runs. Therefore, the error associated with these results for a fix number of iterations remains constant even if one runs the algorithm multiple times. On the other hand, reconstruction using a random initial guess shows the non-deterministic output. The algorithm has been executed multiple times and each time the algorithm initiates with a new random guess. Executing the algorithm multiple times shows the different outputs using random guessess. At some point, algorithm shows the correct reconstruction as shown in figures B.1 (g) and (h), sometimes it shows twin image problem as shown in the figures B.1 (i) and (j) and some other instances it shows the inverted-conjugate as shown in figures B.1 (k) and (l) as amplitude and phase respectively. In conclusion, results obtained employing the random guesses are not unique; each time the algorithm runs, it produces different outputs. Errors in the reconstructions for the object support of 40 pixels, for both the cases, are also plotted as shown in figure B.1 (m), which clearly shows the algorithm uniqueness in the case of improved guess i.e., error remains constant, while non-uniqueness in the case when random initial guesses are utilized.

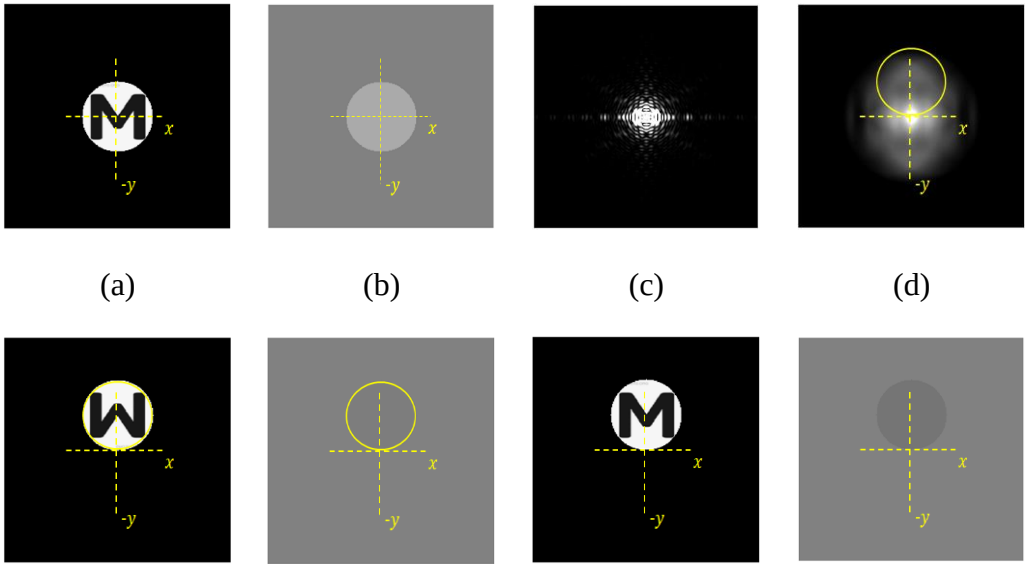

(a) (b) (c) (d)

(e) (f) (g) (h)

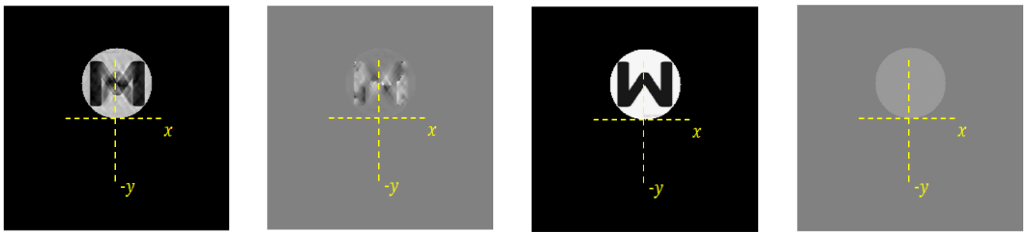

(i) (j) (k) (l)

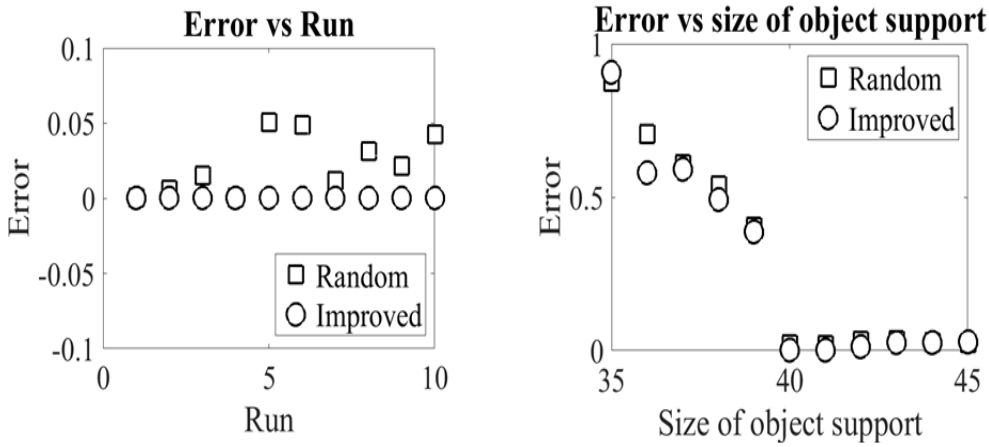

(m) (n)

Figure B.1: Patterns of (a) Letter 'M' and (b) uniform distribution, show the object amplitude and phase used in the PRA respectively, (c) intensity recorded at the Fourier plane, (d) object autocorrelation, a solid circle shows a filtering location using a object support. Reconstructions using the filtered portion from the autocorrelation displaced by the solid circle in (d) are shown in (e) and (f) as amplitude and phase, respectively, (g) and (h), (i) and (j), (k) and (l) show the retrieved amplitudes and phases information, when the random guesses are used as in initial guesses while executing the algorithm multiple times, (m) reconstruction errors in both the cases: using random and improved initial guesses displayed by square and circle symbol, respectively with respect to the execution of the algorithm multiple times, (n) effect of the size of the object support on the errors of the reconstructions. Here all the amplitudes and phases are normalized between $[\mathbf{0}, \mathbf{1}]$ and $[-\boldsymbol{\pi}, \boldsymbol{\pi}]$, respectively.

For the object as mentioned above, the object is enclosed in an aperture of 40 pixels. However, for an unknown object, while detecting the object support from the object

autocorrelation may lead to some error. Therefore, in this section, the errors are plotted for both the aforementioned cases. To plot the errors, in 1st case a fix random initial guess is used, and in 2nd case improved initial guess is used, while changing the size of the radius of the object support from 35 to 45 pixels. The errors are obtained after 100 iterations for both the cases and are plotted in figure B.1 (n). This figure shows that errors grow higher if the size of object support employed in the PRA is less than the actual size (40 pixels). Further, from this figure, when the size of the object support becomes equal to the actual size, errors reduce drastically. Furthermore, once the size of the object support is selected more than the actual size of the object, it influences less on the reconstruction errors for both the cases. Therefore, plotting errors with respect to the size of the object support helps in determining the actual size of the object support.

Appendix C

C.1 Effect of the different shapes of the objects on the autocorrelations

Here the effects have been explored of using various shapes of 'special objects' on the respective autocorrelations obtained from the corrosponding far-field intensities captured at the Fourier plane. These effects are discussed in cases from 1 to 6. 'Special objects' are formed by combining a copy of the object with the different number of reference points as mentioned in cases 1-3. In case 4, the effect of the location of the reference point with respect to the object is discussed. In addition, in case 5, a 'special object' is formed by combining two copies of the object located with some separation. Moreover, case 6 shows the effect on the autocorrelation when a 'special object' is formed using object-inverted conjugate pair. Object autocorrelations are displaced for different shapes of special objects as follows,

C.1.1 Case 1:

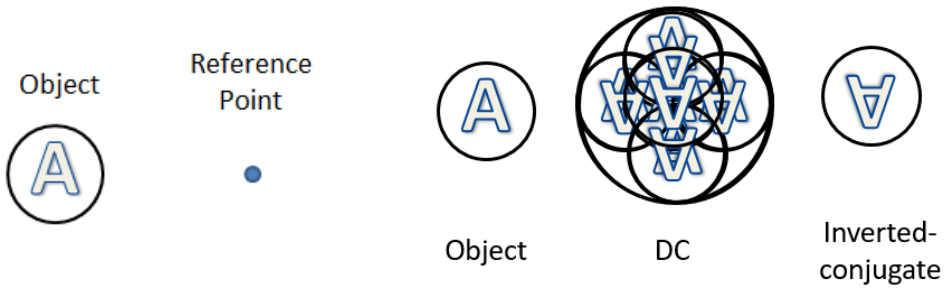

Figure C.1.1: (a) Special object contains an object and a reference point, (b) object autocorrelation for the 'special object' shown in (a).

Figure C.1.1 (a): 'Special object' has an object (left side) and a reference point (right side).

Figure C.1.1 (b): Autocorrelation of this 'special object' has three terms, one copy of the object is located at the left side, DC term is located at the center which contains multiple copies of the object and its inverted-conjugate merged with one

another, these copies spread throughout the autocorrelation region; moreover, one copy of the inverted-conjugate of the object is located at the right side.

C.1.2 Case 2:

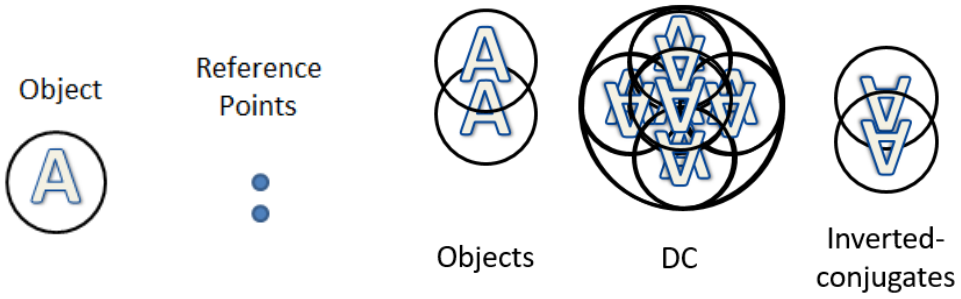

(a) (b)

Figure C.1.2: (a) 'Special object' contains an object and two reference points, (b) respective autocorrelation.

Figure C.1.2 (a): 'Special object' has an object (left side) and two reference points (right side).

Figure C.1.2 (b): Autocorrelation has three terms, two copies of the object are located at the left side, at the center DC term is located, and two copies of the inverted-conjugate are positioned at the right side.

C.1.3 Case 3:

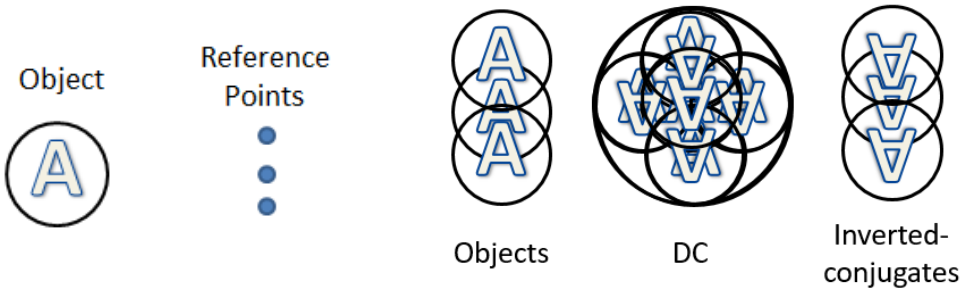

(a) (b)

Figure C.1.3: (a) 'Special object' contains object and three reference points, (b) corresponding object's autocorrelation.

Figure C.1.3 (a): 'Special object' has an object (left side) and three reference points (right side).

Figure C.1.3 (b): Autocorrelation has three terms, the left side has three copies of the object, at the center DC term is present, and right side has three copies of the inverted-conjugate.

From the aforementioned figures C.1.1-C.1.3, it is clear that the number of reference points increases the number of copies of the object and its inverted-conjugate.

C.1.4 Case 4:

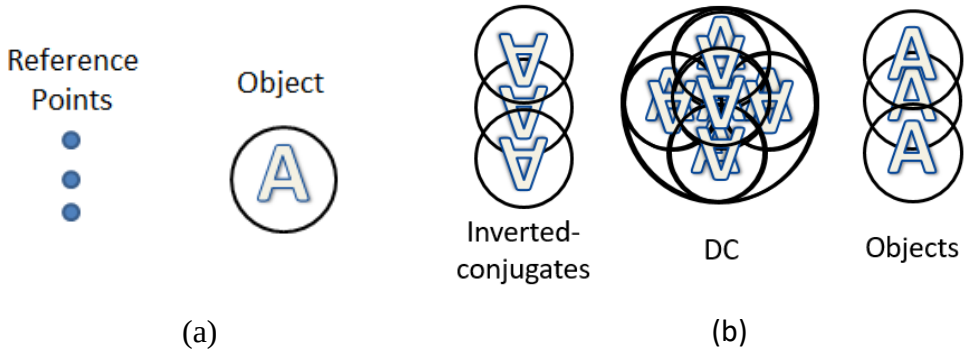

Figure C.1.4: (a) 'Special object' contains object and three reference points, (b) corresponding object autocorrelation of the 'special object'.

Figure C.1.4 (a): 'Special object' has an object (right side) and three reference points (left side).

Figure C.1.4 (b): Respective autocorrelation has three terms, left side has three copies of the inverted-conjugate, DC term is located at the center, and the right side has three copies of the object.

Comparing figures C.1.4 (a) and (b) with figures C1.3 (a) and (b), one can see that by changing the location of the reference points from right to left, the locations of the copies of the object and its inverted-conjugate are also changed accordingly.

C.1.5 Case 5:

(a) (b)

Figure C.1.5: (a) 'Special object' contains two copies of the object, (b) respective autocorrelation

Figure C.1.5 (a): 'Special object' has two copies of the object.

Figure C.1.5 (b): Autocorrelation has three terms, since any object can be considered as a composition of many numbers of points. Situation 1: for the object located at left side in the 'special object', the object copy located at right side in the 'special object' works as a collection of many reference points; therefore, in the autocorrelation, at left side multiple copies of the object appear and on right side multiple copies of the inverted-conjugate of the object appear along with DC term at the center. Situation 2: similarly for the object located at the right, the object located on the left side acts as the collection of the many reference points; therefore, in the autocorrelation, multiple copies of the inverted-conjugate at the left side are generated and many copies of the object at the right side are produced along with the DC term at the center. Hence, at left side, copies of the object generated in situation 1 are merged with the copies of inverted-conjugate generated in situation 2 and formed the DC term. Similarly, at the right side, terms gets merged and formed the DC term. Therefore, for the 'special object' shown in figure C.1.5 (a), the respective autocorrelation of the 'special object' contains three DC terms located at the left, center, and right sides respectively.

C.1.6 Case 6:

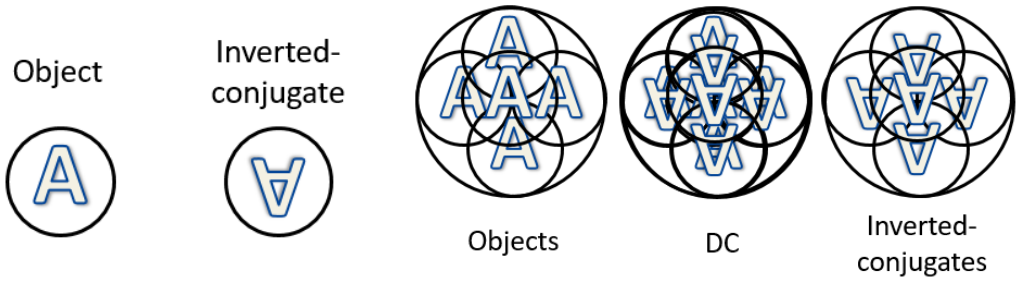

(a) (b)

Figure C.1.6: (a) 'Special object' contains object and inverted-conjugate pair, (b) respective object autocorrelation.

Figure C.1.6 (a): 'Special object' has an object and inverted-conjugate of the object.

Figure C.1.6 (b): Corresponding autocorrelation has three terms, left side has multiple copies of the object, center one has DC term and the right side has multiple copies of the inverted-conjugate of the object.

Circumstance 1: for the object copy located at left side in the ‘special object’, an inverted-conjugate copy of the object located at right side in the ‘special object’ works as the collection of many reference points; therefore, in the autocorrelation, at the left side multiple copies of the object appear and right side multiple copies of the inverted-conjugate appear along with DC term at the center. Circumstance 2: for the inverted-conjugate of the object located right side, the object located on the left side acts as the collection of the many reference points; therefore, in the autocorrelation, multiple copies of the object at the left side are generated and many copies of the inverted-conjugate of the object at the right side are generated along with the DC at the center. Hence, considering these two circumstances, copies of the object are generated only on the left side, and copies of the inverted-conjugate are generated only on the right side. Therefore, for the ‘special object’ shown in figure C.1.6 (a), the corresponding autocorrelation shown in figure C.1.6 (b), contains three terms: object copies at the left side, DC term at the center, and inverted-conjugate copies appear only at the right side.

Appendix D

HIO and HIO+GS algorithms

To start the phase retrieval algorithm, a far-field intensity of the complex object is required. The intensity is captured at the Fourier plane with the help of a CCD camera and is denoted with the notation I as shown in figure D.1. For processing this pattern a programming software i.e., MATLAB is used. An object autocorrelation A_c (two dimensional complex function) is obtained from the intensity by performing a 2D inverse Fourier transform (I.F.T) operation numerically. From the autocorrelation, object support OS information is calculated as mentioned in the Appendix B. Then, to crop a portion from the autocorrelation, shifted object support OS_s or $S(r_o, \theta)$ from the object support is obtained by introducing a shift equal to the radius of the object support along the direction θ. To initiate the algorithm, a two dimensional complex function f is created as an initial guess at the object plane by multiplying the 2D complex autocorrelation with the shifted object support $S(r_o, \theta)$. The field at the Fourier plane F is calculated by operating 2D Fourier transform (F.T.) operation on the function f . Since at the Fourier plane one has already recorded amplitude information which can be obtained from I by calculating its square root, the amplitude of the function F is replaced with the square root of the intensity i.e., $\sqrt{I}$, and a new function F' is created. To obtain a field at the object plane f' , 2D inverse Fourier transform (I.F.T) operation is performed on the F'. At this plane, function is modified as shown in the figure by incorporating $S(r_o, \theta)$ and $S'(r_o, \theta)$, where $S'(r_o, \theta)$ denotes the pixels outside the object support, and value of feedback coefficient β is taken 1, and another function f is obtained. This completes one loop or one iteration of the HIO – PRA. Error E , in each iteration, is calculated as given below.

$$E = \sqrt{\frac{\sum_{r \in S'(r_o,\theta)} |f|^2}{\sum_r |f|^2}} \tag{D.1}$$

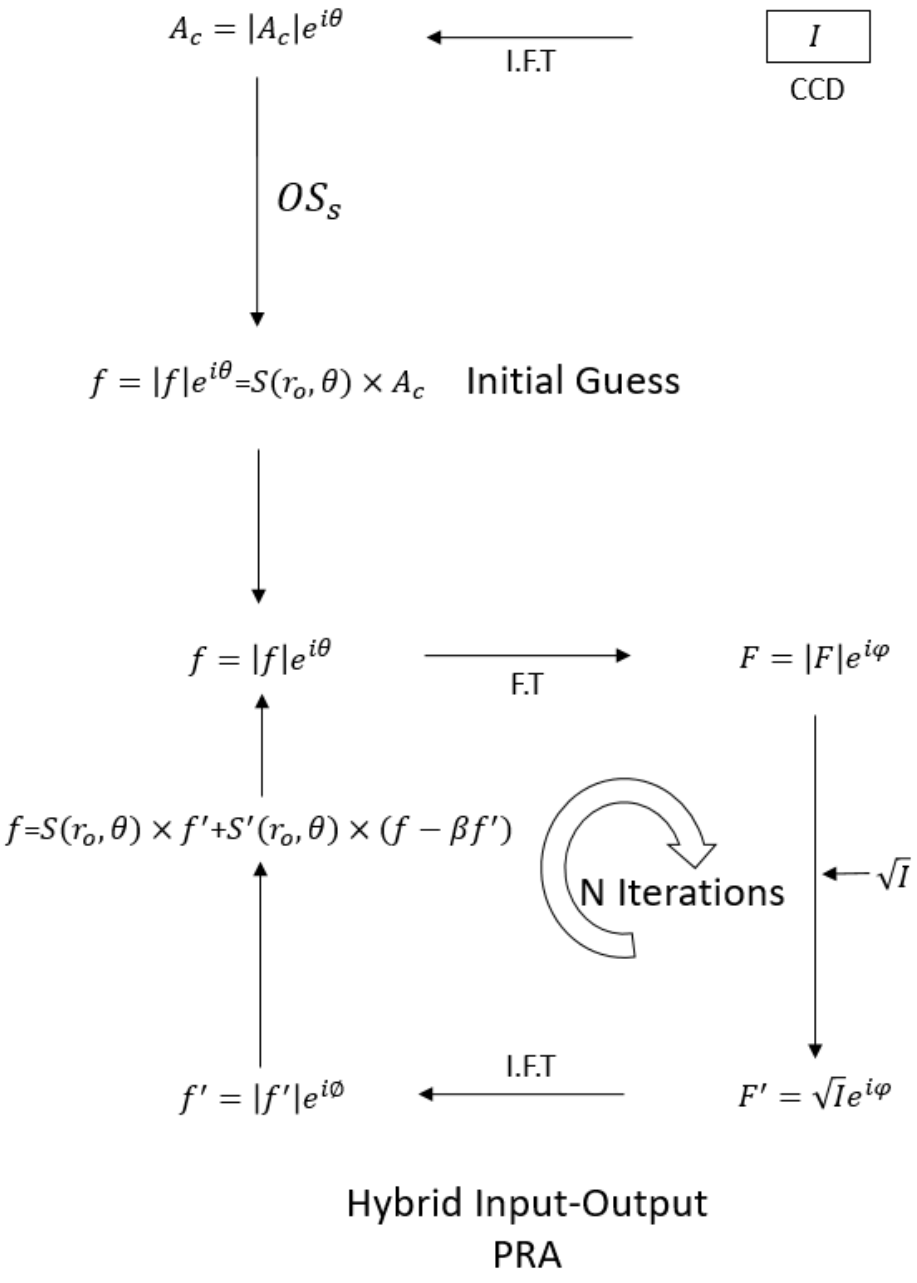

Figure D.1: Flow diagram of hybrid input-output (HIO) phase retrieval algorithm.

For a better convergence rate, researchers have proposed another PRA which combines both HIO as well as GS algorithms. In this combined algorithm few iterations of HIO should be followed by some iterations of GS algorithm. Here we choose 35 iterations of HIO followed by 5 iterations of GS algorithm. 35 HIO + 5 GS completes the one loop or one iteration of

the HIO + GS PRA. The combined HIO + GS algorithm is shown in figure D.2.

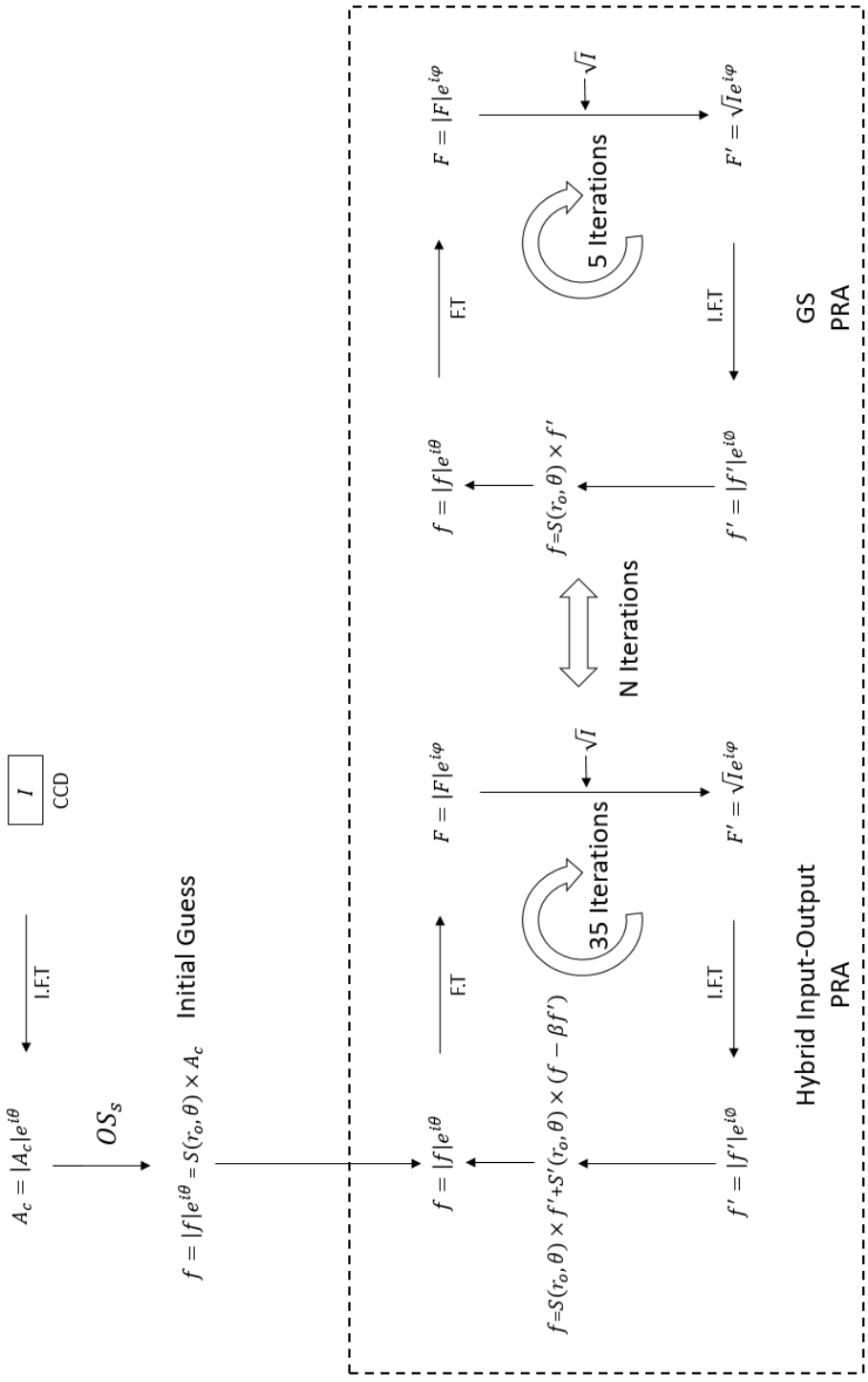

Figure D.2: Flow diagram of hybrid input-output (HIO) followed by the Gerchberg–Saxton (GS) phase retrieval algorithm.

References

1. J. W. Goodman, “Statistical Optics,” Willey-Interscience, New York, 2000, ISBN 0-471-39916-7, pp 576.
2. Graube, A.1975, Applied Physics Letters, 27, 136. doi:10.1063/1.88382.
3. Ulf Schnars and Werner P O Jüptner 2002 Meas. Sci. Technol. 13 R85.
4. J. W. Goodman, “Introduction to Fourier Optics,” 3rd Edition, Roberts & Company Publishers, Englewood, 2004.
5. Mitsuo Takeda, Hideki Ina, and Seiji Kobayashi, "Fourier-transform method of fringe-pattern analysis for computer-based topography and interferometry," J. Opt. Soc. Am. 72, 156-160 (1982).
6. Computational Fourier optics; a MATLAB tutorial. (2011, April 1). The Free Library. Retrieved November 12, 2021 from https://www.thefreelibrary.com/Computational Fourier optics; a MATLAB tutorial.-a0253495199.
7. Goodman, Joseph & Lawrence, R. , ”Digital image formation from electronically detected holograms,” Applied Physics Letters 11, 77 - 79. 10.1063/1.1755043 (1967).
8. J. R. Fienup, "Reconstruction of a complex-valued object from the modulus of its Fourier transform using a support constraint," J. Opt. Soc. Am. A 4, 118-123 (1987).
9. Emmett N. Leith and Juris Upatnieks, "Reconstructed Wavefronts and Communication Theory*," J. Opt. Soc. Am. 52, 1123-1130 (1962).
10. Ichirou Yamaguchi and Tong Zhang, "Phase-shifting digital holography," Opt. Lett. 22, 1268-1270 (1997).
11. J. R. Fienup and C. C. Wackerman, "Phase-retrieval stagnation problems and solutions," J. Opt. Soc. Am. A 3, 1897-1907 (1986).

12. T. R. Crimmins, J. R. Fienup, and B. J. Thelen, "Improved bounds on object support from autocorrelation support and application to phase retrieval," J. Opt. Soc. Am. A 7, 3-13 (1990).
13. J. R. Fienup, "Reconstruction of an object from the modulus of its Fourier transform," Opt. Lett. 3, 27-29 (1978).
14. J. R. Fienup, "Phase retrieval using boundary conditions," J. Opt. Soc. Am. A 3, 284-288 (1986).
15. Tatiana Latychevskaia, Hans-Werner Fink, “Solution to the Twin Image Problem in Holography,” Phys. Rev. Lett. 98, 233901 (2007).
16. Manuel Guizar-Sicairos and James R. Fienup, "Understanding the twin-image problem in phase retrieval," J. Opt. Soc. Am. A 29, 2367-2375 (2012).
17. Charu Gaur, Baranidharan Mohan, and Kedar Khare, "Sparsity-assisted solution to the twin image problem in phase retrieval," J. Opt. Soc. Am. A 32, 1922-1927 (2015).
18. Junbao Hu and Lingfeng Wu , "Transport of intensity phase microscopy combined with accelerated iteration for quantitative phase imaging," J. Opt. 21, 085703 (2019).
19. László Orzó, "High speed phase retrieval of in-line holograms by the assistance of corresponding off-axis holograms," Opt. Express 23, 16638-16649 (2015).
20. Surya Kumar Gautam, R. Kumar Singh, C. S. Narayanamurthy, and D. N. Naik, "Reconstruction of complex-object using edge point referencing," J. Opt. 22, 055601 (2020).
21. J. R. Fienup, "Phase retrieval algorithms: a comparison," Appl. Opt. 21, 2758-2769 (1982).
22. Surya Kumar Gautam, Rakesh Kumar Singh, C. S. Narayanamurthy, and Dinesh N. Naik, "Single-shot and twin-image free unique phase retrieval using an aspect of autocorrelation that considers the object asymmetry," J. Opt. Soc. Am. A 37, 1826-1831 (2020).
23. Shao, X., He, X. Real-time 3D Digital Image Correlation for Large Deformation and Rotation Measurements Based on a Deformation

Transfer Scheme. Exp Mech 61, 951–967 (2021). https://doi.org/10.1007/s11340-021-00714-9.

24. Teruyoshi Nobukawa and Takanori Nomura, "Multilevel recording of complex amplitude data pages in a holographic data storage system using digital holography," Opt. Express 24, 21001-21011 (2016).
25. K. Curtis, L. Dhar, A. Hill, W. Wilson, and M. Ayres, Holographic Data Storage: From Theory to Practical Systems (Wiley, 2010).
26. M. Gu, X. Li, and Y. Cao, “Optical storage arrays: a perspective for future big data storage,” Light: Sci. Appl. 3, e177 (2014).
27. Burr, G. W., Barking, G., Coufal, H., Hoffnagle, J. A., Jefferson, C. M., and Neifeld, M. A., “Gray-scale data pages for digital holographic data storage,” Opt. Lett. 23(15), 1218-1220 (1998).
28. Kim SB, Bae H, Koo KI, Dokmeci MR, Ozcan A, Khademhosseini A. Lens-free imaging for biological applications. J Lab Autom. 2012 Feb;17(1):43-9. doi: 10.1177/2211068211426695. PMID: 22357607; PMCID: PMC3685198.
29. Gerchberg, R. W.. “A practical algorithm for the determination of phase from image and diffraction plane pictures.” Optik 35 (1972): 237-246.
30. Bai, H., Min, R. & Yang, Z. Phase retrieval for off-axis digital holography using multiplexing with hologram rotation and complex encoding. Opt Rev 26, 549–560 (2019). https://doi.org/10.1007/s10043-019-00525-3.
31. J.R. Fienup and A.M. Kowalczyk, "Phase Retrieval for a Complex-Valued Object by Using a Low-Resolution Image," J. Opt. Soc. Am. A 7, 450–458 (1990).
32. J.R. Fienup, “Direct-detection Synthetic-aperture Coherent Imaging by Phase Retrieval,” Opt. Eng. 56, (2017), 113111.
33. GABOR D 1948 A New Microscopic Principle Nature.
34. Schnars U and Jüptner W 1994 Direct recording of holograms by a CCD target and numerical reconstruction 33 179–81.

35. Guo P and Devaney A J 2004 Digital microscopy using phase-shifting digital holography with two reference waves 29 857–9.
36. Wang Y, Zhen Y, Zhang H and Zhang Y 2004 Study on digital holography with single phase-shifting operation Chi. Opt. Lett.
37. Gabor D and Goss W P 1966 Of AMERICA 56.
38. Meng X F, Cai L Z, Xu X F, Yang X L, Shen X X, Dong G Y and Wang Y R 2006 Two-step phase-shifting interferometry and its application in image encryption 31 1414–6.
39. Liu J and Poon T 2009 Two-step-only quadrature phase-shifting 34 250–2.
40. Takaki Y, Kawai H and Ohzu H 1999 Hybrid holographic microscopy free of conjugate and zero-order images.
41. Demoli N, Mes J and Sovic I 2003 Subtraction digital holography.
42. ang Y, Cheng Z-J, Zhao H-M, Yue Q-Y and Guo C-S 2018 Quantitative phase imaging system with slightly-off-axis configuration and suitable for objects both larger and smaller than the size of the image sensor Opt. Express 26 17199–208.
43. Johanan L. Codona, Nathan Doble, Experimental evaluation of differential OTF (dOTF) wavefront sensing, Proc. SPIE 8447, Adaptive Optics Systems III, 84476R (13 September 2012); https://doi.org/10.1117/12.927025.
44. Pavillon N, Seelamantula C S, Kühn J, Unser M and Depeursinge C 2009 Suppression of the zero-order term in off-axis digital holography through nonlinear filtering Appl. Opt. 48.
45. Charrière F, Colomb T, Montfort F, Cuche E, Marquet P and Depeursinge C 2006 Shot-noise influence on the reconstructed phase image signal-to-noise ratio in digital holographic microscopy Appl. Opt. 45 7667–73.
46. Zhao J, Wang D Y, Wang H Y and Xie J J 2007 High-resolution lensless Fourier transform holography for microstructure imaging - art. no. 67230N 3rd Int. Symp. Adv. Opt. Manuf. Test. Technol. Opt. Test Meas. Technol. Equipment, Parts 1-3 6723 N7230–N7230.

47. Doval Á F, Trillo C, Vigo U De, Física D De, Ingenieros A E T S De and Vigo C U Dimensionless formulation of the convolution and angular spectrum reconstruction methods in digital holography 7387 1–10.
48. D. J. Chen, F. P. Chiang, Y. S. Tan, and H. S. Don, "Digital speckle-displacement measurement using a complex spectrum method," Appl. Opt. 32, 1839-1849 (1993).
49. J. Hartmann, “Bemerkungen uber den Bau und die Justirung von Spektrographen,” Zt. Instrumentenkd. 20, 47 (1900).
50. B. C. Platt and R. Shack, "History and Principles of Shack-Hartmann Wavefront Sensing," Journal of Refractive Surgery 17, 573-577 (2001).
51. Peters, W. and W. Ranson. “Digital Imaging Techniques In Experimental Stress Analysis.” Optical Engineering 21 (1982): 427-431.
52. Pan B. Reliability-guided digital image correlation for image deformation measurement. Appl Opt. 2009 Mar 10;48(8):1535-42. doi: 10.1364/ao.48.001535. PMID: 19277087.
53. D. R. Neal, J. Copland, D. A. Neal, “Shack-Hartmann wavefront sensor precision and accuracy,” Proc. SPIE 4779, Advanced Characterization Techniques for Optical, Semiconductor, and Data Storage Components, (11 November 2002).
54. Valentina Ye. Zavalova, Alexis V. Kudryashov, "Shack-Hartmann wavefront sensor for laser beam analyses," Proc. SPIE 4493, High-Resolution Wavefront Control: Methods, Devices, and Applications III, (1 February 2002); https://doi.org/10.1117/12.454723.
55. Panagopoulou, S.. “- 1-Zernike vs . Zonal Matrix Iterative Wavefront Reconstructor.” (2005).
56. Fengzhao Dai, Feng Tang, Xiangzhao Wang, Osami Sasaki, and Peng Feng, "Modal wavefront reconstruction based on Zernike polynomials for lateral shearing interferometry: comparisons of existing algorithms," Appl. Opt. 51, 5028-5037 (2012).

57. Apaolaza, Iñigo. “Characterization of optical aberrations: practical implementation of a Shack-Hartmann sensor with Matlab.” (UPNA) Viena, 30 de junio de (2019).
58. Daniel M. Topa, "Wavefront reconstruction for the Shack-Hartmann wavefront sensor," Proc. SPIE 4769, Optical Design and Analysis Software II, (4 September 2002), pp 101-115; https://doi.org/10.1117/12.481179.
59. Kudryashov, V. Samarkin, A. Alexandrov, J. Sheldakova and V. Zavalova, "Shack-Hartmann wavefront sensor - advantages and disadvantages," International Conference on Advanced Optoelectronics and Lasers, Sevastopol, 2010, pp. 76-77.
60. Pan, Bing & Qian, Kemao & Xie, Huimin & Asundi, Anand. (2009). TOPICAL REVIEW: Two-dimensional digital image correlation for in-plane displacement and strain measurement: a review. Measurement Science & Technology. 20. 10.1088/0957-0233/20/6/062001.
61. Touchard, Fabienne & Brillaud, Jean & Lafarie-Frenot, M.C.. (2004). High strain gradient measurements by using digital image correlation technique. Materials Characterization. 53. 17-28. 10.1016/j.matchar.2004.07.009.
62. Pan, Bing. (2018). Digital image correlation for surface deformation measurement: Historical developments, recent advances and future goals. Measurement Science and Technology. 29. 082001. 10.1088/1361-6501/aac55b.
63. Xinxing Shao, Xiangjun Dai, Zhenning Chen, and Xiaoyuan He, "Real-time 3D digital image correlation method and its application in human pulse monitoring," Appl. Opt. 55, 696-704 (2016).
64. Pan, B., Yu, L. & Zhang, Q. Review of single-camera stereo-digital image correlation techniques for full-field 3D shape and deformation measurement. Sci. China Technol. Sci. 61, 2–20 (2018). https://doi.org/10.1007/s11431-017-9090-x.

65. Bing Pan and Qiong Wang, "Single-camera microscopic stereo digital image correlation using a diffraction grating," Opt. Express 21, 25056-25068 (2013).
66. Thomas Fricke-Begemann, "Three-dimensional deformation field measurement with digital speckle correlation," Appl. Opt. 42, 6783-6796 (2003).
67. Gregory, D. A. “Basic Physical Principles of Defocused Speckle Photography: A Tilt Topology Inspection Technique.” Optics and Laser Technology 8.5 (1976): 201–213.
68. P. F. Luo, Y. J. Chao, M. A. Sutton, and W. H. Peters III, “Accurate measurement of three-dimensional displacement in deformable bodies using computer vision,” Exp. Mech. 33(2), 123–132 (1993).
69. B. Pan, D. F. Wu, and L. P. Yu, “Optimization of a three-dimensional digital image correlation system for deformation measurements in extreme environments,” Appl. Opt. 51(19), 4409–4419 (2012).
70. Reinhard Feiel and Philip Wilksch, "High-resolution laser speckle correlation for displacement and strain measurement," Appl. Opt. 39, 54-60 (2000).
71. Zhenxing Hu, Huimin Xie, Jian Lu, Tao Hua, and Jianguo Zhu, "Study of the performance of different subpixel image correlation methods in 3D digital image correlation," Appl. Opt. 49, 4044-4051 (2010).
72. Khoo, Sze Wei & Karuppanan, Saravanan & Tan, Cs. (2016). A Review of Surface Deformation and Strain Measurement Using Two-Dimensional Digital Image Correlation. Metrology and Measurement Systems. 23. 10.1515/mms-2016-0028.
73. Bing Pan, Huimin Xie, and Zhaoyang Wang, "Equivalence of digital image correlation criteria for pattern matching," Appl. Opt. 49, 5501-5509 (2010).

74. Yu, Liping & Tao, Ran & Lubineau, Gilles. (2019). Accurate 3D Shape, Displacement and Deformation Measurement Using a Smartphone. Sensors. 19. 719. 10.3390/s19030719.
75. Pan, Bing & Xie, Huimin & Gao, Jianxin & Asundi, Anand. (2008). Improved speckle projection profilometry for out-of-plane shape measurement. Applied optics. 47. 5527-33. 10.1364/AO.47.005527.
76. Gombkötő, Balázs and J. Kornis. “Success rate and speckle correlation in electronic speckle photography.” Optics Communications 201 (2002): 289-292.
77. Mudassar, Asloob & Butt, Saira. (2015). Improved Digital Image Correlation method. Optics and Lasers in Engineering 87, 156-167; 10.1016/j.optlaseng.2015.10.002i.
78. M. Sjödahl, "Electronic speckle photography: measurement of in-plane strain fields through the use of defocused laser speckle," Appl. Opt. 34, 5799-5808 (1995).

List of Publication

Published

1. Gautam, S. K., Kumar Singh, R., Narayanamurthy, C. S., and Naik, D. N., “Reconstruction of complex-object using edge point referencing”, Journal of Optics, vol. 22, no. 5, 2020. doi:10.1088/2040-8986/ab7e8b.
2. Kumar Gautam S, Singh RK, Narayanamurthy CS, Naik DN. Single-shot and twin-image free unique phase retrieval using an aspect of autocorrelation that considers the object asymmetry. J Opt Soc Am A Opt Image Sci Vis. 2020 Nov 1;37 (11):1826-1831. doi: 10.1364/JOSAA.402731. PMID: 33175759.
3. Vipin Tiwari, Surya Kumar Gautam, Dinesh N. Naik, Rakesh Kumar Singh, and Nandan S. Bisht, "Characterization of a spatial light modulator using polarization-sensitive digital holography," Appl. Opt. 59, 2024-2030 (2020).
4. Mishra, Shalabh & Gautam, Surya & Naik, Dinesh & Chen, Ziyang & Ji-Xiong, Pu & Singh, Rakesh kumar. (2018). Tailoring and analysis of vectorial coherence. Journal of Optics. 20. 10.1088/2040-8986/aaef2a.

Under production

1. Surya Kumar Gautam, Pramod Panchal, Athira T S, Dinesh N Naik, “Phase retrieval algorithm using edge point referencing”, Optics Letter (2022).

Under processing

1. Discreate and quantitative reconstruction of the out of plane non-linear deformation using local autocorrelations.
2. Recording and reconstruction using phase retrieval algorithm in volumetric holographic data storage.
3. Photography assisted phase retrieval algorithms.
4. Single-shot Jones Matrix microsopy

Conferences procedings

1. **S. K. Gautam**, D. N. Naik, R. K. Singh, and C. S. Narayanamurthy, "Amplitude Shifting Holography," in *Frontiers in Optics / Laser Science*, OSA Technical Digest (Optical Society of America, 2018), paper JW3A.8. https://www.osapublishing.org/abstract.cfm?URI=LS-2018-JW3A.8.
2. **S. K. Gautam**, R. Chakkappai, D. N. Naik, R. K. Singh, and C. S. Narayanamurthy, "Optimization of Space-time Bandwidth for Shearography," in *Frontiers in Optics + Laser Science APS/DLS*, The Optical Society (Optical Society of America, 2019), paper JTu4A.7.

https://www.osapublishing.org/abstract.cfm?URI=LS-2019-JTu4A.7.

3. Arnav Tamrakar, **Surya Kumar Gautam**, Dinesh N. Naik, "Extraction of information of an object hidden behind a diffusing layer using dual beam illumination," Proc. SPIE 11351, Unconventional Optical Imaging II, 113511R (30 March 2020); https://doi.org/10.1117/12.2555748.
4. Urvashi Jinwal, **Surya Kumar Gautam**, Athira T. S., Pramod Panchal, Dinesh N. Naik, "Velocity estimation from fringe contrast using lensless Fourier transform digital holography," Proc. SPIE 11352, Optics and Photonics for Advanced Dimensional Metrology, 113521L (1 April 2020); https://doi.org/10.1117/12.2555789.
5. **Gautam S.K.**, Panchal P., Mishra P., Naik D.N., Narayanamurthy C.S., Singh R.K. (2021) Single-Shot Jones Matrix Microscopy. In: Singh K., Gupta A.K., Khare S., Dixit N., Pant K. (eds) ICOL-2019. Springer Proceedings in Physics, vol 258. Springer, Singapore. https://doi.org/10.1007/978-981-15-9259-1_128.
6. Athira T.S., Panchal P., **Gautam S.K.**, Naik D.N. (2021) Revealing Relative Phase Shift of Individual Beams Through the Phase of the Superposed Beam. In: Singh K., Gupta A.K., Khare S., Dixit N., Pant K. (eds) ICOL-2019. Springer Proceedings in Physics, vol 258. Springer, Singapore. https://doi.org/10.1007/978-981-15-9259-1_131.
7. V A., **Gautam S.K.**, Panchal P., Athira T.S., Gopinath P., Naik D.N. (2021) Influence of Lateral Resolution in Measurement of Surface Profile. In: Singh K., Gupta A.K., Khare S., Dixit N., Pant K. (eds) ICOL-2019. Springer Proceedings in Physics, vol 258. Springer, Singapore. https://doi.org/10.1007/978-981-15-9259-1_122.
8. Miyamoto, Yoko & CHANDRAN THODIKA, Samlan & **Gautam, Surya** & Naik, Dinesh & Viswanathan, Nirmal. (2020). Correction to spatial mode transformation in a modified interferometer. 30. 10.1117/12.2573768.

9. **S. K. Gautam**, and D. N. Naik, Initial Standard Guess for Phase Retrieval Algorithms, Photonics 2018 (The International Conference on Fiber Optics & Photonics), IIT Delhi, 12-15 2018.
10. **S. K. Gautam**, and D. N. Naik, Analysis of Photorefractive BTO Crystal using Jones Matrix, Photonics 2018 (The International Conference on Fiber Optics & Photonics), IIT Delhi, 12-15 2018.
11. **S. K. Gautam**, and D. N. Naik, " Utilizing object asymmetry in the phase retrieval algorithm," in *Frontiers in Optics / Laser Science*, (OPTICA, 2021), paper JTu1A.6.
12. **S. K. Gautam**, and D. N. Naik, " Random verses improved initial guess on the reconstruction from phase retrieval algorithm," in *Frontiers in Optics / Laser Science*, (OPTICA, 2021), paper JTu1A.8.